AD-A251 149

Computations of Nonlinear Gravity Waves by a Desingularized Boundary Integral Method

Yusong Cao
Department of Naval Architecture and Marine Engineering

Contract Number N00014-86-K-0684
Technical Report No. 91-3

October 1991

DTIC
ELECTE
JUN 1 1992
S D
C

Approved for public release
Distribution Unlimited

92-13790

92 5 28 016

Statement A per telecon Dr. Edwin Rood
ONR/Code 1132
Arlington, VA 22217-5000

NWW 6/1/92

Dist | Special
A-1

ABSTRACT

COMPUTATIONS OF NONLINEAR GRAVITY WAVES BY A DESINGULARIZED BOUNDARY INTEGRAL METHOD

by

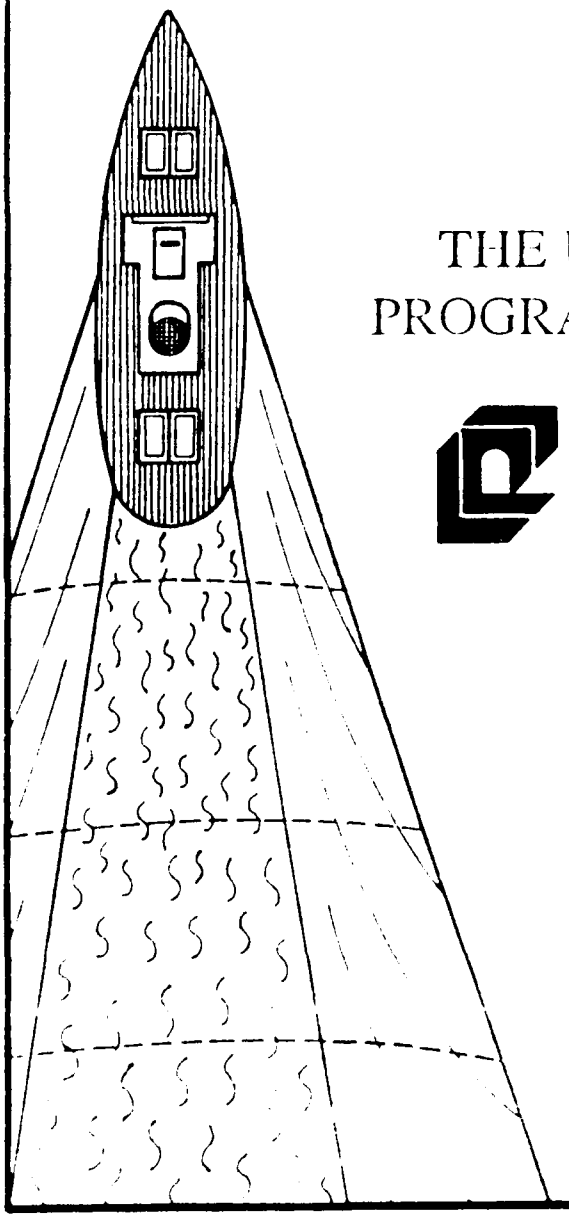
Yusong Cao

Chairpersons: Robert F. Beck, William W. Schultz

A desingularized boundary integral equation method combined with an Eulerian-Lagrangian time-stepping technique is developed for nonlinear gravity wave problems. The desingularization distance between the boundary and the sources is related to the local mesh size to ensure convergence. Tests for some simple problems show that desingularization significantly reduces the computer time required to compute the influence matrix of the resulting algebraic system. The algebraic system is still adequately well-conditioned to allow fast iterative solutions. Accurate solutions can be obtained for a large range of desingularization distances on the order of the mesh size.

Several nonlinear water wave problems are then investigated. The first problem considers upstream runaway solitons due to a disturbance moving near critical speed in two-dimensional shallow water. Results from the desingularized method

with the fully nonlinear free surface boundary condition agree well to those using the fKdV model for weak disturbances. The fully nonlinear model predicts larger solitons than the fKdV model for strong disturbances and also predicts the breaking of waves for some stronger disturbances. Next, the problem of three-dimensional waves due to a submerged moving spheroid show good comparison to those from other algorithms. Finally, the generation of inner-angle wavepackets in the wake of a ship is investigated. The three most probable causes of the wavepackets are examined: interference of the wave systems by the bow and stern; free-surface nonlinear effects; and wake unsteadiness due to translation and oscillation of the disturbance. The wake is studied with nonlinear calculations using the desingularized method and with linear calculations using a time-domain Green function and the stationary phase method. It is shown that nonlinear effects are not essential to the generation and persistence of inner-angle wavepackets; the phenomenon can be explained by unsteady linear theory.



THE UNIVERSITY OF MICHIGAN
PROGRAM IN SHIP HYDRODYNAMICS

COLLEGE OF ENGINEERING

NAVAL ARCHITECTURE &
MARINE ENGINEERING

AEROSPACE ENGINEERING

MECHANICAL ENGINEERING &
APPLIED MECHANICS

SHIP HYDRODYNAMIC
LABORATORY

SPACE PHYSICS RESEARCH
LABORATORY

ERIM

© Yusong Cao 1991
All Rights Reserved

To my parents, wife and daughter

ACKNOWLEDGEMENTS

I would like to thank my advisors Professor Beck and Professor Schultz for all of their efforts during the course of this work with the kind guidance and encouragement. This work would never have been possible without their dedication, their enthusiasm, their experience and their expertise. I am also grateful to Professor Troesch and Professor Vorus for their comments, discussions and suggestions and for their accepting to serve in my dissertation committee. Thanks are also due to Professor Klaus-Peter Beier and Ms. Carolyn Churchill for helping me in preparing the contour and isometric plots of waves in the thesis with the M-plot graphic package and the animation of the computed waves presented at the thesis defense.

I owe my gratitude to my late grand-uncle Tsao Yeu Sheung and my grand-aunt Mrs. Ellen Li, C.B.E., J.P., LL.D for their enthusiastic support of my education in the University of Michigan. Their financial support for the first year made it possible for me to start at Michigan. Their effort, including financial support, also made it possible for my wife and daughter to come and join me later.

I would like to thank Dr. Allan Magee for not only helpful discussions but also providing me the subroutine for the time-domain Green function which is used in this work to calculate the unsteady linear waves. I also appreciate faculty, staff members and colleagues of the Department of Naval Architecture and Marine Engineering, especially Mrs. Virginia Konz, Mrs. Lisa Payton, Dr. Ivan Kirschner, Dr. Allan

Magee and Dr. Jeffrey Falzarano, for their help and friendship which have made my stay in Ann Arbor a very pleasant memory.

This work is supported under the Program in Ship Hydrodynamics at The University of Michigan, funded by The University Research Initiative of the Office of Naval Research, Contract Number N000184-86-K-0684. Computations were made in part using a CRAY Grant at the University Research and Development Program of the San Diego Supercomputer Center. Financial assistance from Rackham Travel Grant to my three trips to attend and present the research work at the International Workshop on Water Waves and Floating Bodies is also appreciated.

TABLE OF CONTENTS

DEDICATION ii

ACKNOWLEDGEMENTS iii

LIST OF FIGURES vii

LIST OF APPENDICES xiii

CHAPTER

I. INTRODUCTION 1

II. PROBLEM FORMULATION AND SOLUTION PROCEDURE 6

2.1 Initial-Boundary Value Problem 6
2.1.1 Governing equation 6
2.1.2 Boundary and initial conditions 7
2.2 Solution Procedure for Nonlinear Waves 10
2.2.1 Solution procedure 10
2.2.2 Numerical implementation 13

III. DESINGULARIZED BOUNDARY INTEGRAL METHOD 15

3.1 Desingularized Integral Equations 18
3.1.1 Direct method 19
3.1.2 Indirect method 20
3.2 Uniqueness of Desingularized Integral Equation and Convergence of the Numerical Methods 21
3.3 Simple Test Examples 23
3.3.1 A dipole below a $\phi = 0$ infinitive flat plane 25
3.3.2 Waves due to a source-sink pair moving below the free surface 35
3.4 Conclusions 38

IV. TWO-DIMENSIONAL SOLITONS IN A SHALLOW WATER 43

4.1 fKdV Equation 45
4.2 Fully Nonlinear Model 47
4.3 Numerical Results 49
4.3.1 Solitons due to a free surface pressure 50
4.3.2 Comparison of free surface pressure and bottom topography 51
4.3.3 Solitons due to submerged cylinders 52
4.4 Conclusions 53

V. WAVES GENERATED BY A SUBMERGED SPHEROID . 65

5.1 Numerical Aspects 67
5.2 Results 70
5.3 Conclusions 74

VI. UNSTEADY WAKE AND INNER-ANGLE WAVEPACKETS 85

6.1 Nonlinear Wave Calculations 89
6.1.1 Multigrid and matrix preconditioning 90
6.1.2 Computational results 91
6.2 Linear Wave Calculations 93
6.2.1 Time-domain Green function 94
6.2.2 Computational results 95
6.3 Wave Patterns by Method of Stationary Phase 96
6.3.1 Constant phase lines 97
6.3.2 Bounding angles for constant phase lines 101
6.3.3 Decay rates of waves 102
6.4 Comparisons and Discussions 104
6.5 Conclusions 107

VII. CONCLUSIONS AND SUGGESTIONS FOR FURTHER RESEARCH 146

7.1 Conclusions 146
7.2 Suggestions for Further Research 148

APPENDICES 151

BIBLIOGRAPHY 162

LIST OF FIGURES

Figure

2.1 Problem definition and coordinate system 7

3.1 Convergence of numerical integration 24

3.2 Schematic diagram of a dipole below a $\phi = 0$ infinitive flat plane . . 27

3.3 Effect of desingularization 29

3.4 Comparisons between Gaussian quadrature and analytic integration ($R_\infty = 6.6667$, $N = 231$) 29

3.5 Effect of desingularization on condition number ($R_\infty = 6.6667$, $N = 231$) 30

3.6 Effect of desingularization on computation time ($R_\infty = 6.6667$, $N = 231$) 31

3.7 Effect of iteration tolerance on RMS error ($R_\infty = 6.6667$, $N = 231$, $l_d = 1$, indirect method) 32

3.8 Effect of iteration tolerance on computation time ($R_\infty = 6.6667$, $N = 231$, $l_d = 1$, indirect method) 32

3.9 Convergence with respect to truncation of boundary ($\triangle X = 0.6667$, $l_d = 1$) 33

3.10 Convergence with respect to node number ($R_\infty = 6.667$, $l_d = 1$) . . 33

3.11 Comparison of surface distribution and isolated sources for indirect method ($R_\infty = 6.667$, $N = 231$) 35

3.12 Error distribution along x-axis ($R_\infty = 6.6667$, $N = 231$, $l_d = 1$) . . . 36

3.13 Waves along x-axis ($t = 10$, $\sigma_o = 0.05$, $F_n = 1$) 40

3.14 Waves along x-axis ($t = 10$, $\sigma_o = 0.75$, $F_n = 1$) 41

3.15 Effect of computational domain size on wave elevation along x-axis ($\sigma_o = 0.05$, $F_n = 1$) 42

4.1 Problem definition for solitons in shallow water 45

4.2 Waves due to free surface pressure ($P_m = 0.02$, $F_n = 1.0$, $\Delta t = 0.2$) 54

4.3 Waves due to free surface pressure ($P_m = 0.1$, $F_n = 1.0$, $\Delta t = 0.2$) . 55

4.4 Waves due to free surface pressure ($P_m = 0.15$, $F_n = 1.0$, $\Delta t = 0.2$) 56

4.5 Waves due to free surface pressure ($P_m = 0.1$, $F_n = 1.5$, $\Delta t = 0.2$) . 57

4.6 Waves due to bottom topography ($L = 2.0$, $2P_m = 0.2$, $F_n = 1.0$, $\Delta t = 0.2$) 58

4.7 Waves due to free surface pressure ($L = 2.0$, $2P_m = 0.2$, $F_n = 1.0$, $\Delta t = 0.2$) 59

4.8 Waves due to submerged circular cylinder ($R = 0.15$, $h_c = 0.6$, $F_n = 1.0$, $\Delta t = 0.2$) 60

4.9 Waves due to submerged circular cylinder ($R = 0.2$, $h_c = 0.6$, $F_n = 1.0$, $\Delta t = 0.2$) 61

4.10 Waves due to submerged circular cylinder ($R = 0.15$, $h_c = 0.6$, $F_n = 1.5$, $\Delta t = 0.2$) 62

4.11 Waves due to submerged elliptical cylinder ($R_x = 1.0$, $R_y = 0.075$, $h_c = 0.6$, $F_n = 1.0$, $\Delta t = 0.2$) 63

4.12 Waves due to submerged elliptical cylinder ($R_x = 1.0$, $R_y = 0.1$, $h_c = 0.6$, $F_n = 1.0$, $\Delta t = 0.2$) 64

5.1 The coordinate and the discretization of the spheroid 67

5.2 Waves generated by the spheroid, above: isometric view, below: wave elevation contours (0.02 apart) 76

5.3 Hydrodynamic coefficients vs. time 77

5.4 Influence of start-up of the spheroid 78

5.5 Pressure on the spheroid surface 79

5.6 Sensitivity of the spheroid surface mesh size 80

5.7 Comparison of hydrodynamic coefficients (modified from Doctors & Beck with the present results added) 81

5.8 Waves generated by the relevant source-sink pair, above: isometric view, below: wave elevation contours (0.02 apart) 82

5.9 Effect of desingularization factor l_d 83

5.10 Wave energy and work done by the spheroid 84

6.1 Nonlinear waves due to a translating, non-oscillating source-sink pair 109

6.2 Nonlinear waves due to two translating, non-oscillating dipoles . . . 110

6.3 Nonlinear waves due to two translating, non-oscillating surface pressure patches (weak disturbance) 111

6.4 Nonlinear waves due to two translating, non-oscillating surface pressure patches (strong disturbance) 111

6.5 Comparison of Nonlinear waves to "linear" waves due to two translating, non-oscillating surface pressure patches (strong disturbance) 112

6.6 Nonlinear waves due to a translating and oscillating surface pressure patch with zero mean,$\tau = 0.25$, $F_n = 0.4$ 113

6.7 Nonlinear waves due to a translating and oscillating surface pressure patch with zero mean, $\tau = 0.5$, $F_n = 0.4$ 113

6.8 Nonlinear waves due to a translating and oscillating surface pressure patch with zero mean, $\tau = 1.0$, $F_n = 0.4$ 114

6.9 Nonlinear waves due to a translating and oscillating surface pressure patch with zero mean, $\tau = 2.0$, $F_n = 0.4$ 114

6.10 Nonlinear waves due to a translating and oscillating surface pressure patch with zero mean, $\tau = 4.0$, $F_n = 0.4$ 115

6.11 Nonlinear waves due to a translating and oscillating surface pressure patch with zero mean, $\tau = 6.0$, $F_n = 0.4$ 115

6.12 Nonlinear waves due to a translating and oscillating surface pressure patch with zero mean, $\tau = 1.0$, $F_n = 0.2$ 116

6.13 Linear waves due to a translating and oscillating source-sink pair with zero-mean strength, $\tau = 0.125$ 117

6.14 Linear waves due to a translating and oscillating source-sink pair with zero-mean strength, $\tau = 0.25$ 118

6.15 Linear waves due to a translating and oscillating source-sink pair with zero-mean strength, $\tau = 0.5$ 119

6.16 Linear waves due to a translating and oscillating source-sink pair with zero-mean strength, $\tau = 1.0$ 120

6.17 Linear waves due to a translating and oscillating source-sink pair with zero-mean strength, $\tau = 2.0$ 121

6.18 Bounding line angles *vs* τ (by linear wave calculations using time-domain Green function 122

6.19 Far-field linear waves due to a translating and oscillating source-sink pair with non-zero-mean strength, $\tau = 1.0$ 123

6.20 Linear waves due to a translating and oscillating source-sink pair with zero-mean strength. ($F_n = 2$ and $\tau = 1.0$) 124

6.21 Linear waves due to a translating and oscillating source-sink pair with zero-mean strength. ($F_n = 2$ and $\tau = 2.0$) 124

6.22 Constant phase lines of Kelvin wake, $\tau = 0$ 125

6.23 Constant phase lines, $\tau = 0.2$ 125

6.24 Constant phase lines, $\tau = 0.25_-$ 126

6.25 Constant phase lines, $\tau = 0.25_+$ 126

6.26 Constant phase lines, $\tau = 0.5$ 127

6.27 Constant phase lines, $\tau = 1.0$ 127

6.28 Constant phase lines, $\tau = 2.0$ 128

6.29 Constant phase lines, $\tau = 4.0$ 128

6.30 $|y|/x$ *vs.* θ for the first and second systems (by stationary phase analysis) 129

6.31 $|y|/x$ *vs.* θ for third system (by stationary phase analysis) 130

6.32 $\tan^{-1}(|y|/x)$ *vs.* θ for third system (by stationary phase analysis) . . 131

6.33 Bounding line angles α_1, α_2 and α_3 *vs.* τ (by stationary phase analysis) 132

6.34 Linear steady waves due to a translating source-sink pair, free surface domain ($0 \leq x \leq 11,\ \ 0 \leq y \leq 4.5$) 133

6.35 Linear waves due to a translating and oscillating source-sink pair, $\tau = 0.5$, free surface domain: ($0 \leq x \leq 11,\ \ 0 \leq y \leq 4.5$) 133

6.36 Nonlinear waves due to a translating and oscillating source-sink pair, $\tau = 0.5$, free surface domain: ($0 \leq x \leq 11,\ \ 0 \leq y \leq 4.5$) 134

6.37 Comparison of wave contour lines and constant phase lines for linear waves due to a translating and oscillating source-sink pair, $\tau = 1.0$. 134

6.38 Unsteady wake due to a translating and oscillating source-sink pair: $\tau = 0.5$, zero-mean strength, $t = 12.0$ 135

6.39 Unsteady wake due to a translating and oscillating source-sink pair: $\tau = 0.5$, zero-mean strength, $t = 12.5$ 136

6.40 Unsteady wake due to a translating and oscillating source-sink pair: $\tau = 0.5$, zero-mean strength, $t = 13.0$ 137

6.41 Unsteady wake due to a translating and oscillating source-sink pair: $\tau = 0.5$, zero-mean strength, $t = 13.5$ 138

6.42 Unsteady wake due to a translating and oscillating source-sink pair: $\tau = 0.5$, zero-mean strength, $t = 14.0$ 139

6.43 Wave elevation along symmetry plane: ($\tau = 0.5$, zero-mean strength, $12 < t < 14$) 140

6.44 Wave elevation along inner-angle wavepacket ($\beta = 14°$) ($\tau = 0.5$, zero-mean strength, $12 < t < 14$) 141

6.45 Peak wave amplitude within the diverging wave region in nonlinear steady wake 142

6.46 Peak wave amplitude within the interference region in nonlinear steady wake 142

6.47 Peak wave amplitude within the diverging wave region in linear steady wake 143

6.48 Peak wave amplitude within the interference region in linear steady wake 143

6.49 Peak wave amplitude within the inner-angle wavepacket in nonlinear unsteady wake 144

6.50 Peak wave amplitude within the inner-angle wavepacket in linear unsteady wake 144

6.51 Peak wave amplitude within the inner-angle wavepacket in the wake of the cutter Point Brower (experimental data of Brown *et al.* redrawn to show the algebraic decay rate) 145

A.1 Effect of restarting of GMRES on residual 156

A.2 Effect of multigrid on the convergence with GMRES 157

A.3 Effect of multigrid on the convergence with SOR 158

LIST OF APPENDICES

Appendix

A. Tests for Multigrid Method 152

B. Preconditioning of Equation (6.1) 159

CHAPTER I

INTRODUCTION

Problems involving nonlinearity of free surface waves in hydrodynamics have become of increasing interest since many wave phenomena cannot be explained by linear theories. For instance, in the generation of the solitons running away upstream of a disturbance moving near the critical speed in shallow water, the nonlinear effect plays an essential role (Wu & Wu 1982, Ertekin, Webster & Wehausen 1986). Another phenomenon is the observation that a ship traveling in deep water may generate a relatively steep, isolated wavepacket within the diverging portion of the Kelvin wake and the packet persists for a very large distance behind a ship. Although the mechanism responsible for this wave feature is not entirely clear, it is believed that nonlinear effects are important in the generation and persistence of the so-called inner-angle solitary wavepacket (Brown *et al.* 1989, Akylas, Kung & Hall 1988 and Hall & Buchsbaum 1990). Many aspects of other wave problems, such as the wave resistance of a ship and the motions of a ship in waves, require accurate computations accounting for nonlinear effects.

Since there are very limited problems for which analytic solutions can be easily found, a numerical method is necessary. Two major difficulties encountered in the study of nonlinear waves are that the free surface boundary conditions are nonlinear

and the free surface boundary is unknown *a priori*. Perturbation methods are most widely used to consider nonlinearity by including higher order terms in the free surface boundary condition. However, the boundary condition is still satisfied on the undisturbed flat free surface. Another alternative is to use an iterative procedure. For example, in the wave resistance calculations by Jensen, Mi & Söding (1986), the boundary condition is satisfied on a deformed free surface using an iterative procedure. In each iteration, a linearized boundary condition based on the solution from the last iteration is satisfied on the free surface determined from the last iteration. Their method is not suitable for unsteady waves.

The use of fully nonlinear and time-dependent free surface boundary conditions in numerical computations was introduced by Longuet-Higgins & Cokelet (1976) using a mixed Eulerian-Lagrangian method for two-dimensional surface waves. This procedure requires at each time step: 1) solving a boundary value problem, which itself is linear, in an Eulerian frame to obtain the velocity on the free surface; and 2) updating the free surface points, which construct the free surface, by integrating the nonlinear kinematic and dynamic free surface boundary conditions with respect to time. Variations of this method have been used for a variety of nonlinear free surface problems in two dimensions (Vinje & Brevig 1981 and Baker 1982) The method can be easily extended to three-dimensional problems. For example, the method was used by Dommermuth & Yue (1987) and Kang (1988) to solve several axisymmetric nonlinear free surface wave problems. Cao, Schultz & Beck (1990, 1991a, 1991b) used this time-stepping procedure combined with a desingularized boundary integral technique to study nonlinear waves caused by disturbances moving under the free surface.

The discretization of the free surface is necessary in numerical calculations. For the time-stepping procedure to be of practical use, it is important to have an effective solution method for the boundary value problem since it requires most of the computation time. A boundary integral method is powerful because it reduces the computational domain by one dimension. In conventional boundary integral formulations, the singularity of the fundamental solution is placed on the domain boundary. This requires special evaluation of singular integrands, which can result in costly numerical calculations.

If the singularity of the fundamental solution is placed away from the boundary and outside the domain of the problem, a desingularized boundary integral equation is obtained (von Kármán 1930, Kupradze 1967, Webster 1975, Heise 1978, Schultz & Hong 1989 and Cao *et al.* 1990, 1991a, 1991b). One immediate advantage of the desingularization is that the computational effort required for the evaluation of the integrals can be greatly reduced. However, there is a question about how to do the desingularization, or more precisely, how to select a proper desingularization distance.

In this thesis, the desingularized boundary integral method is re-examined and some of the above mentioned nonlinear wave problems are investigated using the desingularized method. A brief synopsis of each of the following chapters follows.

In Chapter 2, the initial-boundary value problem is formed for nonlinear free surface wave problems under the irrotational flow assumption. The solution procedure for the problem and the numerical implementation of the method are briefly described for waves generated by a free surface pressure disturbance or underwater disturbances (*e.g.* simple singularities and a submerged body).

Chapter 3, representing an incorporation of Cao, Schultz & Beck (1991a), re-examines the desingularized boundary integral method for some simple potential problems with the boundaries extending to infinity. The uniqueness of the solution and the convergence of the numerical solution to the desigularized integral equation are discussed. A formula to determine the desingularization distance is proposed. The effects of the desingularization distance, the mesh size and the truncation of boundary are tested. The method combined with Eulerian-Lagrangian time-stepping is also tested for the nonlinear waves generated by a simple source-sink pair moving below the free surface. The advantages of the desingularization is shown and discussed. The desingularized method is then used in the following chapters to study the wave problems mentioned above.

Chapter 4, an extension of the work by Cao, Schultz & Beck (1991b), deals with upstream runaway solitons generated by a surface pressure or a bottom topography moving near the critical speed in two-dimensional shallow water. The solution by the desingularized method is compared to the forced KdV (fKdV) solution (Wu 1987). The difference between the waves caused by the surface pressure and those caused by bottom topography with identical forcing distribution in the fKdV model is compared using the fully nonlinear model. The waves caused by submerged cylinders, which cannot be handled by the fKdV model, are also studied using the fully nonlinear model.

Chapter 5, representing an incorporation of Cao, Schultz & Beck (1990), studies the three-dimensional waves generated by a submerged spheroid moving below the free surface. The wave elevation, the pressure and forces on the spheroid are calculated and compared to the results by other theories or methods.

In Chapter 6, the mechanism of the generation of the inner-angle wavepackets in the wake of a ship is studied. Particularly, the effects of the nonlinear free surface boundary conditions and the unsteadiness of the wake is examined. The wake is studied with nonlinear wave calculations using the desingularized method, linear wave calculations using the time-domain Green function (Liapis & Beck 1986, King 1987, Beck & Magee 1990), and a stationary phase method. The results of the three methods are compared and also compared to the experimental data (Brown *et al.* 1989). In the nonlinear calculations, a large computational domain on the free surface is required because of our interest in the far field, resulting in a large number of unknowns in the numerical computations (typically $N > 3000$). Some numerical techniques for a fast iterative solution of the discretized boundary integral equation are tested. These techniques include a fast iterative solver GMRES (Saad 1986 and Olson 1989), a specially chosen precoditioning matrix, a multigrid method, as well as the vectorization of the computer program for computations on supercomputer. Finally, we make conclusions and recommendations in Chapter 7.

CHAPTER II

PROBLEM FORMULATION AND SOLUTION PROCEDURE

In this chapter, the initial boundary value problem is formed for nonlinear problems of waves generated by a free surface pressure disturbance or the motion of a rigid body moving under the free surface. The solution procedure and the numerical implementation are described. It is assumed that the fluid is incompressible and inviscid and the flow is irrotational. This implies the existence of a velocity potential $\phi(\mathbf{x},t)$ with the fluid velocity $\mathbf{u}$ given by $\mathbf{u}(\mathbf{x},t) = \nabla\phi$, where $\mathbf{x} = (x,y,z)$ is the spatial location and t is time. The surface tension is neglected.

2.1 Initial-Boundary Value Problem

2.1.1 Governing equation

The coordinate system used is shown in Figure 2.1, in which the $z = 0$ plane represents the mean position of the free surface and the z axis points upwards. The problem under consideration is the flow generated by the motion of a rigid body or singularity below the free surface, or a free surface pressure distribution, or a combination of the two. The fluid domain D is bounded on top by the free surface S_f, internally by the hull of the body S_h, below by a bottom surface S_b and an

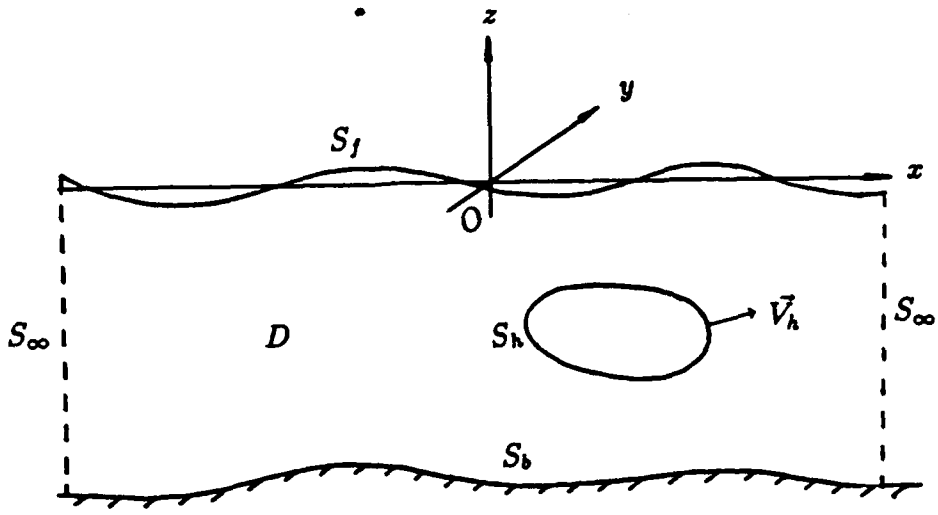


Figure 2.1: Problem definition and coordinate system

enclosing contour S_∞ at infinity.

Because of the existence of the velocity potential ϕ, the continuity equation requires that the potential ϕ satisfies the Laplace equation,

$$\Delta\phi = 0 \qquad \text{(in } D\text{)}. \tag{2.1}$$

It is well known that the momentum equation yields Bernoulli's equation for the irrotational flow,

$$\frac{p}{\rho} = -\frac{\partial\phi}{\partial t} - gz - \frac{1}{2}|\nabla\phi|^2 \qquad \text{(in } D\text{)}. \tag{2.2}$$

This means that the solution procedures for the velocity potential ϕ and the pressure p are uncoupled. Usually, the ϕ is first solved with proper boundary conditions and initial conditions. Then p can be easily calculated using (2.2).

2.1.2 Boundary and initial conditions

Since the free surface boundary is not known *a priori*, two boundary conditions are required on it. The kinematic condition requires that a fluid particle on the free

surface will remain on it,

$$\frac{\partial \eta}{\partial t} + \frac{\partial \phi}{\partial x}\frac{\partial \eta}{\partial x} + \frac{\partial \phi}{\partial y}\frac{\partial \phi}{\partial y} - \frac{\partial \phi}{\partial z} = 0 \qquad (\text{on } S_f). \tag{2.3}$$

where $\eta = \eta(x, y, t)$ is the free surface elevation. The dynamic condition requires that the pressure on the free surface equals the ambient pressure p_a, neglecting the surface tension,

$$p = p_a(x, y, t). \qquad (\text{on } S_f) \tag{2.4}$$

The ambient pressure $p_a(x, y, t)$ is assumed given and can be time and space dependent. Expressing (2.4) in terms of ϕ with the use of (2.2) on the free surface, we obtain,

$$\frac{p_a}{\rho} = -\frac{\partial \phi}{\partial t} - g\eta - \frac{1}{2}|\nabla \phi|^2 \qquad (\text{on } S_f). \tag{2.5}$$

Eqs. (2.3) and (2.5) are the Eulerian description of the free surface boundary conditions. By re-arranging Eqs.(2.3) and (2.5), we obtain the Lagrangian description of the free surface conditions,

$$\frac{D\vec{X}_f}{Dt} = \nabla \phi \qquad (\text{on } S_f) \tag{2.6}$$

$$\frac{D\phi}{Dt} = -\frac{p_a}{\rho} - gz_f + \frac{1}{2}|\nabla \phi|^2 \qquad (\text{on } S_f). \tag{2.7}$$

where

$$\frac{D}{Dt} = \frac{\partial}{\partial t} + \nabla \phi \cdot \nabla$$

is the substantial derivative following a fluid particle and $\vec{X}_f = (x_f, y_f, z_f)$ is the position vector of a free surface particle.

Depending on the problem to be solved, one description can be more convenient to use than the other. For instance, if breaking waves or overturning waves are studied, the Lagrangian description is more convenient because the wave elevation becomes

multivalued. The Eulerian description can be advantageous since the nodal spacing may be kept uniform and free surface regriding is not necessary. In the Lagrangian formulation the regriding may be necessary to avoid the numerical instabilities due to largely-uneven spacing. We will use the Lagrangian description since it has some other advantages in the sense of the numerical wave computations, which will be shown in the following chapters.

On the body surface S_h and the bottom S_b the flow satisfies the non-penetration condition,

$$\frac{\partial \phi}{\partial n_h} = \vec{V}_h \cdot \vec{n}_h \qquad (\text{on } S_h) \tag{2.8}$$

$$\frac{\partial \phi}{\partial n_b} = \vec{V}_b \cdot \vec{n}_b \qquad (\text{on } S_b), \tag{2.9}$$

where $\vec{V}_h$ and $\vec{V}_b$ are the velocities of body surface and the bottom surface, and $\vec{n}_h$ and $\vec{n}_b$ are the exterior unit normal vectors to the two surfaces, respectively.

At infinity, a proper far-field condition is required. For a three-dimensional initial-boundary value problem, $\phi \to 0$ or $\nabla\phi \to 0$ implies that the flow due to a disturbance vanishes at infinity.

In our time-dependent problems, we study the flow generated by disturbances starting from rest. Therefore, for initial conditions, we require

$$\phi = 0 \qquad (\text{in } D \text{ for } t \leq 0)$$

and

$$\eta = \eta_o(x, y) \qquad (\text{on } S_f \text{ for } t \leq 0), \tag{2.10}$$

where η_o is a known initial free surface elevation.

The mathematical formulation used here can model the waves generated by one of four disturbances or any combination of them: 1) the motion or deformation of a body

in the water; 2) the deformation of the bottom surface; 3) the free surface pressure distribution; and 4) an initial free surface elevation. For a particular problem, it is not necessary that all surfaces exist. For example, if the waves are generated by the free surface pressure disturbance, surface S_h does not need to exist. S_b does not exist if the fluid is in deep water.

The mathematical formulation is exact under the potential flow assumption. No additional assumptions are made, such as the linearization of the free surface conditions. The problem is fully nonlinear because of the nonlinear free surface conditions. The body and bottom boundary conditions are exact although they are linear.

2.2 Solution Procedure for Nonlinear Waves

2.2.1 Solution procedure

As mentioned in the introduction, two major difficulties encountered in the study of nonlinear waves are that the free surface boundary conditions are nonlinear and the free surface boundary is unknown *a priori*. There are very few problems (usually with simple boundary geometry) for which analytic solutions can be found. A numerical method is necessary for practical computations.

To account for the nonlinearity, a perturbation method can be used that includes higher-order terms in the series expansion of the free surface boundary conditions. This method has been a powerful tool in the analytical study of nonlinear waves (Lamb 1929, Stoker 1957, Wehausen & Laitone 1960, and Whitham 1974). The perturbation method has also been used in numerical calculations by researchers, for example, Nakos & Sclavounos (1990) in the calculation of ship motions in waves. In most cases, the boundary conditions are not satisfied on the real free surface but on

a flat mean free surface. An iterative procedure can be used to satisfy the nonlinear free surface conditions. In the work of Jensen, Mi & Söding (1986) and Jensen, Bertram & Söding (1989), a linearized boundary condition based on the solution from the last iteration is satisfied on the deformed free surface determined from the previous iteration. However, their methods are not suitable for unsteady waves.

Longuet-Higgins & Cokelet (1976) first introduced the mixed Eulerian-Lagrangian method for two-dimensional water waves using fully nonlinear free surface boundary conditions satisfied on the actual free surface in numerical computations. This is a time-stepping procedure which requires two major tasks at each time instant:

1. solving a boundary value problem, which itself is linear, in an Eulerian frame to obtain the velocity on the free surface; and

2. updating the positions of the free surface particles and the velocity potential on the surface by integrating the nonlinear kinematic and dynamic free surface boundary conditions with respect to time.

Variations of this method have been used for a variety of two-dimensional and three-dimensional nonlinear free surface problems (Vinje & Brevig 1981, Baker 1982, Lin 1984, Dommermuth & Yue 1987, Kang 1988 and Cao, Schultz & Beck 1990, 1991a, 1991b).

The boundary value problem at each time step is,

$$\Delta\phi = 0 \qquad (\text{in } D) \tag{2.11}$$

$$\phi = \phi_o \qquad (\text{on } S_{f_o}) \tag{2.12}$$

$$\frac{\partial\phi}{\partial n_h} = \vec{V}_h \cdot \vec{n}_h \qquad (\text{on } S_h) \tag{2.13}$$

$$\frac{\partial \phi}{\partial n_b} = \vec{V}_b \cdot \vec{n}_b \qquad \text{(on } S_b\text{)} \tag{2.14}$$

and

$$\nabla \phi \to 0 \qquad \text{(as } \mathbf{x} \to \infty\text{)}. \tag{2.15}$$

where ϕ_o and S_{f_o} are known from the previous time steps.

After solving the boundary value problem, the flow is known for the present time. The velocities of the free surface particles can be calculated and the free surface position S_{f_o} and the potential ϕ_o on it can be predicted for the next time step by integrating the free surface kinematic and dynamic conditions (2.6) and (2.7). The pressure on the body S_h and S_b can be calculated using the Bernoulli's equation (2.2),

$$\begin{aligned} \frac{p}{\rho} &= -\frac{\partial \phi}{\partial t} - gz - \frac{1}{2}|\nabla \phi|^2 \\ &= -\frac{d\phi}{dt} - gz - (\frac{1}{2}\nabla \phi - \vec{V}) \cdot \nabla \phi \qquad \text{(on } S_h \text{ or } S_b\text{)}, \end{aligned} \tag{2.16}$$

where

$$\frac{d\phi}{dt} = (\frac{\partial \phi}{\partial t} + \vec{V} \cdot \nabla)\phi$$

is the substantial derivative of the potential at a fixed point on S_h or S_b following the motion of that point and $\vec{V}$ is the velocity of that point (*i.e.* $\vec{V} = \vec{V}_h$ or $\vec{V}_b$). The second form of (2.16) is more appropriate to use because the nodal points must move to follow the boundary. The forces and the moments on the body can be calculated by integrating the pressure over the the body surface,

$$\vec{F} = \int\int_{S_h} -p\vec{n}_h ds, \tag{2.17}$$

and

$$\vec{M} = \int\int_{S_h} -p(\vec{r} \times \vec{n}_h) ds. \tag{2.18}$$

where $\vec{r}$ is the position vector of a body surface point to a reference point (usually the centroid of the body).

2.2.2 Numerical implementation

The boundary value problem (2.11 – 2.15) has to be solved by a numerical method. Many methods, such as finite difference methods, finite element methods and boundary integral methods, are available. A review of numerical methods for free surface flows is given in Yeung (1982). It is very important to choose an effective solution method for the boundary value problem since its solution requires most of the computation time. A boundary integral method is powerful because it reformulates the original problem as an integral equation on the domain boundary thus reducing the computational domain by one dimension. We use a desingularized boundary integral method to solve (2.11 – 2.15). Although the method is not as widely used as conventional singular boundary integral methods because of lack of a uniqueness and completeness theorem, it has many potential advantages over the singular methods and has received more attention recently. In Chapter 3, the desingularized method is re-examined and tested with some simple problems. It is shown that the desingularized method is faster, easier to implement (especially easy to take advantage of vector and parallel computers) and can be more accurate for many problems. Therefore, this method is used in the nonlinear wave problems studied in Chapters 4, 5 and 6.

The time integration of the free surface boundary conditions (2.6) and (2.7), which are first-order ordinary differential equations with respect to time, are integrated with a widely used fourth-order Runge-Kutta-Fehlberg method. This method

has been shown to be very accurate and stable. The subroutine can be found in ODE-PACK. An initial time increment is set, but is modified by the Runge-Kutta-Fehlberg subroutine where appropriate to satisfy an error tolerance.

CHAPTER III

DESINGULARIZED BOUNDARY INTEGRAL METHOD

A boundary integral equation method employs a fundamental solution, which satisfies the differential equation (and possibly part of the boundary conditions), to reformulate the original boundary value problem as an integral equation on the boundary. In conventional boundary integral formulations, singularities of the fundamental solution are placed on the domain boundary. This requires special evaluation of singular integrands, which can result in costly numerical calculations. In the time-dependent procedure for nonlinear free surface problems, the boundary integral equation needs to be solved at each time step. Since most of the computation time is devoted to the boundary integral problem, an effective solution method is critical in the time-stepping procedure.

When the singularity of the fundamental solution is placed away from the boundary and outside the domain of the problem, a desingularized boundary integral equation is obtained. Similar to the singular formulation of boundary integral equations, the non-singular formulation also has two versions: the direct method and the indirect method. In the direct method, Green's second identity is used to derive the boundary integral equation, and the solution of the problem is obtained directly

by solving the boundary integral equation. In the indirect method, the solution is constructed by a singularity distribution outside the problem domain and a boundary integral equation for the strength of the singularities is formulated to satisfy the boundary condition. After the strength is determined, the flow can be easily calculated.

One immediate advantage of the desingularization is that simple quadrature can be used to evaluate the integrals since the integrals are non-singular, thus reducing the computational time in obtaining the algebraic system representing the discretized boundary integral equation. It has also been shown that the desingularized boundary integral equation can give more accurate solutions for a given truncation in some problems (Webster 1975, Schultz & Hong 1989).

The first use of a desingularization method is the classical work by von Kármán (1930) that determines the flow about an axisymmetric body using an axial source distribution. The strength of the source distribution is determined by the kinematic boundary condition on the body surface. Kupradze (1967) proposes a non-singular formulation of the direct boundary integral equation for the exterior Dirichlet problem with an auxiliary control surface outside the problem domain. Heise (1978) studies some numerical properties of integral equations in which the singular points are on an auxiliary boundary outside the solution domain for plane elastostatic problems. By applying Green's theorem to the solution and a simple linear wave source with the singular point lying inside the body (i.e., outside the problem domain) and using a bilinear expansion of the source, Martin (1981) obtains the so-called "null-field equations for the water wave radiation problems". Johnston & Fairweather (1984) and Han & Olson (1987) use an adaptive method in which the singularities

are located outside the domain and allowed to move as part of the solution process. This adaptive method requires considerably fewer singularities than the number of boundary nodes, but it results in a system of nonlinear algebraic equations for both the strength and the location of the singularities.

Webster (1975) gives a discussion on the numerical properties of the desingularization technique for the external potential flow of an arbitrary, three-dimensional smooth body. Triangular panels of a simple source distribution are placed somewhat inside the surface of body. The integration is performed analytically for each panel using a bilinear distribution of the singularity strength. These integrations require evaluation of (logarithmic and arctangent) transcendental functions. From the numerical results, Webster concludes that "submergence of the singularity sheet below the surface of the body appears to improve greatly the accuracy, as long as the sheet is not submerged too far". This indicates that for a certain discretization of the body surface, a more accurate solution may be obtained using the non-singular formulation than the singular formulation. Although Webster did not attempt it, a simple numerical quadrature can be used if the desingularization distance is sufficiently large. This will significantly reduce the computational effort to obtain the algebraic system.

Although the non-singular formulation of the indirect method has grown popular recently, few studies on the non-singular direct method have been reported, especially for three-dimensional problems. Schultz & Hong (1989) obtain a non-singular direct formulation by moving the singularity in the Cauchy's integral away from the boundary in two-dimensional potential problems. Their results show the advantages of the non-singular formulation. They also use an overdetermined system combin-

ing the real and imaginary parts of Cauchy's theorem or using "extra" evaluation points away from the boundary contour. This overdetermined system can exhibit higher-order convergence than the determined system from either the real part or the imaginary part of Cauchy's theorem. Few investigations on applications with boundaries extending to infinity, especially for water wave problems, have been reported. The work of Jensen, Mi & Söding (1986) solving the steady nonlinear ship wave problem using a Rankine source distribution above the free surface can be considered as an application of the indirect desingularized method.

The direct and indirect desingularized methods are formulated in the following sections. The effect of desingularization distance is examined for a simple problem with an infinitive and flat boundary. The convergence of the method with respect to mesh size and computational time are compared to find the "optimum" desingularization distance (will be discussed in more detail later). This "optimum" distance will then be used for the simulations of unsteady nonlinear waves in the following chapters.

3.1 Desingularized Integral Equations

The Laplace equation is the governing equation in a domain D bounded by Γ. A Dirichlet condition is imposed on part of the boundary Γ_d and a Neumann condition on the remaining boundary Γ_n. Therefore, one has the following mixed boundary value problem:

$$\Delta\phi = 0 \qquad (\text{in } D), \tag{3.1}$$

$$\phi = \phi_o \qquad (\text{on } \Gamma_d), \tag{3.2}$$

$$\frac{\partial\phi}{\partial n} = \chi \qquad (\text{on } \Gamma_n), \tag{3.3}$$

where ϕ_o and χ are known functions. If the boundary extends to infinity, a far-field condition is required. The desingularized boundary integral method separates the integration and control (i.e., evaluation) surfaces, one of which is the boundary of the problem. In the direct method, the boundary of the problem is the integration surface, while in the indirect method, the boundary is the control surface.

3.1.1 Direct method

The boundary integral equation in the direct method is derived from Green's second identity:

$$\int\int\int_D (\phi\Delta\psi - \psi\Delta\phi)\, dD - \int\int_\Gamma \left(\phi\frac{\partial\psi}{\partial n} - \psi\frac{\partial\phi}{\partial n}\right) d\Gamma = 0, \tag{3.4}$$

which holds for any two functions with second derivatives continuous in D and the boundary Γ. If ϕ is the solution and ψ is chosen as

$$\psi = \frac{1}{\left|\vec{X}_p - \vec{X}_q\right|}, \tag{3.5}$$

with its evaluation point $\vec{X}_p$ outside D and integration point $\vec{X}_q$ on Γ, the volume integral in (3.4) vanishes. Equation (3.4) then becomes

$$\int\int_\Gamma \left(\phi\frac{\partial\psi}{\partial n} - \psi\frac{\partial\phi}{\partial n}\right) d\Gamma = 0. \tag{3.6}$$

Applying the boundary conditions (3.2) and (3.3) to (3.6) and moving the known quantities to the right-hand side gives:

$$\begin{aligned}\int\int_{\Gamma_n} \phi(\vec{X}_q)\frac{\partial}{\partial n}\left(\frac{1}{\left|\vec{X}_p - \vec{X}_q\right|}\right) d\Gamma - \int\int_{\Gamma_d} \frac{1}{\left|\vec{X}_p - \vec{X}_q\right|}\frac{\partial\phi(\vec{X}_q)}{\partial n} d\Gamma \\ = -\int\int_{\Gamma_d} \phi_o\frac{\partial}{\partial n}\left(\frac{1}{\left|\vec{X}_p - \vec{X}_q\right|}\right) d\Gamma + \int\int_{\Gamma_n} \frac{1}{\left|\vec{X}_p - \vec{X}_q\right|}\chi\, d\Gamma.\end{aligned} \tag{3.7}$$

The kernels are non-singular since $\vec{X}_p$ and $\vec{X}_q$ never coincide. The integral equation (3.7) is solved for ϕ on Γ_n and $\partial\phi/\partial n$ on Γ_d.

The fundamental solution $\frac{1}{|\vec{X}_p-\vec{X}_q|}$ can easily be replaced by other higher-order singularities (dipole, etc.) with little additional computational effort since the integrals are non-singular and can be evaluated numerically.

3.1.2 Indirect method

In the indirect method, the solution is constructed by a simple Rankine source distribution over some surface Ω outside the problem domain,

$$\phi(\vec{X}) = \int\int_{\Omega} \sigma(\vec{X}_s)\frac{1}{|\vec{X}-\vec{X}_s|}d\Omega, \tag{3.8}$$

which satisfies Laplace's equation. By applying the boundary conditions, (3.2) and (3.3), one obtains a boundary integral equation for the unknown strength of the singularities, $\sigma(\vec{X}_s)$,

$$\int\int_{\Omega} \sigma(\vec{X}_s)\frac{1}{|\vec{X}_c-\vec{X}_s|}d\Omega = \phi_o(\vec{X}_c) \qquad (\vec{X}_c \in \Gamma_d) \tag{3.9}$$

and

$$\int\int_{\Omega} \sigma(\vec{X}_s)\frac{\partial}{\partial n}\left(\frac{1}{|\vec{X}_c-\vec{X}_s|}\right)d\Omega = \chi(\vec{X}_c) \qquad (\vec{X}_c \in \Gamma_n), \tag{3.10}$$

where $\vec{X}_s$ is the integration point, and $\vec{X}_c$ the control point on the real boundary. Once the singularity strength is solved, the solution ϕ can be determined.

Similarly, $\frac{1}{|\vec{X}_c-\vec{X}_s|}$ can easily be replaced by higher-order fundamental solutions.

3.2 Uniqueness of Desingularized Integral Equation and Convergence of the Numerical Methods

The existence of the solution to the direct version of the desingularized boundary integral equation is obvious as long as the original boundary value problem is well-posed and has a unique solution according to the Green's theorem.

Kupradze (1967) gives a proof of the uniqueness of the solution to the direct version of the desingularized boundary integral equation for exterior Dirichlet problems and proposes an approximate solution method in which the solution is expressed as

$$\frac{\partial \phi}{\partial n} = \sum_{k=1}^{N} C_k \omega_k(\vec{X}_p) \tag{3.11}$$

where

$$\omega_k(\vec{X}_p) = \frac{1}{|\vec{X}_p - \vec{X}_{q_k}|} \qquad (k = 1, 2, ...) \tag{3.12}$$

is a linearly independent and complete set. $\vec{X}_p$ is the point on the real boundary and $\vec{X}_{q_k}$ $(k = 1, 2, 3, ...)$ are points covering the auxiliary boundary everywhere "densely". Substituting (3.11) into the desigularized equation gives a system of linear algebraic equations for C_k $(k = 1, N)$. This, in fact, is a kind of collocation method where $\vec{X}_{q_k}$ is the collocation point. Kupradze proves the convergence of the method. However, this method may not be very effective in practice since each element of the coefficient matrix and the right hand side of the linear system requires an integration over the whole real boundary that will still be very time consuming although the integrands are non-singular. Also, in his method, the auxiliary boundary does not change as N changes, which may cause numerical instabilities as N becomes large.

A simple collocation method is used here to solve the integral equations. In the direct method the Green's theorem is evaluated at chosen collocation points on

the auxiliary boundary, while in the indirect method the boundary conditions are satisfied at the collocation points on the real boundary. The integration surface (the real boundary in the direct method or the auxiliary boundary in the indirect method) is divided into panels, and the integration is carried out for each panel assuming some kind of distribution of the solution or source strength. Therefore, each element in the coefficient matrix of the resulting linear system requires integrations over a small number of the nearby panels. This will reduce the computation time significantly.

The convergence of a numerical method requires that the numerical solution approach the exact solution as the computational grid is refined. To ensure the convergence, the non-dimensional desingularization distance of a singular point (outside the domain and normal to the boundary) is proposed to be given by

$$L_d = l_d(D_m)^\nu, \tag{3.13}$$

where l_d is a parameter independent of the discretization (l_d will be termed the desingularization factor) which reflects how far the integral equation is desigularized, D_m is the local mesh size (usually the square root of the local mesh area in a three-dimensional problem) and ν is a parameter that affects the accuracy of the numerical integration.

The use of (3.13) implies that the desingularization distance is related to the local mesh size. As the mesh becomes finer, the singular point becomes closer to the boundary for $\nu > 0$. In the limit, the non-singular formulation is consistent with the singular formulation although the kernels do not become singular and the desigularized integral equations are expected to have similar properties as the singular boundary integral equations. Numerically, the use of the desingularization distance (3.13) with $\nu > 0$ is also advantageous over the case when $\nu = 0$ since the condition

number of the coefficient matrix of the desingularized equations will deteriorate less rapidly as the mesh is refined.

Desingularization increases the condition number of the coefficient matrix for a given truncation. Webster (1975) shows that non-singular formulations are not significantly less well conditioned than singular formulations if the desingularization is not too large. In most three-dimensional computations, the large number of unknowns requires an iterative solution of the linear system. As the desingularization increases, the condition number also increases. Thus, an increase in the number of iterations in solving the algebraic system is expected. There appears to be an "optimum" desingularization distance: if the singularity is too far from the boundary, the linear system will be poorly conditioned and numerical instabilities occur; if the singularity is too close to the boundary, numerical integration of the increasingly singular kernel is suspect and the solution may not be accurate. The "optimum" l_d and proper ν will be determined by numerical tests for simple problems.

3.3 Simple Test Examples

To test the convergence of the numerical integration with respect to the mesh refinement, the potential due to a known constant normal dipole distribution within a square, flat surface ($-1 < x < 1, -1 < y < 1, z = 0$) is considered. The potential is evaluated at a point above the center of the surface at a distance given by (3.13) with $l_d = 1$. The surface is divided into square panels and a 2×2 Gaussian quadrature is used for each panel. A third-order convergence should be found assuming the integrand is non-singular and is independent of the mesh (*i.e.* $\nu = 0$). For $\nu > 0$, (3.13) makes the integrand depend on the mesh size, and hence the third-order convergence is not assured. Fig. 3.1 shows the convergence of the numerical integration for three

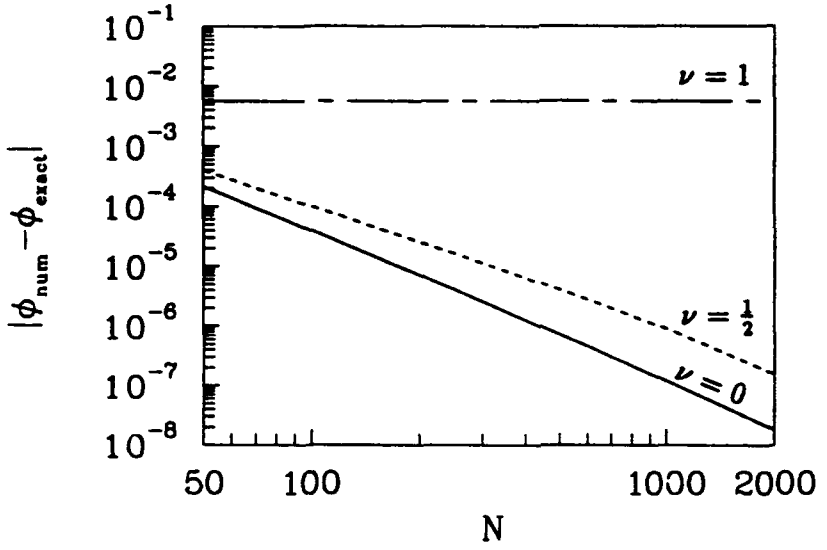


Figure 3.1: Convergence of numerical integration

values of ν: 0, 1/2 and 1. As can be seen, the numerical integration error increases with ν. However, ν should be greater than 0 for the convergence of the solution of the integral equation. Therefore, an appropriate ν lies in between 0 and 1. $\nu = 1/2$ is chosen for the subsequent calculations.

The numerical performance of the desingularized boundary integral methods is tested for a problem in which the potential is generated by a dipole below an infinitive flat plane with $\phi = 0$. This simple problem has an exact solution formed by the dipole and its negative image about the flat plane. This problem represents the solution to the first time step of nonlinear waves caused by an impulsive disturbance of a dipole under water. The method is then tested for simple time-dependent nonlinear waves caused by a moving source-sink pair under the free surface.

The direct and indirect methods are compared in this example. In the direct method, the boundary is divided into panels, and a solution is sought at the nodes. Since the kernels are non-singular, the panel integrals can be evaluated using Gaussian quadrature, where the solution is assumed to be bilinear over each panel. In the indirect method, the integrals of the singularity distribution (3.8) is replaced by a summation of concentrated singularities without an apparent loss of accuracy when the desingularization distance is appropriate. Therefore, the computations will be less complex and time consuming than in the direct method.

In the results that follow, the Generalized Minimal Residual Method (GMRES), Saad & Schultz (1986) and Olson (1989), is used to iteratively solve the system of equations. It is found that this method to be generally twice as fast as a standard conjugate gradient routine for nonsymmetric matrices. A sufficiently small value of the convergence tolerance is chosen so that it introduces negligible error in comparison to that introduced by truncation. The computations are carried out using double precision on an Apollo DN10000 workstation.

3.3.1 A dipole below a $\phi = 0$ infinitive flat plane

In this example, a Dirichlet condition, $\phi = 0$, is imposed on the $z = 0$ plane. A dipole of unit strength is located at $\vec{X}_o(0, 0, -1)$, and the direction of the dipole coincides with the x axis. The normal derivative $\partial\phi/\partial n$ is sought on $z = 0$. The problem is symmetric about the $y = 0$ plane. The computations take advantage of this symmetry.

Since the potential at the dipole location is singular for this problem, the solution

is decomposed into a regular part and a singular part:

$$\phi(\vec{X}_p) = \tilde{\phi}(\vec{X}_p) - \frac{x_p}{|\vec{X}_p - \vec{X}_o|^3}. \tag{3.14}$$

For the direct method, we apply (3.7) for $\tilde{\phi}$ and recognize the Γ_n is absent and far-field closure does not contribute. Substituting back for ϕ gives

$$\int\int_{\Gamma_d} \frac{\partial \phi}{\partial n} \frac{1}{|\vec{X}_p - \vec{X}_q|} d\Gamma_1 = \frac{x_p}{|\vec{X}_p - \vec{X}_o|^3} \quad , \tag{3.15}$$

where $\vec{X}_p = (x_p, y_p, z_p)$ is the control point outside D, and $\vec{X}_q$ the integration point on Γ_d ($z = 0$). The computational domain, the truncation of Γ_d by $x = \pm R_\infty$ and $y = \pm R_\infty$, is discretized into a uniform square mesh defined by N node points. The mesh configuration is shown in Fig. 3.2. The integrations assume a bilinear distribution of $\partial\phi/\partial n$ and use a Gaussian quadrature. The control points $\vec{X}_p$ are placed directly above the node points at a distance $L_d = l_d(\Delta X)^{1/2}$, where ΔX is the side of a square panel.

For the indirect method, we construct the potential using (3.9), with the integration replaced by summation as discussed previously, supplemented with the singular dipole term

$$\phi(\vec{X}) = \frac{-1}{4\pi} \frac{x}{|\vec{X} - \vec{X}_o|^3} + \sum_{i=1}^{N} \frac{\sigma_i}{|\vec{X} - \vec{X}_{si}|} \quad , \tag{3.16}$$

where $\vec{X}_{si}$ are the source points above $z = 0$. The boundary condition $\phi = 0$ on $z = 0$ results in

$$\sum_{i=1}^{N} \frac{\sigma_i}{|\vec{X}_c - \vec{X}_{si}|} = \frac{1}{4\pi} \frac{x_c}{\left(x_c^2 + y_c^2 + (z_c + 1)^2\right)^{3/2}} \quad , \tag{3.17}$$

where $\vec{X}_c = (x_c, y_c, z_c)$ is the control point on $z = 0$.

The exact solution for $\phi(\vec{X})$ is

$$\phi(x, y, z) = \frac{-1}{4\pi} \frac{x}{\left(x^2 + y^2 + (z + 1)^2\right)^{3/2}} + \frac{1}{4\pi} \frac{x}{\left(x^2 + y^2 + (z - 1)^2\right)^{3/2}} \quad . \tag{3.18}$$

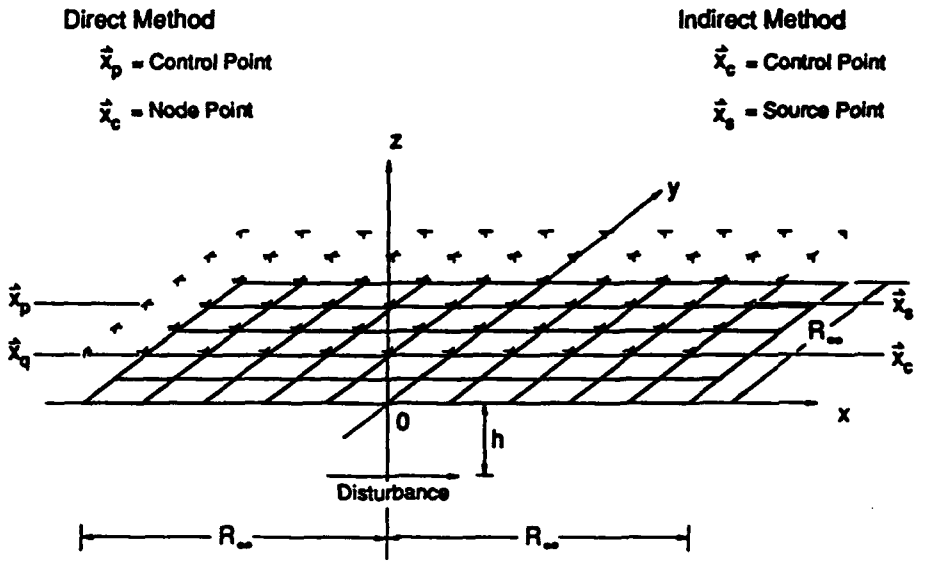


Figure 3.2: Schematic diagram of a dipole below a $\phi = 0$ infinitive flat plane

The exact normal derivative of ϕ on the $z = 0$ plane then is

$$(\frac{\partial \phi}{\partial n})_{exact} = \frac{3}{2\pi} \frac{x}{(x^2 + y^2 + 1)^{5/2}} \quad . \tag{3.19}$$

The numerical solution for the normal derivative of ϕ is compared to (3.19) by the RMS error measurement defined by

$$E_{rms} = \sqrt{\frac{1}{N} \sum_{i=1}^{N} \left((\frac{\partial \phi}{\partial n})_{exact} - (\frac{\partial \phi}{\partial n})_{num} \right)^2} \quad . \tag{3.20}$$

Fig. 3.3 shows the RMS error as a function of l_d for three truncations. In the direct method, in which a 2×2 Gauss quadrature is used to evaluate the influence function, the RMS error increases as l_d increases. In the indirect method, the solution breaks down $l_d = 0$ because the integration and control points coincide. However, as l_d increases, the RMS error decreases rapidly and remains rather insensitive to l_d for quite a large range. Eventually, l_d becomes too large for the given truncation

to represent the second term in (3.18) well, and the error starts to increase. It is interesting that desingularization in the indirect method greatly reduces error and gives smaller error than in the direct method for a large range of l_d. One of the reasons is that solution of many problems can be represented accurately by a finite number of some singularities located outside the problem domain. In this example, one negative image dipole above the $z = 0$ plane results in the exact solution. The direct method seems to be less sensitive to the desingularization.

The effect of different quadratures to evaluate the coefficient matrix for the direct method is given in Fig. 3.4. As expected, for small l_d, the analytic integration by the approach given in Newman (1986) produce smaller RMS error than the Gaussian quadrature because the integration error dominates the accuracy of the solution. As l_d increases, the Gaussian quadrature integrates the smoother integrands accurately, and the results merge to those using the analytic integration. It is fortuitous that in the intermediate range of l_d, the results using the Gaussian quadrature show less error than those using the analytic integration—the discretization and quadrature errors seem to partially cancel each other. A more accurate 3×3 Gaussian quadrature brings the results closer to those using the analytic integration, as expected. For the singular direct method ($l_d = 0$ in Fig. 3.4), the analytic integration gives the least error as expected.

The effect of desingularization on the condition number of the algebraic system is shown in Fig. 3.5. As expected, the condition number increases with l_d. However, a poorly-conditioned system does not necessarily imply an inaccurate solution as long as l_d is not too large. In our example, minimal error occurs around $l_d = 3.0$ in the indirect method, where the condition number is quite large.

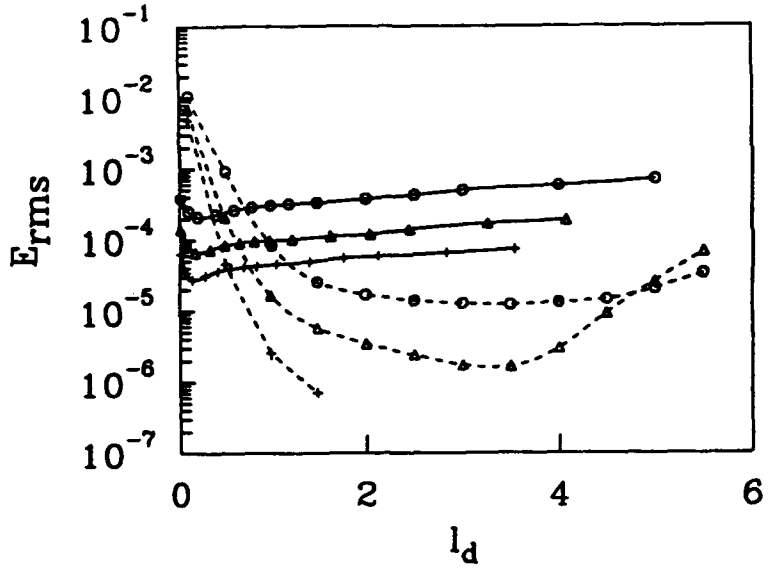


Figure 3.3: Effect of desingularization ($R_\infty = 6.6667$):
o : $N = 231$; $\triangle$:$N = 496$; +: $N = 861$;
—— direct method; - - - - indirect method

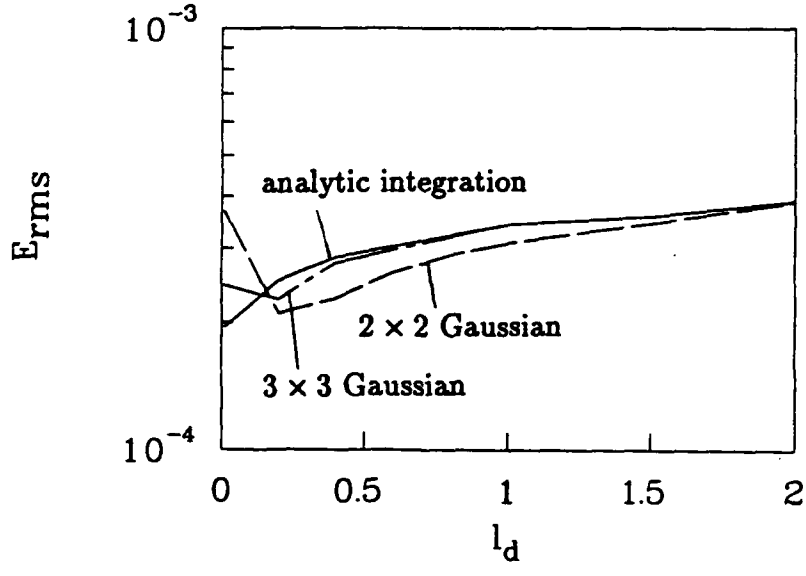


Figure 3.4: Comparisons between Gaussian quadrature and analytic integration ($R_\infty = 6.6667$, $N = 231$)

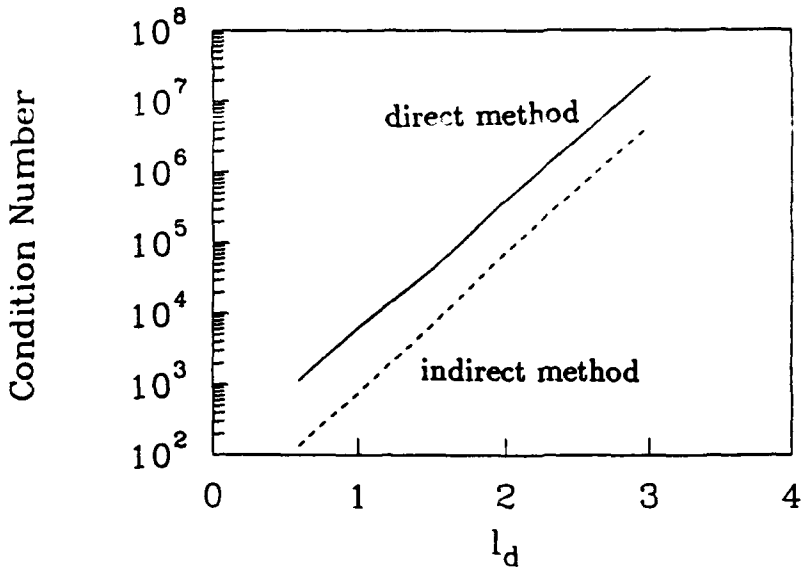


Figure 3.5: Effect of desingularization on condition number
($R_\infty = 6.6667$, $N = 231$)

Fig. 3.6 compares the ratios of the CPU time by the GMRES to that by an LU algorithm for the direct method with 231 unknowns as a function of l_d. The LU algorithm takes about 3.5 seconds to solve the matrix equation. An error tolerance ϵ for the least squares residual of the equations needs to be specified when the GMRES is used. We find that $\epsilon = 10^{-5}$ is sufficiently small in all the computations performed in this example. With the use of this tolerance, the CPU time by the GMRES is less than that by the LU algorithm for $l_d < 1.5$. The analytic integration requires about 22 seconds to set up the matrix while the 2×2 Gaussian quadrature requires only about 6.4 seconds, for a savings of about 70 percent. The CPU time for solving the matrix equation by the GMRES varies from 3.0 seconds to 4.0 seconds as l_d changes from 0.8 to 3.0. Even in the worst case, $l_d = 3.0$, we have a total reduction in the CPU time of about 60 percent over the singular formulation (with $l_d = 0$ and

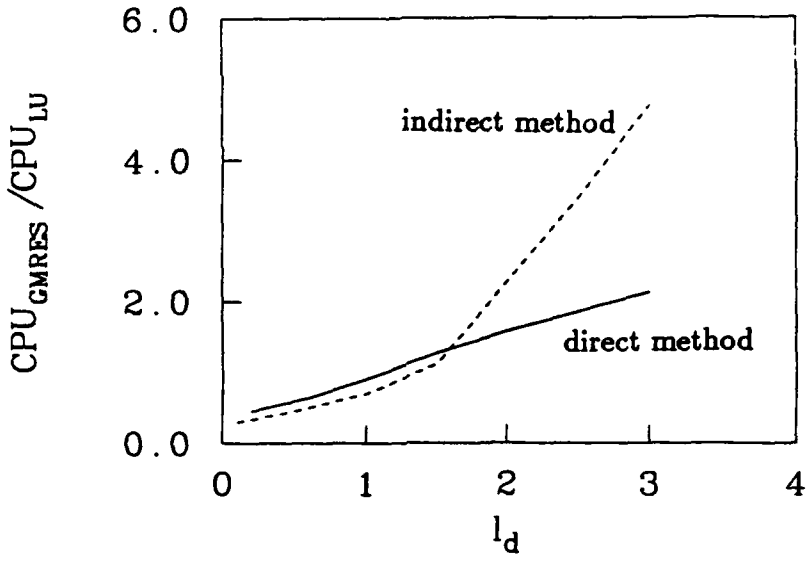


Figure 3.6: Effect of desingularization on computation time
($R_\infty = 6.6667$, $N = 231$)

analytic integration).

For the indirect method with the same truncation, the CPU time for the matrix set up is only about 1.3 seconds, and the CPU time for the solution of the matrix equation by the GMRES varies from 1.7 to 4.0 seconds. The total CPU time is reduced by about 80 percent using the non-singular indirect method for this truncation compared with the singular direct method. When l_d is small (e.g., < 1.5), a larger ϵ does not result in a significant difference in the RMS error (Fig. 3.7), but the CPU time can be significantly reduced (Fig. 3.8).

Fig. 3.9 shows the effect of the truncation of the infinitive plane. The computational domain is extended by adding uniformly sized meshes. As expected, both the direct and indirect methods converge quadratically with respect to the extent of the computational domain for this problem. Both methods also converge algebraically

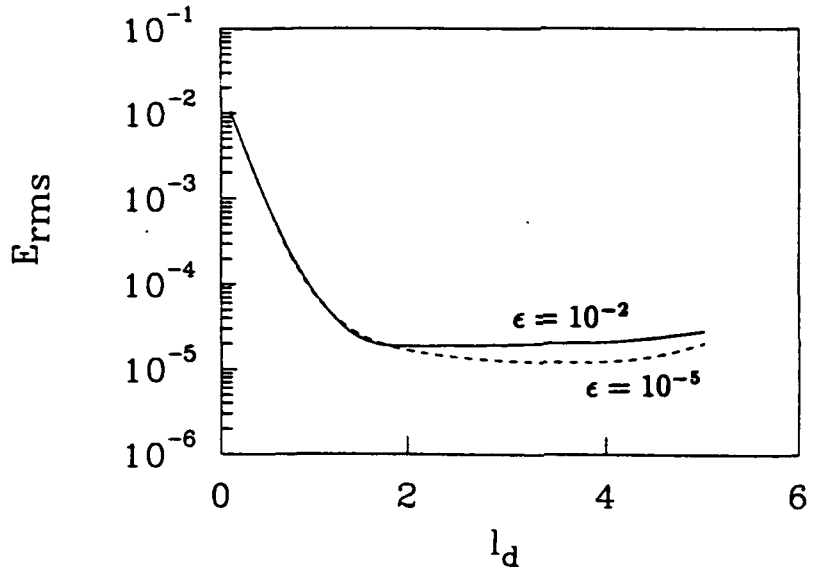


Figure 3.7: Effect of iteration tolerance on RMS error ($R_\infty = 6.6667$, $N = 231$, $l_d = 1$, indirect method)

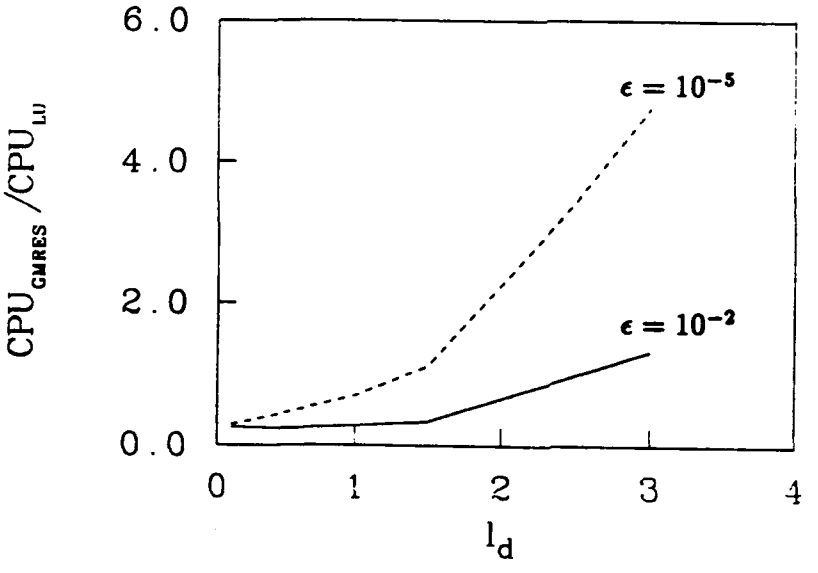


Figure 3.8: Effect of iteration tolerance on computation time ($R_\infty = 6.6667$, $N = 231$, $l_d = 1$, indirect method)

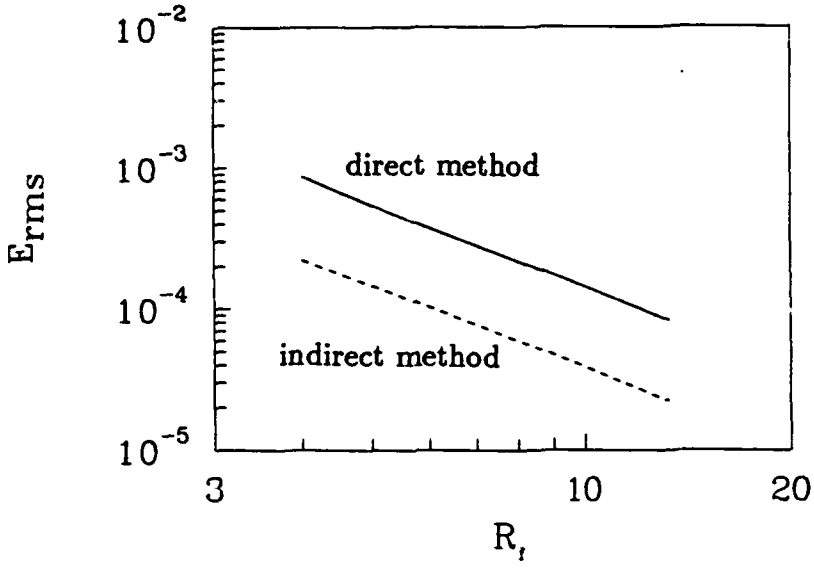


Figure 3.9: Convergence with respect to truncation of boundary ($\Delta X = 0.6667$, $l_d = 1$)

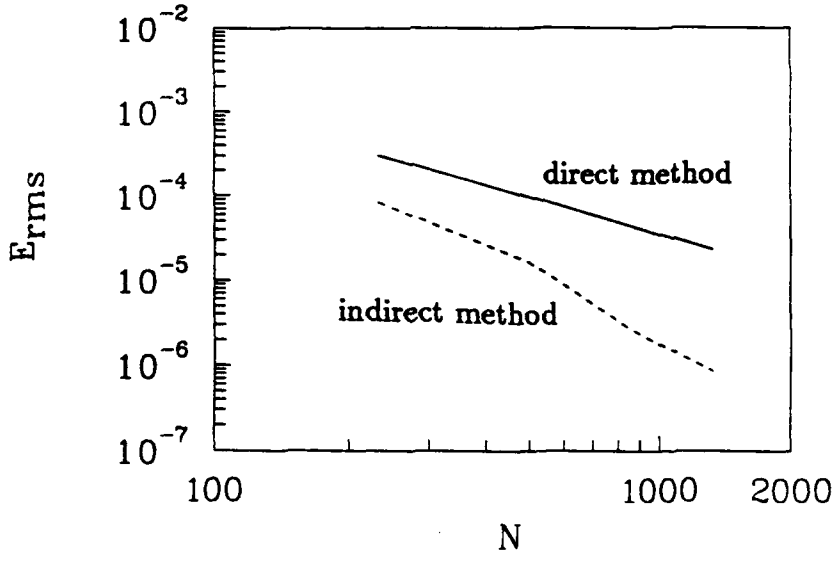


Figure 3.10: Convergence with respect to node number ($R_\infty = 6.667$, $l_d = 1$)

(approximately linearly) with respect to N, Fig. 3.10, in which the computational domain remains unchanged while the mesh size varies.

We also use a surface distribution of sources above the $z = 0$ plane in the indirect method for this problem. This is similar to Webster's method (Webster 1975) except that the integrals over the source surface are carried out by a 2×2 Gaussian quadrature in our case. As seen in Fig. 3.11, the results are better than those using concentrated sources for a large range of l_d (from 0.1 to 3.0). This can be expected since the use of concentrated sources implies using a rougher quadrature for the integrals over the source surface. However, we found that the condition number of the resulting system of equations using a surface distribution of sources is greater than that using concentrated sources by $O(10^2)$ (not shown here). Therefore, the system is no longer well conditioned for l_d greater than 3.0 while the condition of the system using concentrated sources is still acceptable with a double precision computation. In addition, the distributed source requires about as 4 times the CPU time as the concentrated sources in the matrix setup.

Fig. 3.12 shows the error distribution along the x axis for both direct and indirect methods. Larger oscillations in the solution by the direct method are observed at the edge of the computational domain. This may be due to the neglecting of the contribution from the integrals over the far-field closure in the direct method, which is very likely to result in a strong global effect on the accuracy of the boundary integral equation itself. In the indirect method no integrals are required over the real boundary; the boundary condition is enforced within the computational domain, and the singularities individually satisfy the far-field condition. Thus, one may expect that the effect due to the failure in satisfying the boundary condition outside the

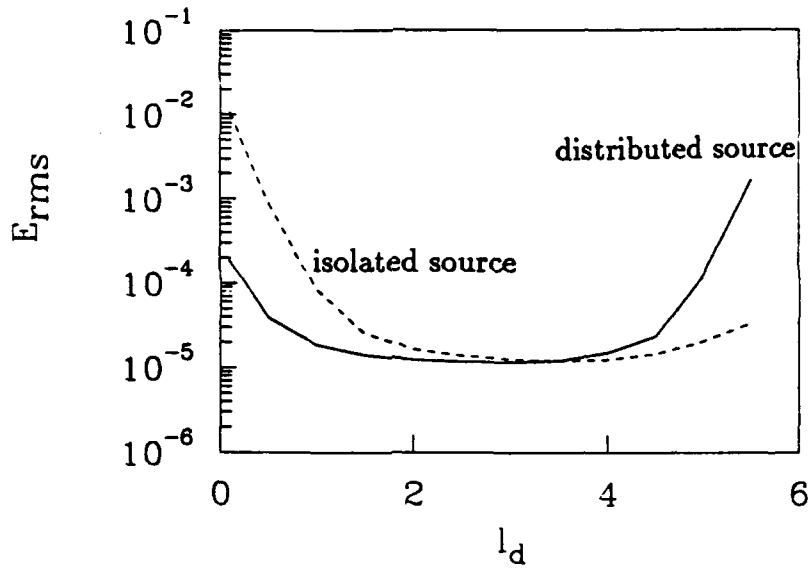


Figure 3.11: Comparison of surface distribution and isolated sources for indirect method ($R_\infty = 6.667$, $N = 231$)

computational domain to be smaller than the effect due to the neglecting of the far-field closure. Overall, we find the indirect method to be better than the direct method for the problems with infinitive boundaries.

3.3.2 Waves due to a source-sink pair moving below the free surface

In this example, the waves are generated by the motion of a submerged source-sink pair below the free surface. The problem is nondimensionalized by making the submergence depth of the source-sink pair, the gravity acceleration and the fluid density unity. The source-sink pair moves in the x direction with the velocity $\vec{U} = F_n(1 - e^{-\mu t})$ starting from rest and gradually increasing to a steady value F_n. The strength of the pair is given by $\sigma(t) = \sigma_o(1 - e^{-\mu t})$ which also increases from zero to the final value σ_o gradually. The distance between the source and sink is set equal to 0.1. The Froude number is unity. The midpoint between the pair is initially

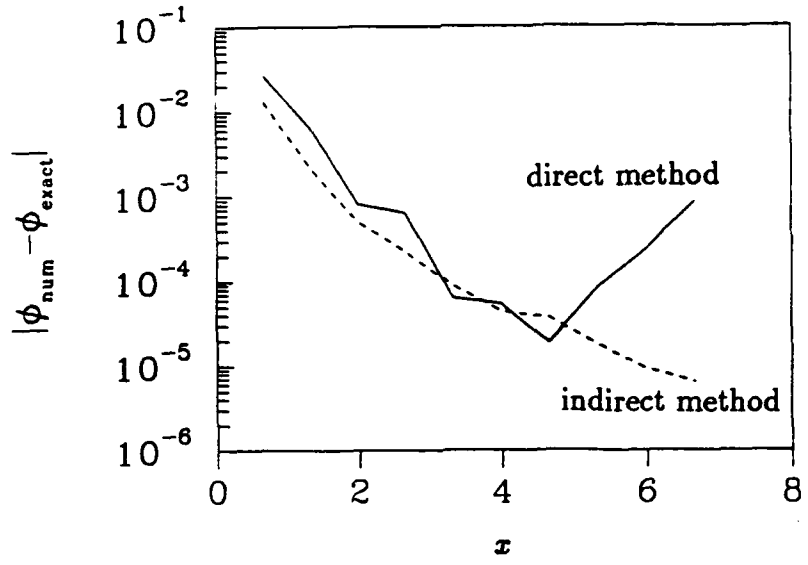


Figure 3.12: Error distribution along x-axis ($R_\infty = 6.6667$, $N = 231$, $l_d = 1$) located at point $(5, 0, -1)$.

We use the indirect method with concentrated sources because of its computational advantages and simplicity. An additional advantage of the indirect method is that the velocities can be calculated directly once the strength of the singularity distribution is known, while the direct method requires numerical differentiation to obtain the tangential components of the velocity. The potential is expressed as a sum of 1) the potential due to the submerged source-sink pair in a infinitive fluid, 2) the image of the submerged pair above the undisturbed free surface, and 3) a sum of N concentrated sources of unknown strength above the free surface. The far-field condition is better satisfied when the image of the pair is used in the construction of the solution. The discretized integral equation for the unknowns σ_i is

$$\sum_{i=1}^{N} \frac{\sigma_i}{|\vec{X}_f - \vec{X}_{si}|} = \phi_o(\vec{X}_f)$$

$$-\frac{-\sigma(t)}{\left|\vec{X}_f - \vec{X}_{source}\right|} - \frac{\sigma(t)}{\left|\vec{X}_f - \vec{X}_{sink}\right|} - \frac{-\sigma(t)}{\left|\vec{X} - \vec{X}^i_{source}\right|} - \frac{\sigma(t)}{\left|\vec{X} - \vec{X}^i_{sink}\right|}, \tag{3.21}$$

where $\phi_o(\vec{X}_f)$ is known from previous time. $\vec{X}_{source}$ and $\vec{X}_{sink}$ are the locations of the source and sink and $\vec{X}^i_{source}$ and $\vec{X}^i_{sink}$ are the locations of their images. After the σ_i are solved, the velocities of the fluid particles on the free surface can be calculated A fourth-order Runge-Kutta-Fehlberg method is used in the nonlinear free surface integration.

In the results shown below, the initial free surface mesh grid extends from $0 \leq x \leq 20$ and $0 \leq y \leq 7.5$ and has 41×16 node points. The grid spacing is uniform in the x direction but increases by 10% in the y direction. The node points serve as the material points. The concentrated sources are placed approximately perpendicular from the node points at a distance determined by (3.13) with $l_d = 1.0$ and $\nu = 0.5$.

The method is first applied to waves generated by a sufficiently small disturbance such that linear wave theory is a good approximation. The results of the present method using fully nonlinear free surface conditions are compared to an "exact" solution computed from a time-dependent Green function for a Kelvin wave source that satisfies the linearized free surface condition (King, Beck & Magee, 1988). Fig. 3.13 shows the comparison of the nonlinear wave elevation along the symmetry plane to the linear wave elevation at $t = 10$ for a weak disturbance ($\sigma_o = 0.05$). The nonlinear and linear results agree very well. Independent computations using: a) a smaller computational domain (with the same mesh spacing within $0 \leq x \leq 15$ and $0 \leq y \leq 7.5$), b) finer mesh grids (81×16 and 41×31 with the same computational domain size), and c) doubling the time increment, result in negligible difference for the nonlinear calculation. This indicates that even for the small disturbance example studied here, the differences in Fig. 3.13 are primarily due to nonlinear effects. Fig. 3.14 shows

the results for a stronger disturbance ($\sigma_o = 0.75$), showing the significant nonlinear effects of the free surface conditions, especially at the trough.

To study the effects (mainly the non-physical reflection) due to the truncation of the free surface, we compare the results using two differently sized computational domains mentioned above with identical grid spacing for the weak disturbance case. Fig. 3.15 shows the results using the two domains. Little difference is seen in the results of the two computations until the front wave hits the boundary of the smaller domain. Even after the front wave passes this boundary, significant differences are not apparent until the first crest passes the boundary. The error then starts to grow and propagate back into the domain. This differs from our attempts to solve the identical problem using the direct method—extraneous wave reflections were noticed at the boundary almost immediately. This is remarkable, especially considering that the non-singular indirect method requires no special treatment such as one-side derivatives along the edge of the computational domain. While in the direct method, numerical spatial derivatives, especially one-side derivatives at the boundary are necessary to calculate the velocities of the nodes. It is known that numerical differentiation is very likely to cause numerical instabilities.

3.4 Conclusions

The non-singular formulation significantly reduces the time required to compute the influence matrix of the resulting algebraic system. The algebraic systems are still adequately well-conditioned to allow efficient iterative solutions. Accurate solutions can be obtained by the desingularized boundary method for a large range of desingularization distances on the order of the mesh size (near $l_d = 1$). The indirect method is more efficient than the direct method. It is easy to code and takes less

computation time. In addition, the indirect method performs better for problems with infinitive boundaries and handles irregular meshes more easily. Nonlinear wave calculations using the time-stepping procedure with desingularized boundary integral method show promising. The method will be examined in the studies on more complicate nonlinear wave problems in the following chapters.

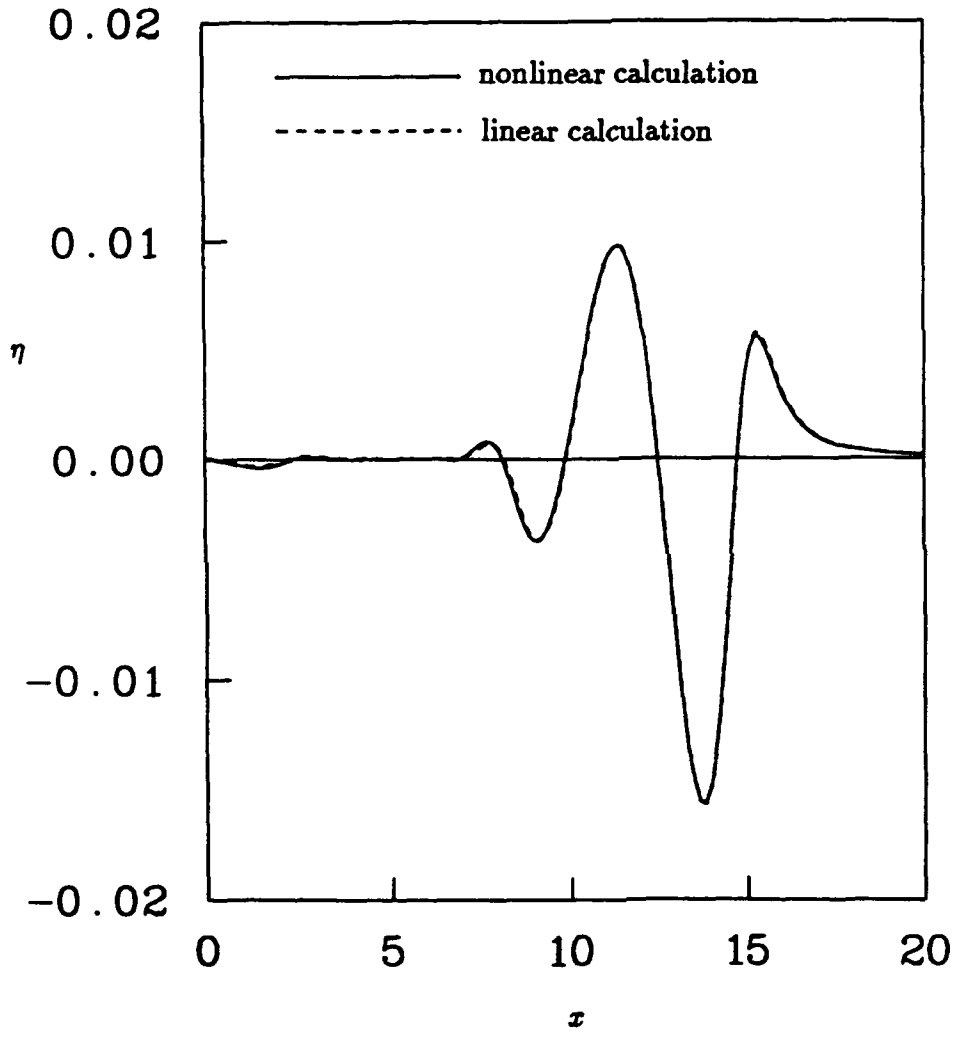


Figure 3.13: Waves along x-axis ($t = 10$, $\sigma_o = 0.05$, $F_n = 1$)

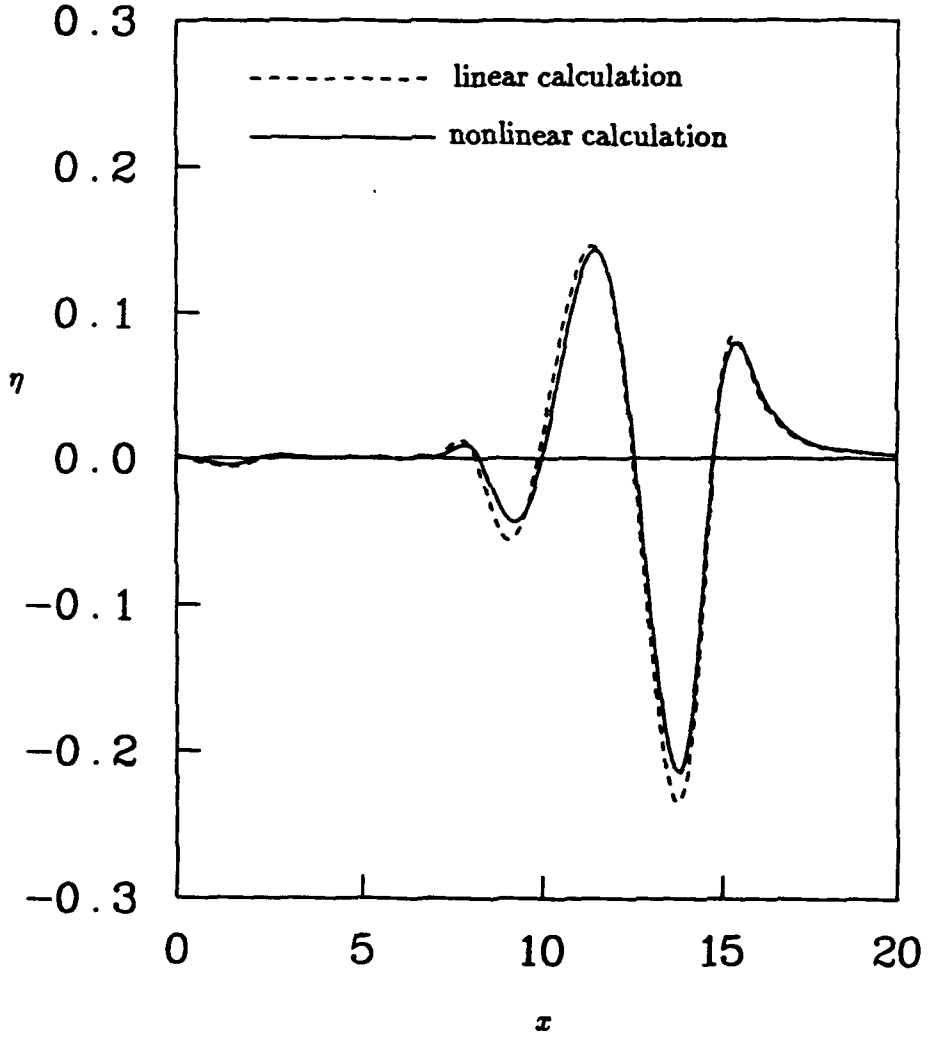


Figure 3.14: Waves along x-axis ($t = 10$, $\sigma_o = 0.75$, $F_n = 1$)

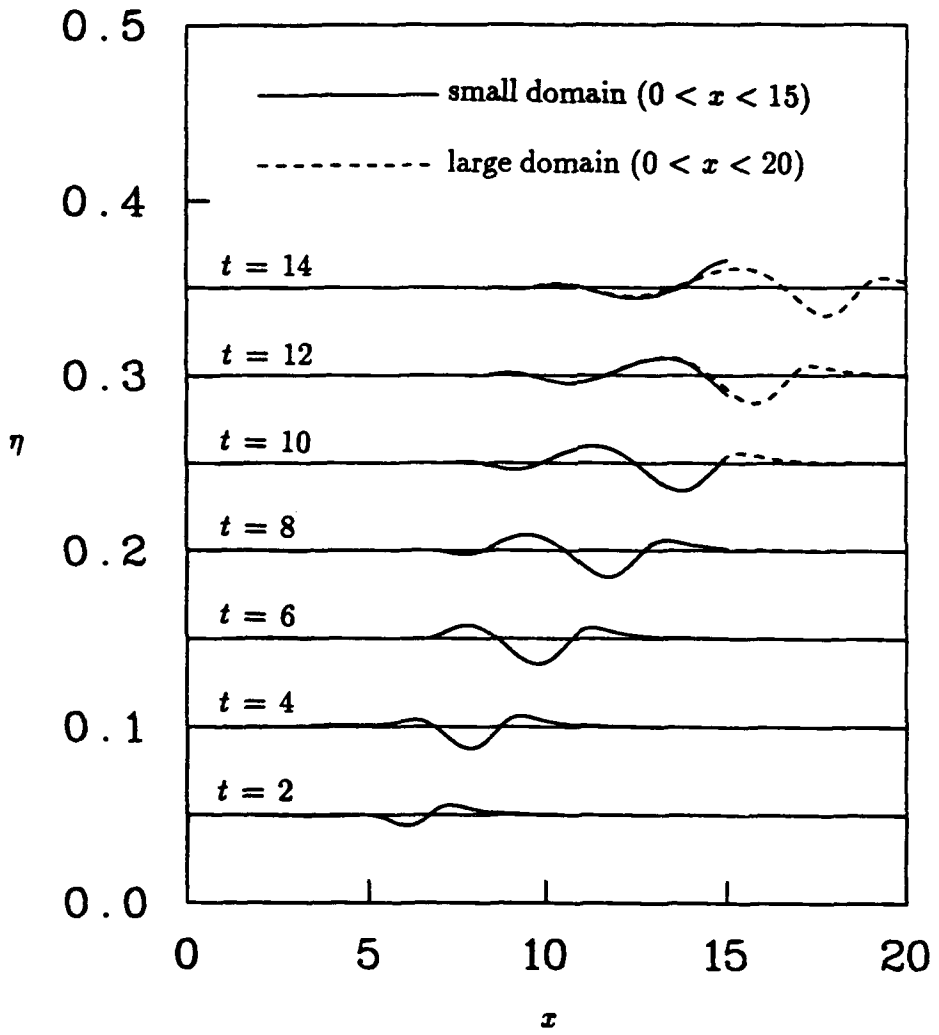


Figure 3.15: Effect of computational domain size on wave elevation along x-axis ($\sigma_o = 0.05$, $F_n = 1$)

CHAPTER IV

TWO-DIMENSIONAL SOLITONS IN A SHALLOW WATER

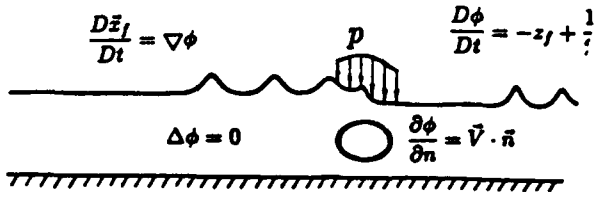
A disturbance moving steadily with a transcritical velocity in a shallow water can generate a succession of solitary waves, advancing upstream of the disturbance. A train of weakly nonlinear and weakly dispersive waves develops downstream of a region of depressed water surface trailing just behind the disturbance. Although the disturbance is steady (moving at a constant speed), the flow generated is never steady because the flow is in resonance when the disturbance moves near the critical speed. This phenomenon was first found by Wu & Wu (1982) using a generalized Boussinesq model for two-dimensional long waves generated by a moving surface pressure or bottom topography distribution. This phenomenon was later experimentally confirmed by Ertekin, Webster & Wehausen (1986) and Lee, Yates & Wu (1989). It has been found that it is important to include the nonlinear term in the free surface boundary conditions in order to get the solitary waves.

The generalized Boussinesq model is only good for long waves (*i.e.* $\epsilon = h_o/\lambda$ is small, where h_o is the mean depth of the water and λ is a typical wave length). A high-order equation is given in Dommermuth & Yue (1987) for the problem. For a weak disturbance near the critical speed, a simplified forced KdV equation (fKdV), derived

from the Boussinesq equation, can be used to model the phenomenon (Akylas 1984, Cole 1985, Wu 1987, and Lee *et al.* 1989). Attempts have been made to extend the formulations to three-dimensional waves with side walls (Mei 1986, Katsis & Akylas 1987, Ertekin *et al.* 1986, and Pederson 1988).

Most theoretical studies on this phenomenon are based on perturbation methods. Recently, Choi, *et al.* (1990) used a finite element method based on Luke's variational principle for the generation of solitons by a ship moving in a channel. Grilli & Svendsen (1989) used the mixed Eulerian-Lagrangian time stepping formulation with a boundary integral equation technique (singular formulation) for a related problem studying the runup and reflection of a two-dimensional solitary wave in a numerical tank. In their method, Grilli & Svendsen solve the Laplace equation numerically with the fully nonlinear free surface boundary conditions. These numerical methods have broader applications than the perturbation methods.

In this chapter, the waves generated by a free surface pressure or a bottom topography moving at the critical speed are studied using both the fKdV model (Wu, 1987) and the fully nonlinear model with the desingularized method. The results from the two different models are compared. The difference in the waves due to the free surface pressure and the bottom topography with an identical dimensionless distribution is studied by the fully nonlinear model. In the fKdV model, these two different disturbances will generate the same waves (Wu 1987). We will also study the nonlinear waves due to submerged bodies, which are difficult for the perturbation methods mentioned above to consider. The bottom is horizontally flat except in the area of the varying bottom topography. The free surface extends to infinity at both ends, Fig. 4.1. The flow is assumed irrotational. The problem is nondimensionlized



Initial Conditions

$$\phi = 0 \quad (t \leq 0)$$

$$z_f = -p \quad (t \leq 0$$

Figure 4.1: Problem definition for solitons in shallow water

by the mean water depth h_o, the gravity acceleration g and the fluid density ρ.

4.1 fKdV Equation

The fKdV equation for a free surface pressure and a bottom topography distribution can be derived from the Boussinesq equations (Wu 1987) and has the form

$$\eta_t - (1 + \frac{3}{2}\eta)\eta_x - \frac{1}{6}\eta_{xxx} = \frac{1}{2}(p_a + b)_x = \frac{1}{2}P_x, \tag{4.1}$$

where $p_a = p_a(x + F_n t)$ and $b = b(x + F_n t)$ represent a free surface pressure and a bottom topography moving in $-x$ direction, respectively, and F_n is the Froude number based on the mean water depth. Given the forcing $P(x + F_n t) = p_a(x +$

$F_n t) + b(x + F_n t)$ associated with the initial conditions, Eq. (4.1) can be solved for the wave elevation η. Detail of the derivation can be found in Wu (1987).

Within the fKdV model, the free surface pressure and the bottom topography disturbance play the same forcing role, *i.e.* the waves generated by a pressure disturbance will be the same as the waves due to a topography disturbance if the two disturbances have the same distribution and magnitude. This implies that in an experiment, a free surface pressure distribution can be replaced by the equivalent topography bottom that is easier to control (Lee *et al.* 1989). However, they are not interchangeable if the parameter ranges are beyond the fKdV assumptions.

No closed form solution to (4.1) has been found. A numerical approach is necessary. For the concern of numerical stability in solving the fKdV equation, it is preferable to replace the dispersion term η_{xxx} in (4.1) by η_{xxt} based on the lowest order solution. Thus (4.1) becomes,

$$\eta_t - (1 + \frac{3}{2}\eta)\eta_x - \frac{1}{6}\eta_{xxt} = \frac{1}{2}P_x. \tag{4.2}$$

This was first pointed out by Benjamin *et al.* (1972) and later used by Wu (1987) and Lee *et al.* (1989)

Following Wu (1987), we solve the fKdV equation (4.2) numerically with a time-stepping procedure based on the Euler's predictor-corrector algorithm to advance time without iteration at the correction stage. A second-order central-difference approximation is used for the spatial derivatives. Since this is an implicit method, both the prediction and correction stages reduce to the inversion of a constant tridiagonal matrix, which is strictly diagonally dominant.

A computational window moving with the disturbance is employed. The time

step Δt and the shifted distance Δx (usually the mesh size) are chosen such that

$$J = \frac{\Delta x}{F_n \Delta t} \tag{4.3}$$

is an integer ($J = 1, 2, 3, ...$). Thus the window is shifted every J time steps and if we view the solution only when the window is shifted, the position of the disturbance in the window does not change. Each time the window is shifted one point is dropped at the downstream side of the window and a new point emerges into the window from upstream. Because of the finite computational domain, a treatment for the open boundary conditions is necessary to reduce non-physical reflections from the the boundaries. Wu & Wu (1982), Wu (1987) and Lee *et al.* (1989) use

$$\eta_t = \pm \eta_x \tag{4.4}$$

where the "+" is taken for the upstream while "−" for the downstream. Although this open boundary condition is only appropriate for linear waves with unit phase speed, it has been shown that it can eliminate most of the non-physical small amplitude wave reflection from open boundaries. The open boundary condition (4.4) is discretized by a forward difference in time. For the spatial discretization, a backward difference is used for the upstream point and a forward difference for the downstream point. Even though the open boundary condition (4.4) is used, the value of η for the new coming point upstream still needs to be provided. It is not clearly stated how the value of η for the coming point is provided in the above mentioned papers. We provide the value by quadratic extrapolation using the three closest points.

4.2 Fully Nonlinear Model

We apply the indirect desingularized method to this problem. A submerged moving body can also be considered in this method. At each time instant, the

potential is constructed as,

$$\phi(x,y) = \sum_{j=1}^{N^f} \sigma_j{}^f \Phi^f(x,y,x_j{}^f,y_j{}^f) + \sum_{k=1}^{N^h} \sigma_k{}^h \Phi^h(x,y,x_k{}^h,y_k{}^h), \tag{4.5}$$

where (x,y) is the field point. Φ^f is the potential due to the source at point $(x_j{}^f, y_j{}^f)$ above the free surface and its image source about the $z = -1$ plane, and Φ^h the potential due to the source at point $(x_k{}^h, y_k{}^h)$ inside the rigid surface and its image,

$$\Phi^f = \log[(x-x_j{}^f)^2 + (y-y_j{}^f)^2] + \log[(x-x_j{}^f)^2 + (y-y_j{}^f+2)^2], \tag{4.6}$$

$$\Phi^h = \log[(x-x_k{}^h)^2 + (y-y_k{}^h)^2] + \log[(x-x_k{}^h)^2 + (y-y_k{}^h+2)^2]. \tag{4.7}$$

The function $\phi(x,y)$ automatically satisfies the Laplace equation and the boundary condition on the bottom except the area of a bottom topography. The Dirichlet condition on the free surface and the Neumann condition on other rigid body surfaces remain to be satisfied. The source strength $\sigma_j{}^f$ and $\sigma_k{}^h$ are determined by satisfying the boundary conditions at the chosen control points on the free surface and rigid surface,

$$\sum_{j=1}^{N^f} \sigma_j{}^f \Phi^f(\bar{x}_i,\bar{y}_i,x_j{}^f,y_j{}^f) + \sum_{k=1}^{N^h} \sigma^h{}_k \Phi^h(\bar{x}_i,\bar{y}_i,x_k{}^h,y_k{}^h) = \phi_o(\bar{x}_i,\bar{y}_i)$$

$$(i = 1,2,...,N^f), \tag{4.8}$$

$$\sum_{j=1}^{N^f} \sigma^f{}_j \frac{\partial}{\partial x} \Phi^f(\hat{x}_l,\hat{y}_l,x_j{}^f,y_j{}^f) + \sum_{k=1}^{N^h} \sigma^h{}_k \frac{\partial}{\partial x} \Phi^h(\hat{x}_l,\hat{y}_l,x_k{}^h,y_k{}^h) = \vec{V}_h \cdot \vec{n}(\hat{x}_l,\hat{y}_l)$$

$$(l = 1,2,...,N^h), \tag{4.9}$$

where $(\bar{x}_i,\bar{y}_i)$ is the control point on the free surface and $(\hat{x}_l,\hat{y}_l)$ is the control point on the rigid surface. ϕ_o is known from the previous time. Equations (4.8) and (4.9) form a system of $(N^f + N^h) \times (N^f + N^h)$ linear equations. After solving (4.8) and (4.9) for $\sigma_j{}^f$ and $\sigma_k{}^h$, the flow is determined and the flow velocities can be calculated by taking the spatial derivative of (4.5). The free surface position and the flow potential

on it can then be updated. The pressure on the body can also be calculated using (2.16) and integrating the pressure gives the forces on the body.

The fourth-order Runge-Kutta-Fehlberg method and the same computational window shifting technique for the fKdV equation is used in the time stepping. Each time the window is shifted one node point is dropped at the downstream side of the window without any treatment since no spatial derivative of the free surface is required in this algorithm. For the upstream boundary, the position and the potential of the incoming point are pre-computed using some extra upstream points outside the window, which are convected by the computed velocity from the already solved source strength. The extra points do not contribute to the discretized integral equation.

4.3 Numerical Results

For the fully nonlinear method, the effects of the mesh size, the error telorance for the GMRES and the error tolerance for the Runge-Kutta-Fehlberg subroutine on the solution have been numerically tested. It has been found that as long as the GMRES error tolerance is less than $10^{-8}(N^l + N^h)$, the Runge-Kutta-Fehlberg error telorance less than 10^{-3}, and if the mesh has at least 15 nodes per wave length, the solution will be adequately resolved.

4.3.1 Solitons due to a free surface pressure

The waves generated by a moving surface pressure distribution are studied. The pressure distribution (Wu 1987) is used,

$$P(x+F_nt) = p_a(x+F_nt) = \begin{cases} \frac{1}{2}P_m\{1+\cos[\frac{2\pi}{L}(x+F_nt)]\} & |x+F_nt| \le \frac{L}{2} \\ 0 & |x+F_nt| \ge \frac{L}{2} \end{cases}$$

This will also check our programs for the fKdV model and the fully nonlinear model.

First the results by the fKdV and the fully nonlinear algorithm for a relatively weak forcing ($P_m = 0.02$) are compared. The results using 301 node points and a time step $\Delta t = 0.2$ in the two models are shown in Fig. 4.2. No upstream runaway soliton is observed since the disturbance is weak and the period for the generation of the solitons is very large. In general, the results of the two methods are similar although the transient trailing waves computed by the fKdV program seem to travel faster downstream away from the disturbance than those by the nonlinear program and the nonlinear program predicts a steeper front wave. Both methods have small non-physical downstream reflections of about the same magnitude after the waves reach the downstream boundary. The results change little with finer grids. It is difficult to isolate the causes of the differences in the results by the fKdV and the nonlinear computation. They may be due to the computational errors or to the different mathematical models. It seems that the difference is mainly due to the different models for both the free surface nonlinearity and the two-dimensional effect. This can be seen by examining the short time results where the trailing waves have not reached the downstream boundary and the solutions are not affected by the non-physical reflection.

For stronger forcing, $P_m = 0.1$, both models predict the upstream runaway soli-

tons shown in Fig. 4.3. The results are in good agreement in general. However, the nonlinear model again predicts steeper waves with a shorter period to generate solitons. This becomes more obvious when the forcing is stronger. Fig. 4.4 shows the results for $P_m = 0.15$. As seen, the nonlinear model predicts a much steeper front wave which starts to break at $t = 24.2$ and the program stops. For $P_m = 0.2$, which is used in Wu (1987) and Lee *et al.* (1989), the waves by the nonlinear program break sooner (not shown here), while the waves by the fKdV model do not break. This does not necessarily indicate that the fKdV model gives a better solution. As assumed for the derivation of the fKdV equation (Wu 1987), the forcing P_m must be $O(\epsilon^4)$. A typical wavelength can be estimated for the case $P_m = 0.1$ shown in Fig.4.3 from the figure. The wavelength λ is found approximately 10. Therefore, $\epsilon is approximately 0.1$. So the forcing P_m should be $O(10^{-4})$. The values for P_m used in Wu (1987) seem far beyond this limitation. Wave breaking was observed in the experiments (Lee *et al.* 1989).

Fig. 4.5 shows the results for a surface pressure at the supercritical speed ($F_n = 1.5$). Both models reveal the similar characters of the flow motion. The downstream transient waves travel at slower speeds than the disturbance and eventually only a single steady soliton remains traveling at the same speed as the forcing. Also, since the flow is not in resonance, the soliton height is smaller than those generated by the disturbances near the critical speed.

4.3.2 Comparison of free surface pressure and bottom topography

In the fKdV model, the waves due to a pressure disturbance are the same as the waves due to a topography disturbance if their dimensionless distributions are

identical. This is due to the fact that the fKdV model assumes small ϵ and uses the vertical average of the flow velocity over the water layer, thus not taking into account the two-dimensional effects of the vertical variation. The differences in the waves generated by the free surface pressure and the bottom topography of identical distribution using the fully nonlinear model are examined.

Fig. 4.6 shows the waves due to a moving semi-elliptical bottom topography with the major axis L and minor axis b_o being 2.0 and 0.2, respectively. Fig. 4.7 shows the waves generated by the free surface pressure of the same dimensionless elliptical distribution. The difference in the waves due to the two different disturbances are very significant. The free surface pressure behaves as a stronger forcing than the bottom topography. The waves due to the pressure start to break at about $t = 55$. The breaking occurs at the first wave peak downstream of the disturbance.

4.3.3 Solitons due to submerged cylinders

Waves generated by submerged cylinders, which cannot be modeled by the fKdV equation but can be easily handled by the nonlinear model, are calculated. Fig. 4.8 shows the waves due to a circular cylinder with the radius $R = 0.15$ and the depth of the centroid $h_c = 0.6$ moving at $F_n = 1.0$. Solitons generated are clearly seen. Fig. 4.9 shows the waves generated by a larger circular cylinder with $R = 0.2$ at the same speed. The the cylinder with larger radius implies a stronger disturbance and therefore produces larger waves and the first wave downstream starts to break at about $t = 45$. Fig. 4.10 shows the waves due to the cylinder ($R = 0.15$) at the supercritical speed ($F_n = 1.5$). Again only one single soliton eventually moves with the disturbance as in the case of the surface pressure (Fig. 4.5). Fig. 4.11 and

Fig. 4.12 show the waves due to elliptical cylinders. In the former case, the ratio of the major axis to the minor axis is $R_y/R_x = 0.075/1.0$. In the later case, the cylinder has a larger minor axis ($R_y/R_x = 0.1/1.0$) representing a stronger disturbance. The breaking of the downstream wave occurs in the later case.

4.4 Conclusions

The fully nonlinear model predicts the runaway solitons for three types of disturbances moving near the critical speed: surface pressure, bottom topography and submerged cylinder. The numerical results by the fully nonlinear model agree with the fKdV results for the weak surface pressure disturbance. For the strong disturbance, the fully nonlinear model predicts larger solitons than the fKdV. These solitons are so steep that they break either upstream or downstream. According to the fully nonlinear calculations, for an identical distribution, the free surface pressure generates larger waves than the bottom topography and the difference is significant.

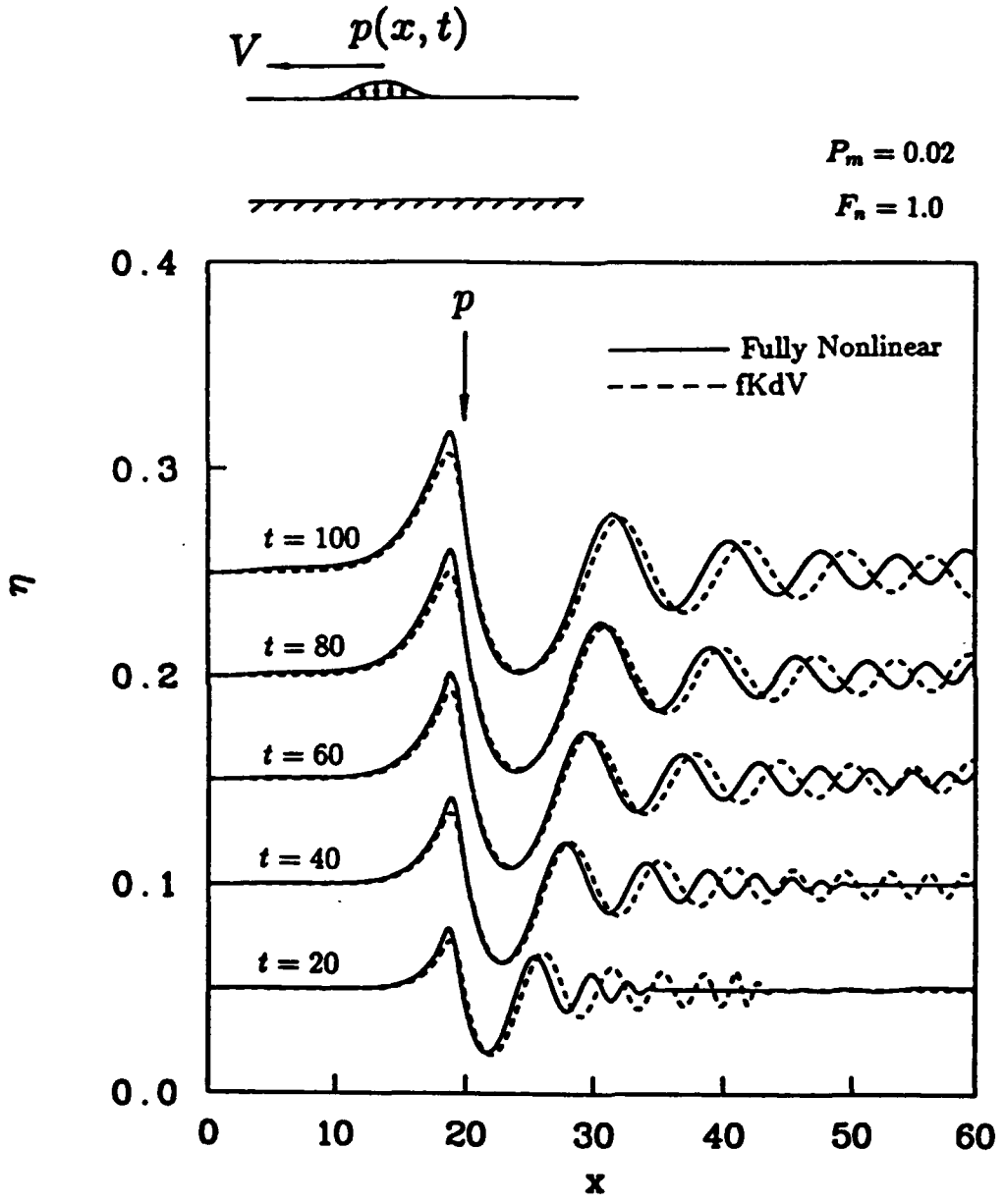


Figure 4.2: Waves due to free surface pressure ($P_m = 0.02$, $F_n = 1.0$, $\Delta t = 0.2$)

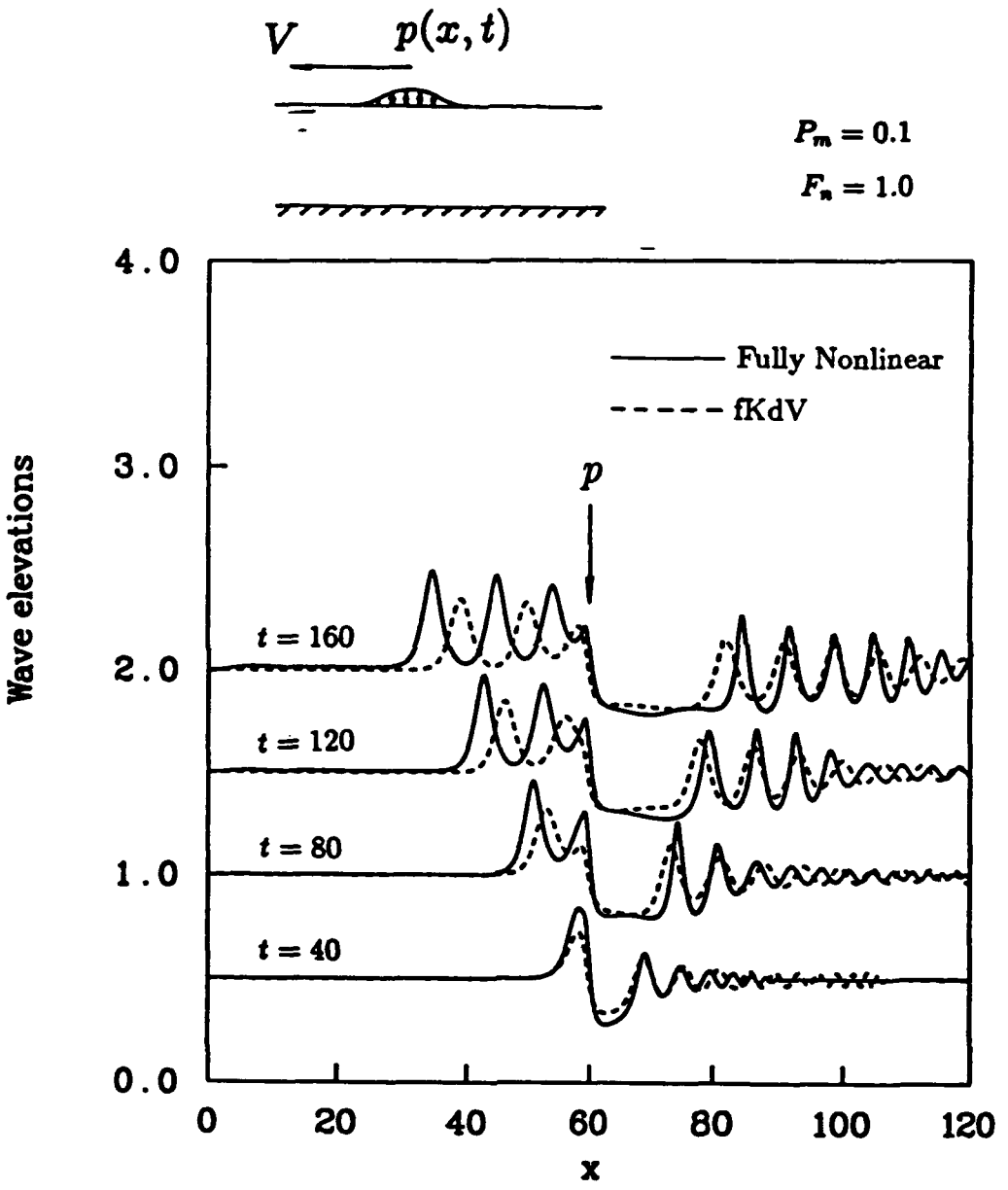


Figure 4.3: Waves due to free surface pressure ($P_m = 0.1$, $F_n = 1.0$, $\Delta t = 0.2$)

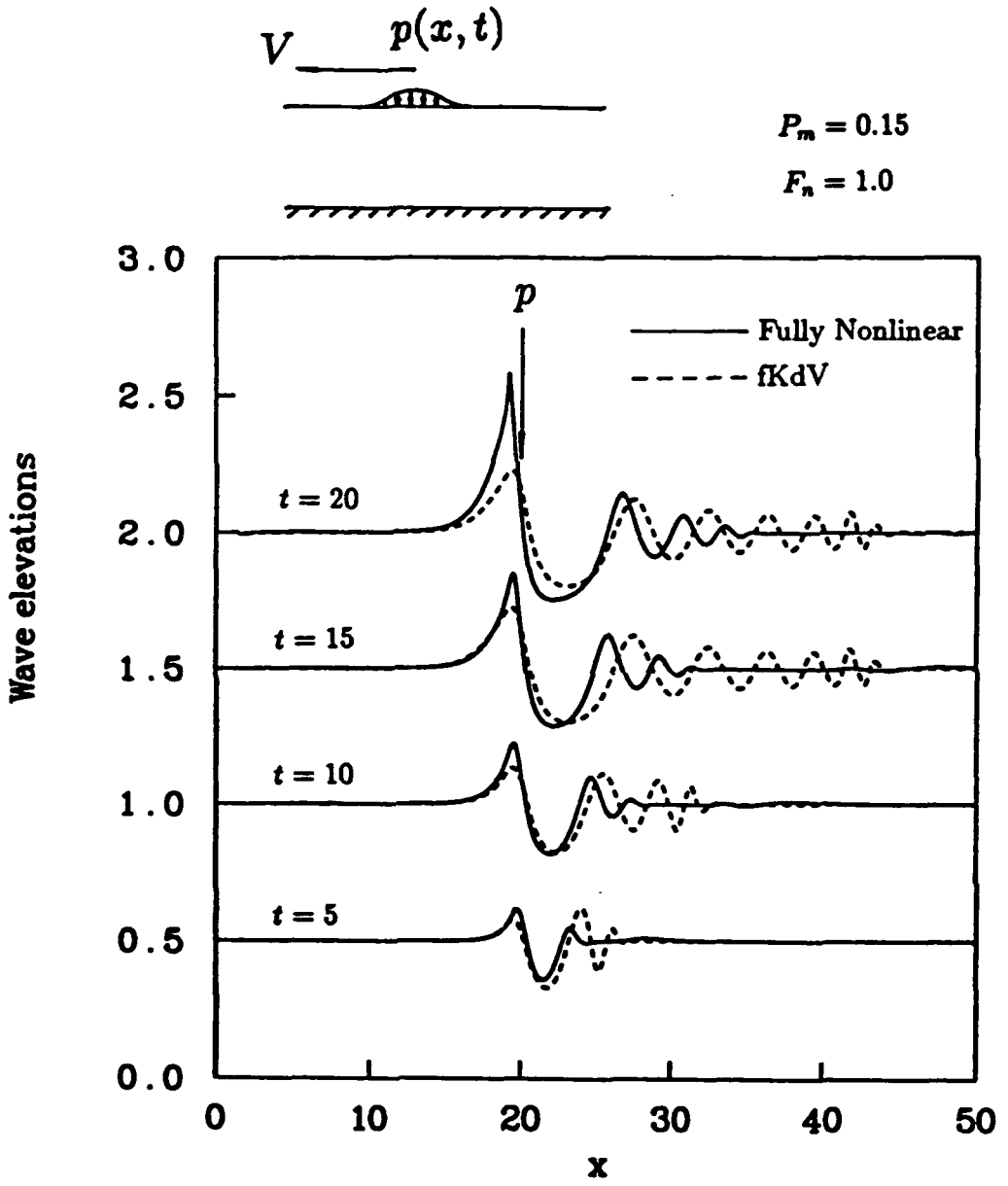


Figure 4.4: Waves due to free surface pressure ($P_m = 0.15$, $F_n = 1.0$, $\Delta t = 0.2$)

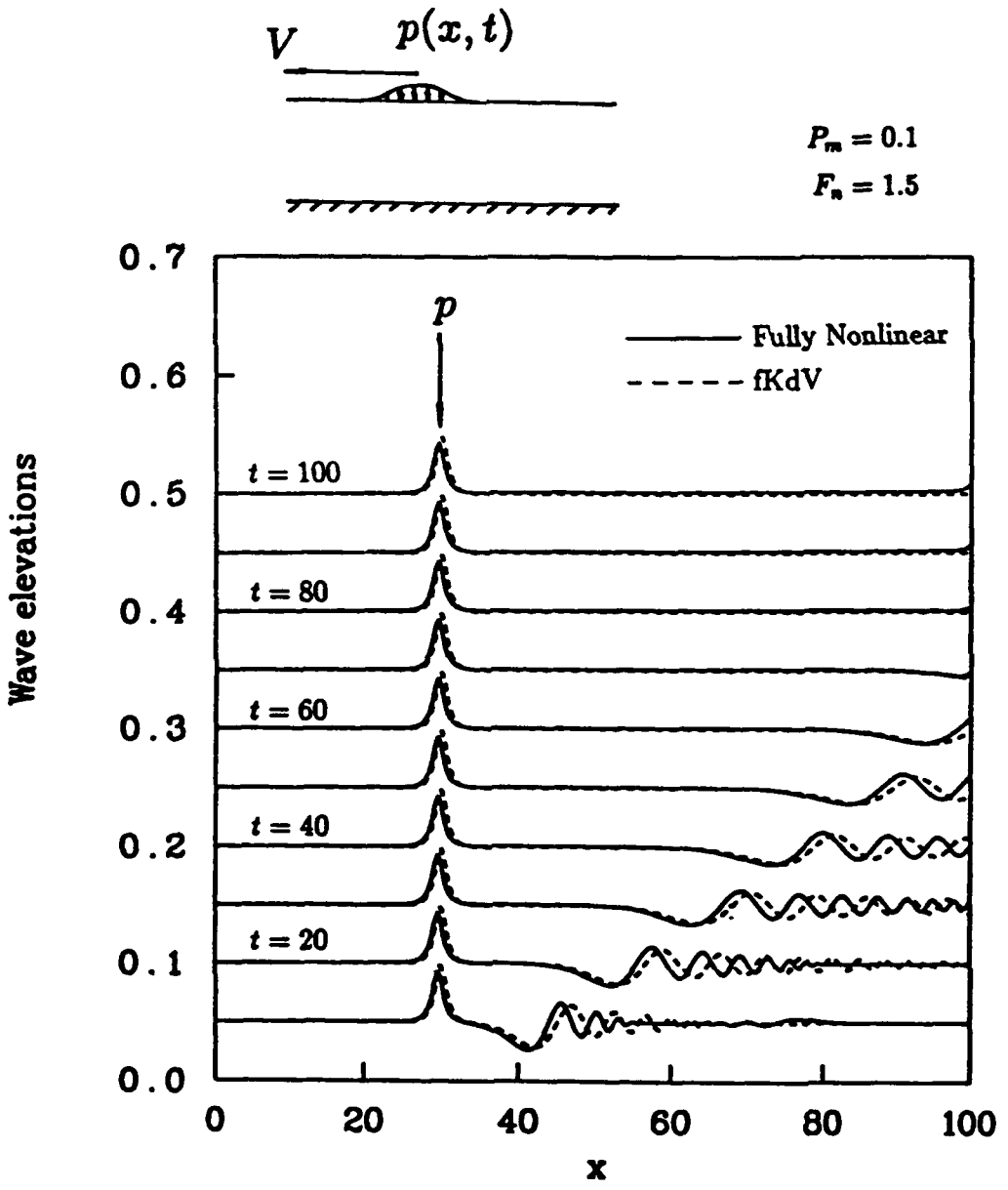


Figure 4.5: Waves due to free surface pressure ($P_m = 0.1$, $F_n = 1.5$, $\Delta t = 0.2$)

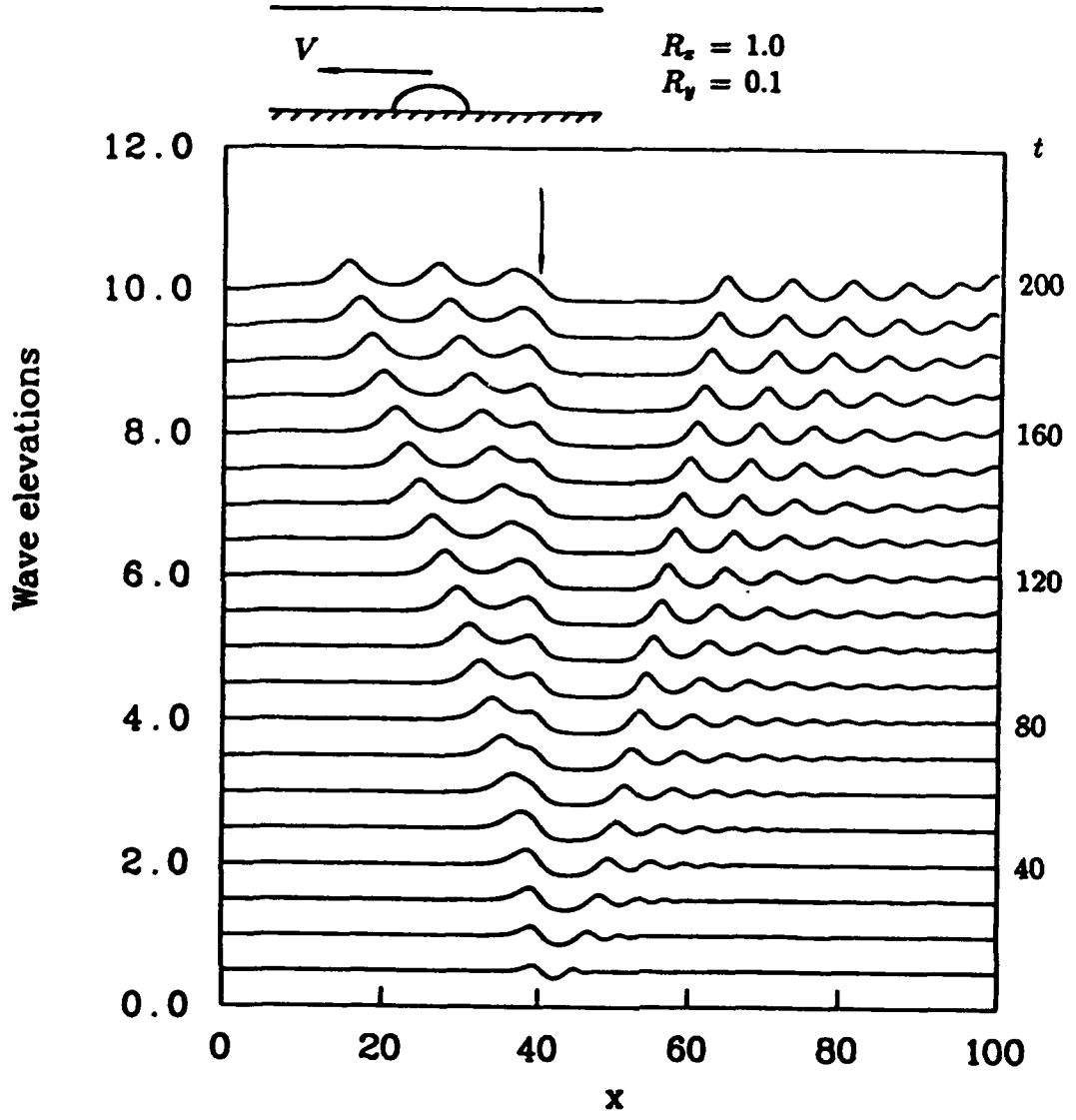


Figure 4.6: Waves due to bottom topography ($L = 2.0$, $2P_m = 0.2$, $F_n = 1.0$, $\Delta t = 0.2$)

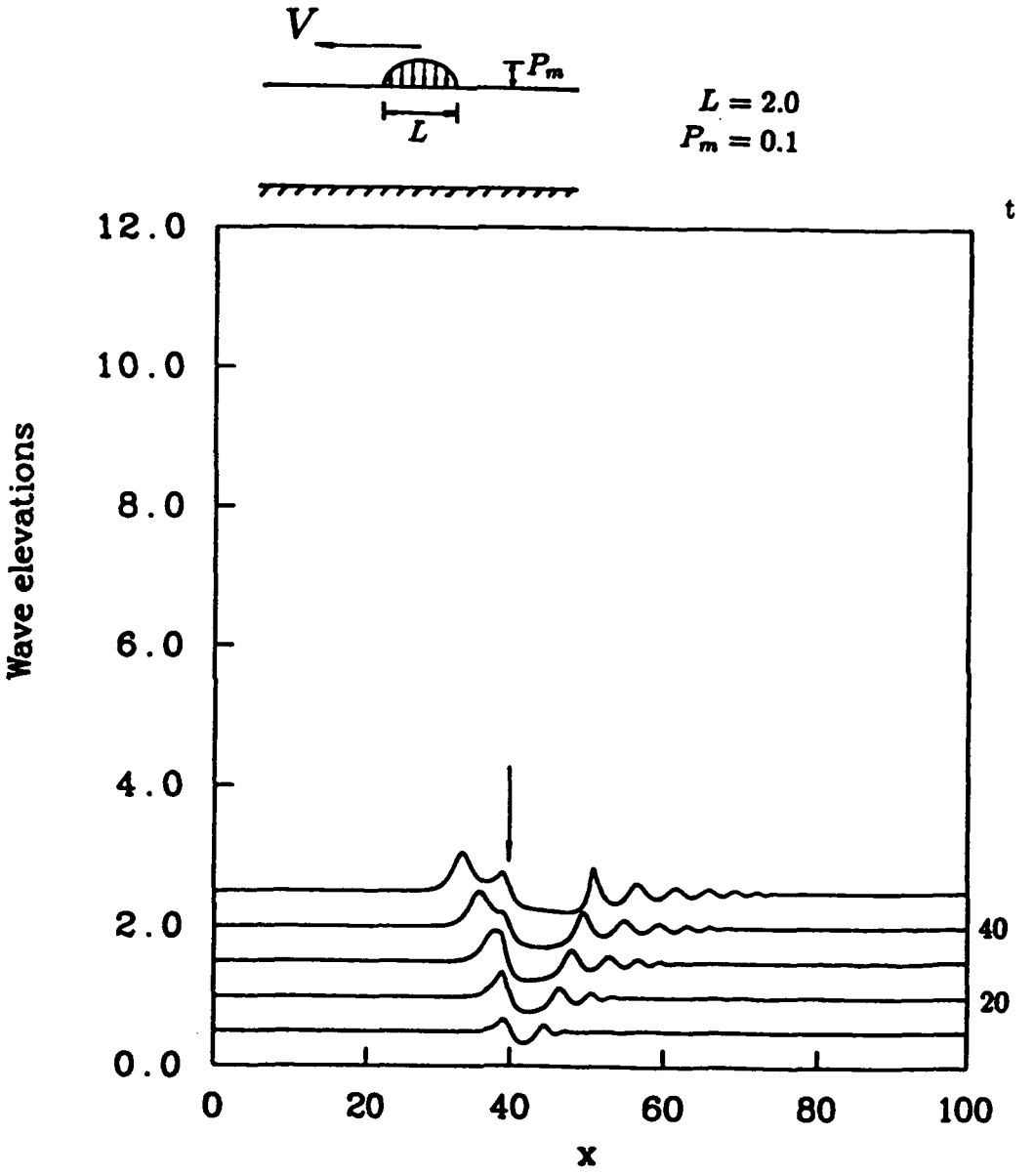


Figure 4.7: Waves due to free surface pressure ($L = 2.0$, $2P_m = 0.2$, $F_n = 1.0$, $\Delta t = 0.2$)

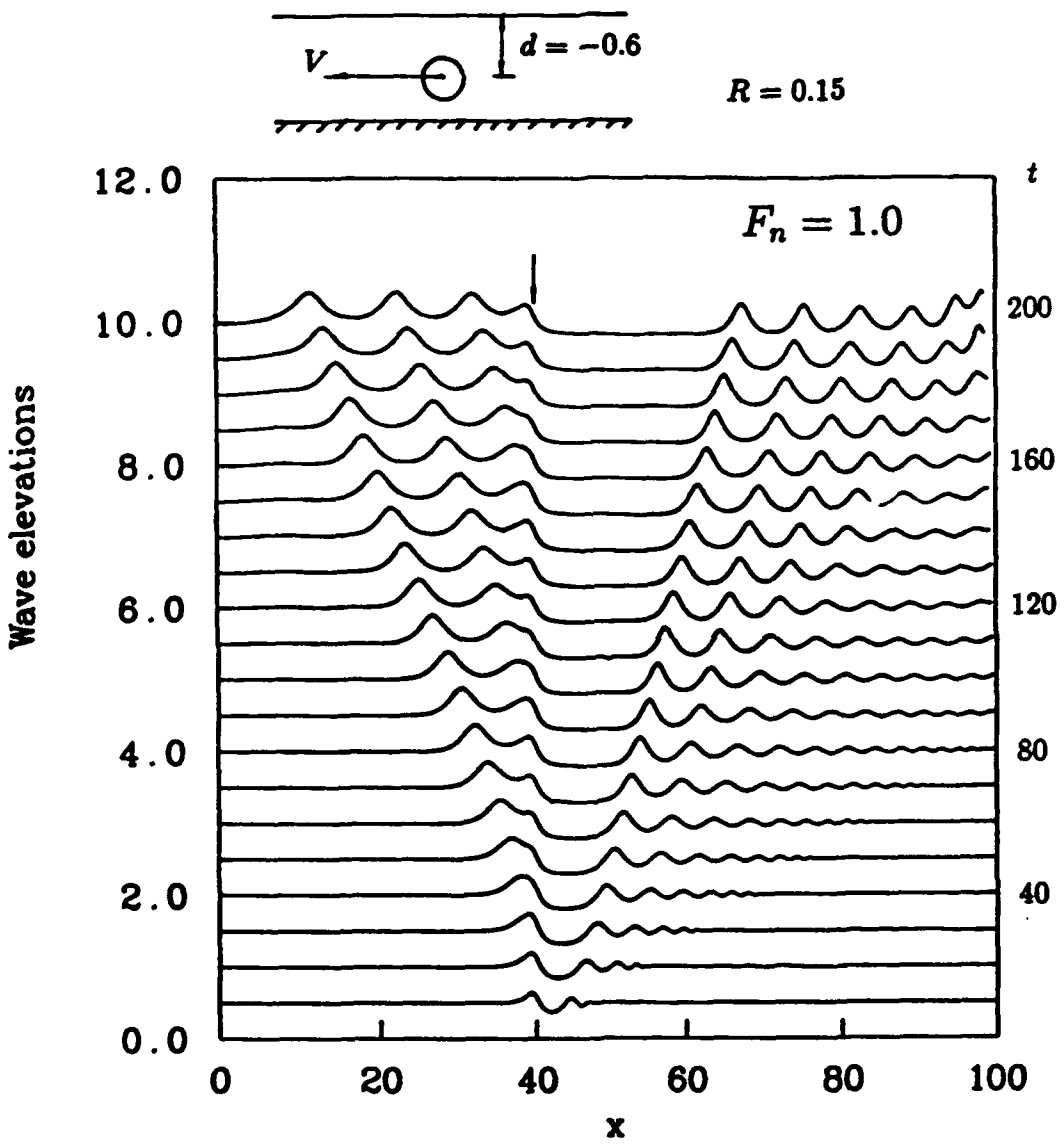


Figure 4.8: Waves due to submerged circular cylinder ($R = 0.15$, $h_c = 0.6$, $F_n = 1.0$, $\Delta t = 0.2$)

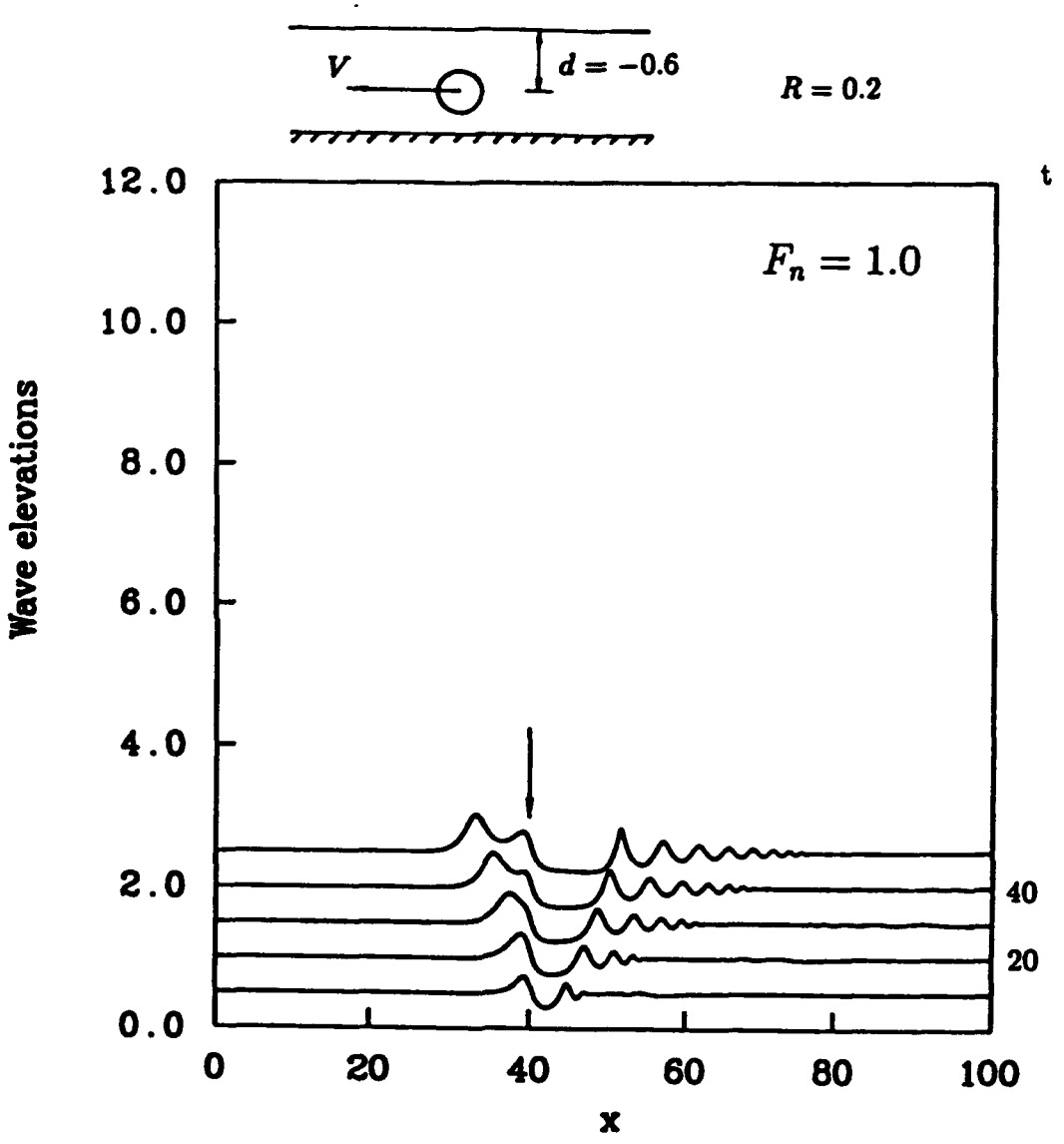


Figure 4.9: Waves due to submerged circular cylinder ($R = 0.2$, $h_c = 0.6$, $F_n = 1.0$, $\Delta t = 0.2$)

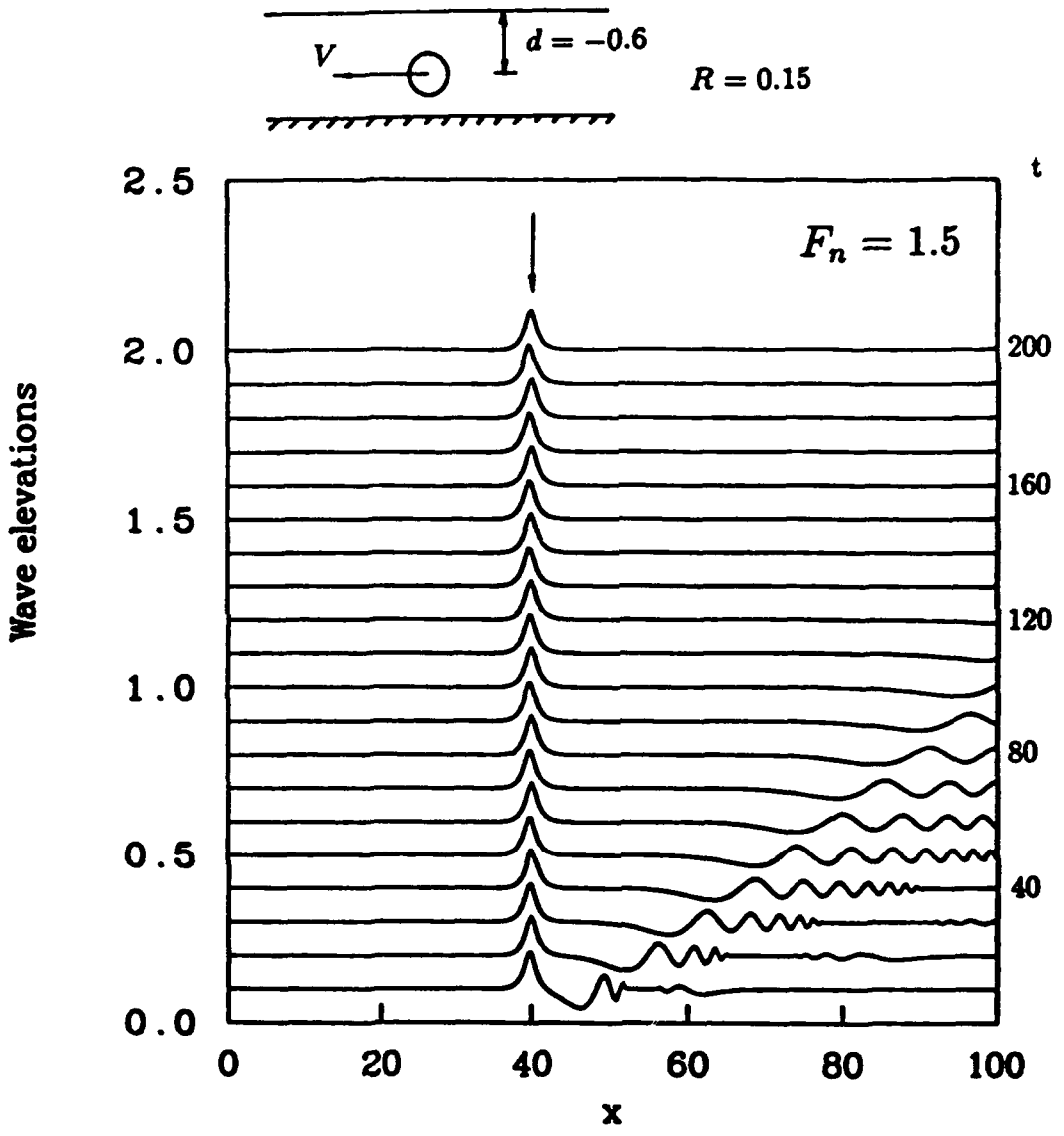


Figure 4.10: Waves due to submerged circular cylinder ($R = 0.15$, $h_c = 0.6$, $F_n = 1.5$, $\Delta t = 0.2$)

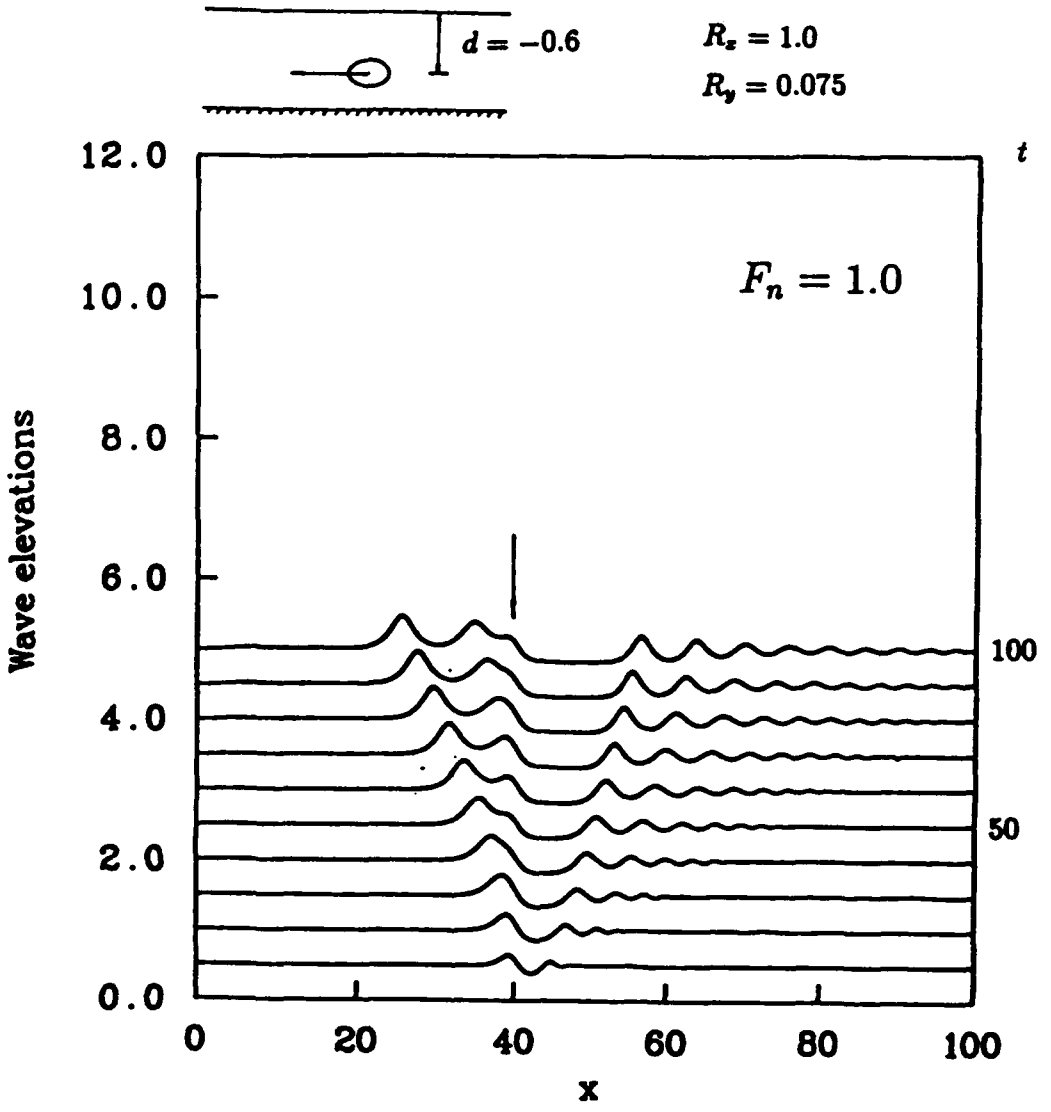


Figure 4.11: Waves due to submerged elliptical cylinder ($R_x = 1.0$, $R_y = 0.075$, $h_c = 0.6$, $F_n = 1.0$, $\Delta t = 0.2$)

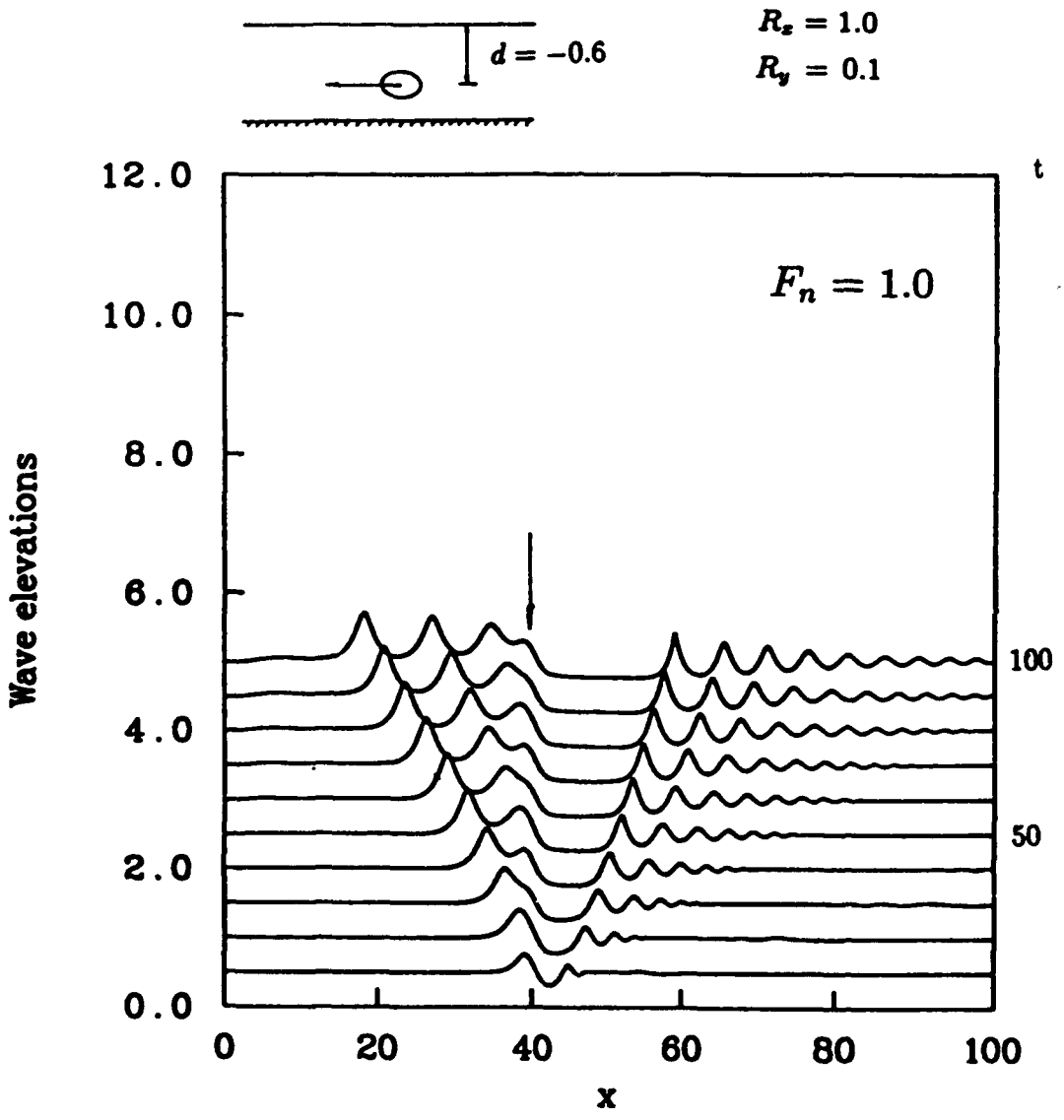


Figure 4.12: Waves due to submerged elliptical cylinder ($R_x = 1.0$, $R_y = 0.1$, $h_c = 0.6$, $F_n = 1.0$, $\Delta t = 0.2$)

CHAPTER V

WAVES GENERATED BY A SUBMERGED SPHEROID

In this chapter, the desingularized boundary integral equation is applied to a spheroid moving below a free surface. The waves due to a submerged spheroid have been studied by many researchers and used to check various theories and numerical methods (Doctors & Beck 1987, Havelock 1931, Farell 1973a,b, Bertram 1990, and Magee 1991).

For a steady problem, Doctors & Beck (1987) linearize the free surface condition about uniform flow and solve the resulting classical Neumann-Kelvin problem using a panel method with Kelvin sources of constant strength over each panel. Bertram (1990) uses the Rankine source method of Jensen, Mi & Sõding (1986). In their method, discrete sources are distributed above a finite section of the free surface to fulfill the free surface boundary conditions. On the body surface, polygonal panels of constant strength are distributed. The nonlinear free surface boundary condition is met using an iterative scheme that linearizes around an approximation from previous iteration. The potential and wave elevation are improved in each iteration. The radiation and open boundary conditions are enforced by shifting sources versus collocation points on the free surface.

For an unsteady problem with forward speed, Magee (1991) uses a time-domain analysis to solve the unsteady Neumann-Kelvin problem. In his analysis, the body boundary condition is applied on the exact time-dependent body surface, while the linear free surface condition is retained which allows the use of the time-domain Green function. Since the Green function satisfies the free surface and radiation conditions, unknowns need only be distributed on the body surface at any instant of time. However, because of the memory effect from the free surface, a large computer storage is required to store the strengths and the positions of the sources in order to evaluate the convolution integral. The storage requirement is proportional to the simulation time, which may prohibit large time simulations.

We apply the desingularized method for the unsteady problem. Discrete Rankine sources are distributed above the truncated free surface and inside the spheroid. The evaluation of Rankine sources is very fast, especially on a supercomputer since a very high level of vectorization can be achieved because of the simplicity of the Rankine source. The errors due to the free surface truncation is expected. With a proper implementation of the open boundary conditions, the truncation error can be reduced to minimal.

The spheroid, with the diameter-length ratio D/L equal to 0.2, starts to move horizontally from rest in the $-x$ direction at the depth H below the free surface and reaches an ultimate steady velocity. The flow is at rest until the spheroid starts to move and will eventually reach a steady state in the moving coordinate system. The flow is symmetric about the Oxz plane. The computation will take advantage of this symmetry. The problem is nondimensionized by making the length of the spheroid L, the gravity g, and the fluid density ρ unity.

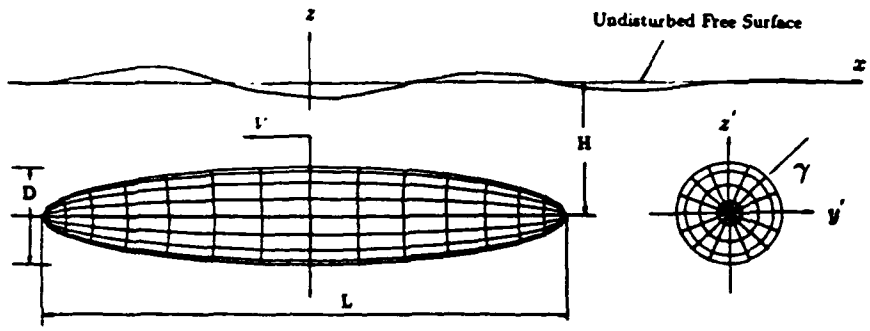


Figure 5.1: The coordinate and the discretization of the spheroid

5.1 Numerical Aspects

The free surface is discretized using N_x^f nodes and N_y^f nodes in the x and y directions, respectively, to form $N^f = N_x^f \times N_y^f$ free surface nodes within a computational domain $0 \leq x \leq R_x$ and $0 \leq y \leq R_y$. The initial grid has an equal spacing in the x direction and an algebraically increasing spacing in the y direction further from the symmetric plane. On the spheroid, the grid lines are spaced uniformly in the circumferential direction. The grid lines have a cosine spacing in the longitudinal direction. The body has a grid with N_x^b elements in x direction and N_θ^b elements in the circumferential direction, resulting in $N^b = (N_x^b - 1) \times (N_\theta^b + 1) + 2$ nodes including the two end points on the body surface, Fig. 5.1.

We construct the solution using a source distribution on a surface (S_f') above the free surface and a source distribution on a surface (S_b') inside the body surface. For a better computational open boundary behavior, we add the negative images of the source distribution on S^b about the undisturbed free surface. So the potential is

expressed as

$$\phi(\vec{x}) =$$

$$\int\int_{S_f'} \sigma^f(\vec{x}^f)\,\{\frac{1}{|\vec{x}-\vec{x}^f|}\}ds + \int\int_{S_b'} \sigma^b(\vec{x}^b)\,\{\frac{1}{|\vec{x}-\vec{x}^b|} - \frac{1}{|\vec{x}-\vec{\bar{x}}^b|}\}ds$$

$$\approx \sum_{j=1}^{N^f} \sigma_j{}^f\,\{\frac{1}{|\vec{x}-\vec{x}_j^f|}\} + \sum_{j=1}^{N^b} \sigma_j{}^b\,\{\frac{1}{|\vec{x}-\vec{x}_j^b|} - \frac{1}{|\vec{x}-\vec{\bar{x}}_j^b|}\}, \tag{5.1}$$

where $\vec{x}^f$ is the point on S_f', $\vec{x}^b$ is the point on S_b' and $\vec{\bar{x}}^b$ is the image of $\vec{x}^b$. By applying the free surface boundary condition (2.12) and the body boundary condition (2.13), we obtain a system of linear equations for the unknown strength of the singularities,

$$\sum_{j=1}^{N^f} \sigma_j{}^f\,\{\frac{1}{|\vec{x}_{f_i}-\vec{x}_j^f|}\} + \sum_{j=1}^{N^b} \sigma_j{}^b\,\{\frac{1}{|\vec{x}_{f_i}-\vec{x}_j^b|} - \frac{1}{|\vec{x}_{f_i}-\vec{\bar{x}}_j^b|}\} = \phi_o(\vec{x}_{f_i})$$

$$(i = 1, 2, ..., N^f) \tag{5.2}$$

$$\sum_{j=1}^{N^f} \sigma_j{}^f\,\frac{\partial}{\partial n}\{\frac{1}{|\vec{x}_{b_i}-\vec{x}_j^f|}\} + \sum_{j=1}^{N^b} \sigma_j{}^b\,\frac{\partial}{\partial n}\{\frac{1}{|\vec{x}_{b_i}-\vec{x}_j^b|} - \frac{1}{|\vec{x}_{b_i}-\vec{\bar{x}}_j^b|}\} = \vec{V}\cdot\vec{n}(\vec{x}_{b_i})$$

$$(i = 1, 2, ..., N^b) \tag{5.3}$$

where $\vec{x}_{f_i}$ and $\vec{x}_{b_i}$ are the control points on S_f and S_b. After σ^f and σ^b are determined, the fluid particle velocities on the free surface can be calculated. Then the time-stepping procedure integrates the free surface boundary conditions.

Similar to the two-dimensional problem in Chapter 4, the fourth-order Runge-Kutta-Felhberg method and the computational window shifting technique are used in the time stepping with a simpler implementation of the open boundary conditions. Each time the window is shifted one row of node points are dropped at the down-stream side of the window without any special treatment since no spatial derivative of the free surface is required. For the upstream boundary, a row of new node points

enter the window with homogeneous conditions. Because of an additional dimension, the flow decays from the disturbance more rapidly in the three-dimensional case than in the two-dimensional case. Therefore, the easier and simpler implemention of the open boundary condition can be used in many three-dimensional wave problems. It will be shown that this technique works very well in the numerical computations.

The pressure on the body surface is evaluated using the Bernoulli equation:

$$-p = \frac{\partial \phi}{\partial t} + \frac{1}{2}|\nabla \phi|^2 + z = \frac{\delta \phi}{\delta t} + (\frac{1}{2} \nabla \phi - \vec{V}_b) \cdot \nabla \phi + z, \tag{5.4}$$

where $\frac{\delta \phi}{\delta t} = (\frac{\partial}{\partial t} + \vec{V}_b \cdot \nabla)\phi$ is the substantial derivative of the potential at fixed points on the body surface. The nondimensional velocity of the spheroid is

$$\vec{V}_b = -F_n(1 - e^{-\mu t})\, \vec{i}. \tag{5.5}$$

The Froude number F_n is defined as $F_n = U/\sqrt{gL}$, where U is the ultimate steady velocity of the spheroid.

The drag F_x, lift F_z, and moment M on the body are calculated by integrating the pressure over the body surface using (2.17) and (2.18) in conjunction with Simpson's rule. The hydrodynamic coefficients are defined as

$$C_W = \frac{F_x}{\frac{1}{2}\rho U^2 A}, \quad C_L = \frac{F_z}{\frac{1}{2}\rho U^2 A}, \quad \text{and} \quad C_M = \frac{M}{\frac{1}{2}\rho U^2 A L}, \tag{5.6}$$

where A is the surface area of the spheroid.

The mesh size on the free surface is usually larger than that on the body by about 10 times and the differences in the magnitudes of the coefficient matrix elements are large. Therefore, the resulting system for σ_f and σ_b, (5.2) and (5.3), as a whole is likely to be poorly conditioned. To avoid this numerical difficulty, we split the

system into two subsystems, (5.2) for σ_f and (5.3) for σ_b, which are alternately solved using LU decomposition for each subsystem. In other words, σ_f is solved by (5.2) with σ_b known and σ_b is then corrected by (5.3) with σ_f known. The process goes forth and back between (5.2) and (5.3) until the error criterion is met. Each set of equations is much better behaved and more accurate solutions can be obtained. Another advantage of splitting is that the coefficient matrix for σ_b does not change with time and needs only to be inverted once for the entire time simulation. The matrix for σ_f does not change during the iteration between the body and the free surface and only needs to be inverted once for the current instant of time. Of course, the coefficient matrix for σ_f changes at the next instant of time.

The pressure on the body is evaluated at the node points. The substantial derivative of the potential $\frac{\delta\phi}{\delta t}$ in (5.4) is calculated using a four-point forward difference scheme. The fourth-order Runge-Kutta-Fehlberg method is used in the nonlinear free-surface integration. An initial time increment is set, but is modified by the Runge-Kutta-Fehlberg subroutine where appropriate.

5.2 Results

On the free surface, we use 61 × 16 nodes within $0 \leq x \leq 7.5$ and $0 \leq y \leq 1.875$, and symmetry about $y = 0$ is assumed. The spacing in the y direction increases by 10 percent for each row of nodes further from the centerline. For comparisons to the results presented in Doctors & Beck (1987), we use the same submergence depths of the spheroid ($H/L = 0.16$ and 0.245).

Fig. 5.2 shows isometric and contour plots of the waves caused by the spheroid for $H/L = 0.245$ and $F_\tau = 0.6$ at $t = 25$. A smooth startup $\mu = 2$ in (5.5) and

$N_x^b = 2N_\theta^b = 16$ are used. Fig. 5.3 shows the drag, lift and moment acting on the spheroid as a function of time. They approach the steady state values after the body has moved 10 to 15 body lengths. Fig.5.4 shows the effects of two different startups of the body on the hydrodynamic forces. In the two startups ($\mu = 2$ and ∞), the body experiences large differences in force acting on it during the transition; eventually the forces approach the same steady state values. We also notice that the body experiences a negative drag for a short time soon after the impulsive startup.

Fig. 5.5 compares the pressure on the spheroid using the present method and the Neumann-Kelvin calculation (Magee 1990) at $t = 25$ for the same conditions. The comparison is made for the pressure on the top, bottom and side of the spheroid. In the Neumann-Kelvin calculation, the body surface is divided into flat panels with distributions of constant source strength. The strength is determined by satisfying the body boundary condition at the centers of the panels. The pressure is calculated at the center points. The pressure elsewhere is obtained by interpolation. The differences between the linear and the nonlinear results are noticeable.

Fig. 5.6 shows the convergence of the drag, lift and moment with respect to the node number N^b, with $N_x^b = 2N_\theta^b = 8,\ 12,\ 16$ and 20. For all these cases, the free surface grid (61×16) adequately resolves the waves.

Comparisons of the hydrodynamic coefficients at different Froude numbers to the Neumman-Kelvin calculations (Doctors & Beck 1987) and other calculations by Bertram *et al* (1991) and Boppe (1990) are shown in Fig. 5.7 for $H/L = 0.245$ (Note: the moments in the Fig. 5.7 are taken about the vertical projection of the spheroid centroid onto the undisturbed free surface. The moments shown in the other figures are taken about the centroid of the spheroid). Bertram's calculation is based on the

method of Jensen, Mi and Söding (1986). Boppe's calculation uses a Dawson-type scheme. Their calculations solve the boundary value problem for steady flow. Our calculations solve the initial boundary value problem for unsteady flow generated by the spheroid starting from rest. After the spheroid reaches it final constant speed, the flow will become steady as $t \rightarrow \infty$. Our results in Fig. 5.7 are obtained by curve fit assuming the unsteady components decay at $O(t^{-1})$ according to Wehausen (1964). A finer free surface grid (71×16) is used for smaller Froude numbers ($F_n = 0.3$ and 0.4) to resolve the shorter waves. Our results agree well with the linear results of Doctors & Beck (1987) at low Froude number as expected since the nonlinear effects are presumably small for low Froude number. As the Froude number increases, the difference between our results and the linear results increase since the nonlinear effects are expected to become larger. Also notice that there are differences between different calculations, especially for large Froude number. This may be due to the different truncations in our calculations and the other calculations or due to the error from the curve fitting for large time asymptotic values in our calculations. Nevertheless, the agreement is good in general.

For $H/L = 0.16$, nonlinear effects seem very strong. For all attempted Froude numbers (F_n=0.4, 0.5, 0.6, 0.7 and 0.8), the free surface in our computation is sucked down and touches the body surface which in turn stops the computation. A smoother start up could delay the surface piercing of the body. It seems that in our calculations, the acceleration of the body specified is too large so that the initial start-up causes surface piercing of the body. It is also possible for this to happen even if the acceleration is very small but the final speed is high. Surface piercing of the body also occurs in Bertram's steady calculation (Bertram 1990) at high Froude number ($F_n = 0.8$). The linear calculations are not affected by this because the free

surface boundary conditions are satisfied at $z = 0$. The surface piercing of the body needs to be verified by experiments.

The waves generated by the spheroid and those generated by the relevant simple source-sink pair disturbance are compared (Fig. 5.2 and Fig. 5.8). The strength of the pair and the distance between the source and sink are determined to give a Rankine oval having the same length and midsectional area as the spheroid moving in an infinite fluid. The comparison becomes meaningless if the disturbance is too close to the free surface because the simple source-sink no longer represents the body well. The same depth of submergence, location of the center and motion of the disturbance as those for the spheroid are used for a direct comparison. Comparison of Fig. 5.2 and Fig. 5.8 shows that the wave patterns of the spheroid and the relevant source-sink are very similar except that the spheroid generates steeper waves near the stern.

The computations are carried out on a Cray Y-MP. The results shown in Fig. 5.2 take approximately 4.3 CPU seconds to solve the boundary value problem (5.2) and (5.3) in which 10 percent of this time is required for the matrix setup. About 5 iterations between (5.2) and (5.3) are required. The CPU time for the entire time simulation is 45 minutes. For the simpler disturbance in Fig. 5.8 it takes approximately 3.9 CPU seconds to solve (5.2) and 40 minutes for the entire time simulation. In the later case, only (5.2) needs to be solved. The difference in the CPU time for the two computations is not significant because the splitting procedure for the body problem only requires an additional evaluation of multiple right-hand sides.

A faster iterative matrix solver can be used effectively for the source-sink pair

disturbance to further reduce the computation time. Although GMRES could have been used for the whole system in the spheroid example, it would require special preconditioning. We tried solving the whole system for the spheroid example using both LU decomposition and GMRES without preconditioning. The LU algorithm gave inaccurate solutions while GMRES did not converge.

Fig. 5.9 shows the effect of desingularization ($l_d = 0.5, 1.0, 2.0, 3.0$ and 4.0) on the wave computations. The results are not significantly affected except for $l_d = 0.5$, which becomes too small and the integration by summation (or one point Gauss quadrature) is too crude.

We also performed an energy conservation check for a fixed control volume bounded by the free surface, the body surface, a horizontal bottom and four vertical surfaces representing the truncated far-field boundaries. The body starts to move from rest at the center of the control volume. The energy of the fluid in the control volume and the work done by the body are shown in Fig. 5.10. The energy and the work balance each other well until $t = 6$ when the waves and the body reach the truncated boundary. Since the energy flux is neglected in the energy calculation, agreement is not to be expected after the body or the waves reach the boundary.

5.3 Conclusions

Desingularization performs well for fully nonlinear free surface problems of a submerged spheroid. Desingularization is not numerically dispersive (Fig. 5.9) nor dissipative (Fig. 5.10). Iteration between the free surface and the body surface boundary conditions is required for the not well-conditioned matrix equation without preconditioning. The waves produced by the spheroid and the relevant source-sink

disturbance are similar if they are sufficiently submerged. This indicates that a simple disturbance (with a much simpler iterative procedure and fewer unknowns) can be used if the surface waves are the main interest. In general, the comparison of the hydrodynamic coefficients by our results to those by other calculations is good for $H/L = 0.245$. For $H/L = 0.16$, our method predicts the surface piercing of the body, which needs to be verified by experiments.

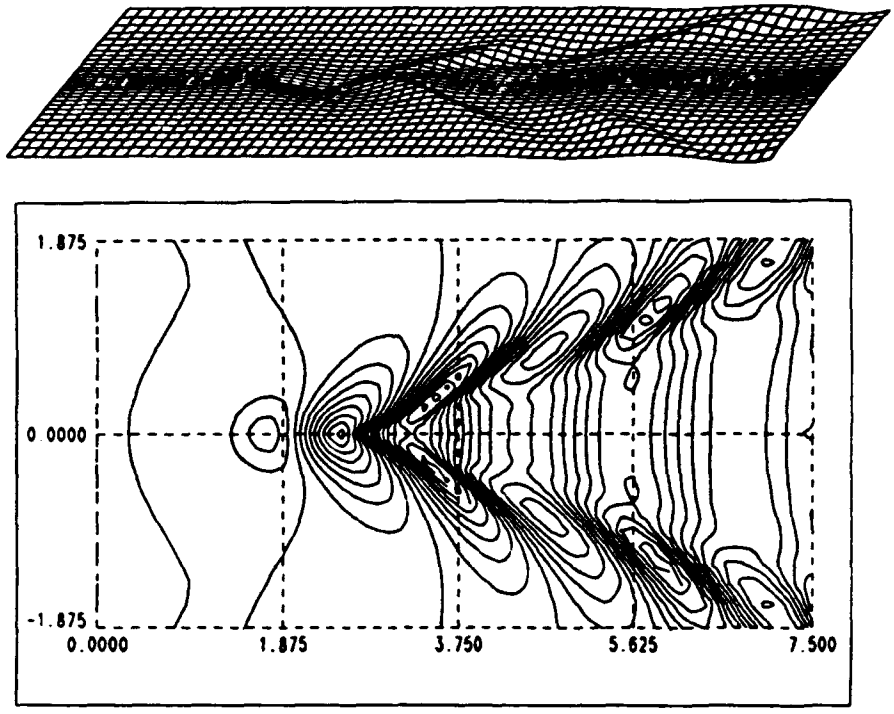


Figure 5.2: Waves generated by the spheroid, above: isometric view, below: wave elevation contours (0.02 apart)

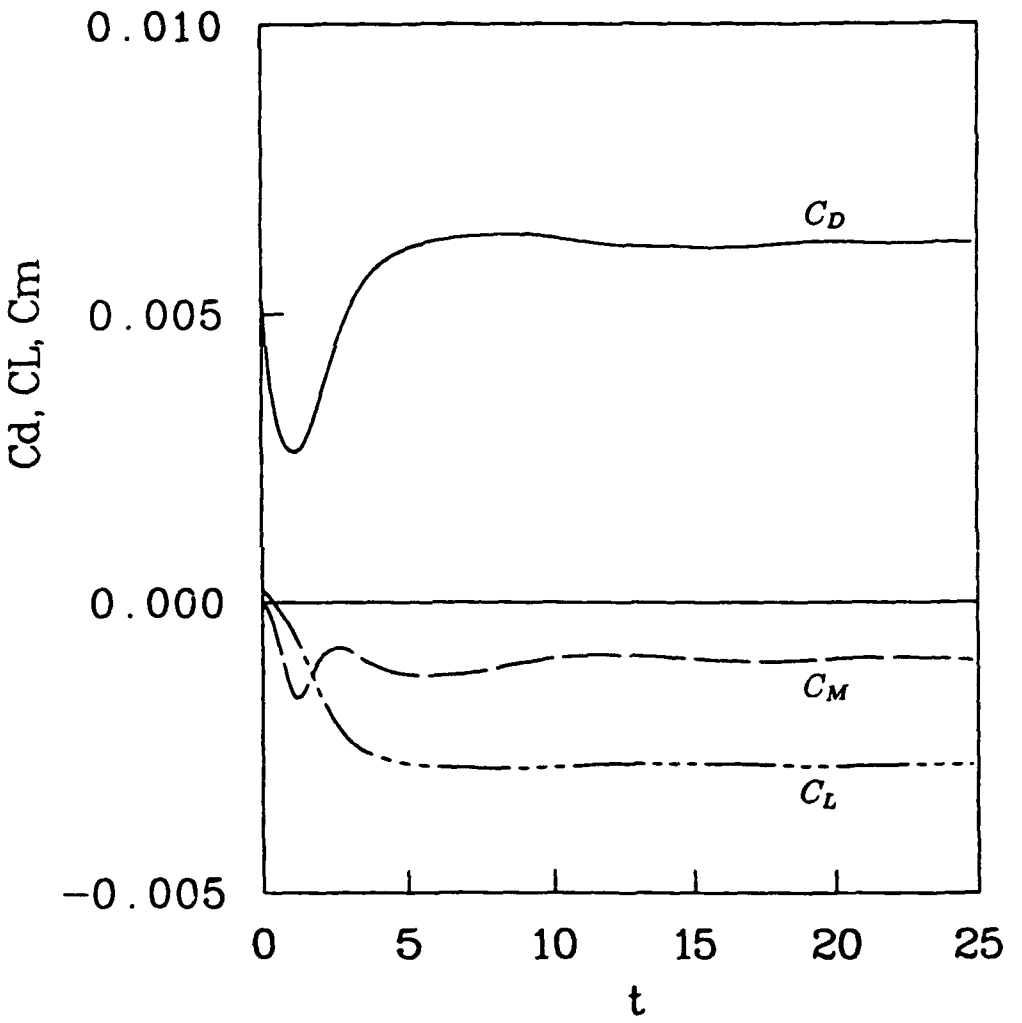


Figure 5.3: Hydrodynamic coefficients vs. time

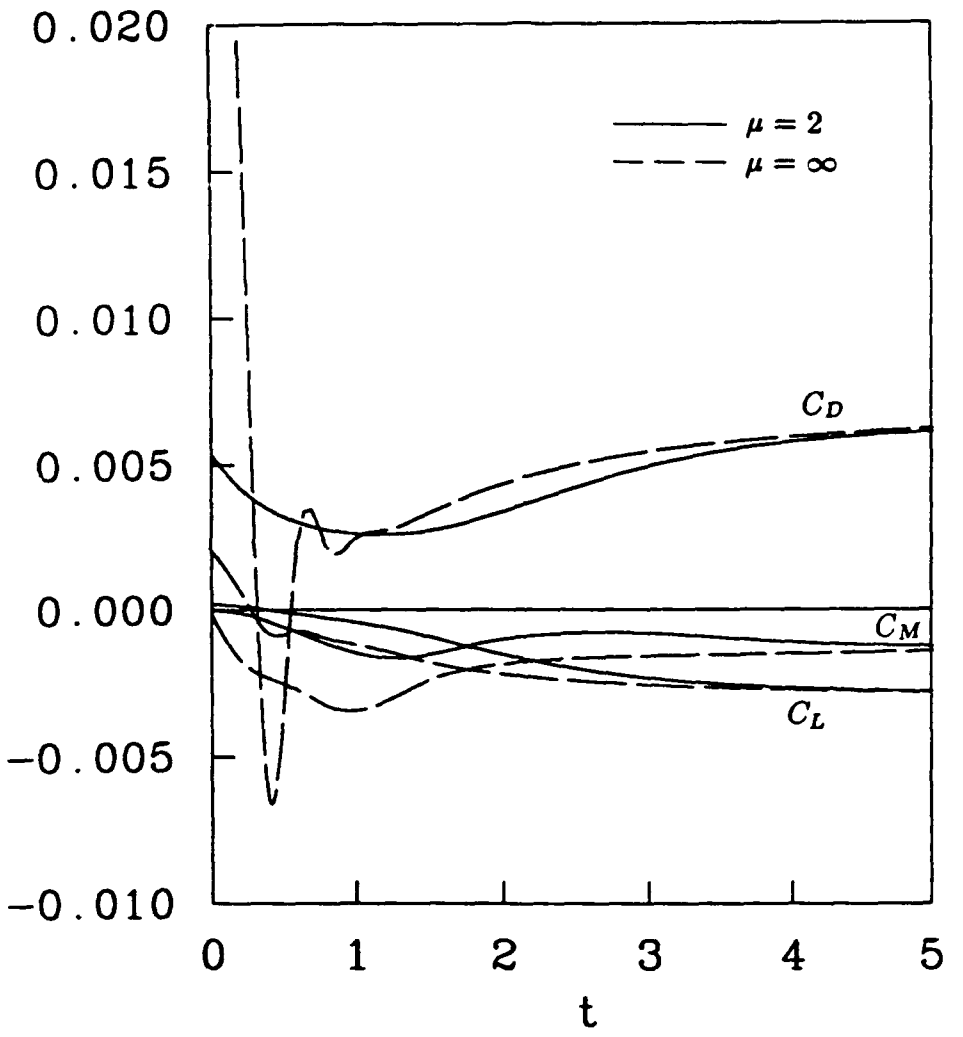


Figure 5.4: Influence of start-up of the spheroid

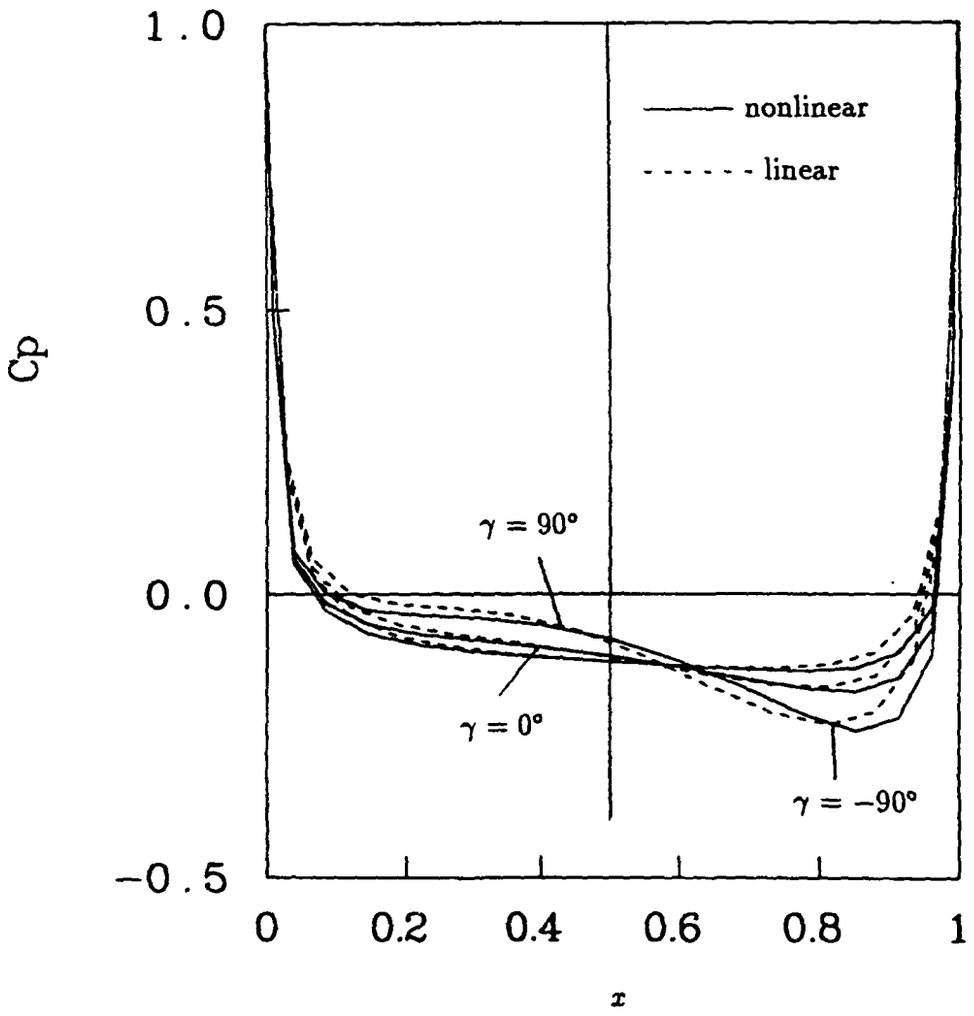


Figure 5.5: Pressure on the s roid surface

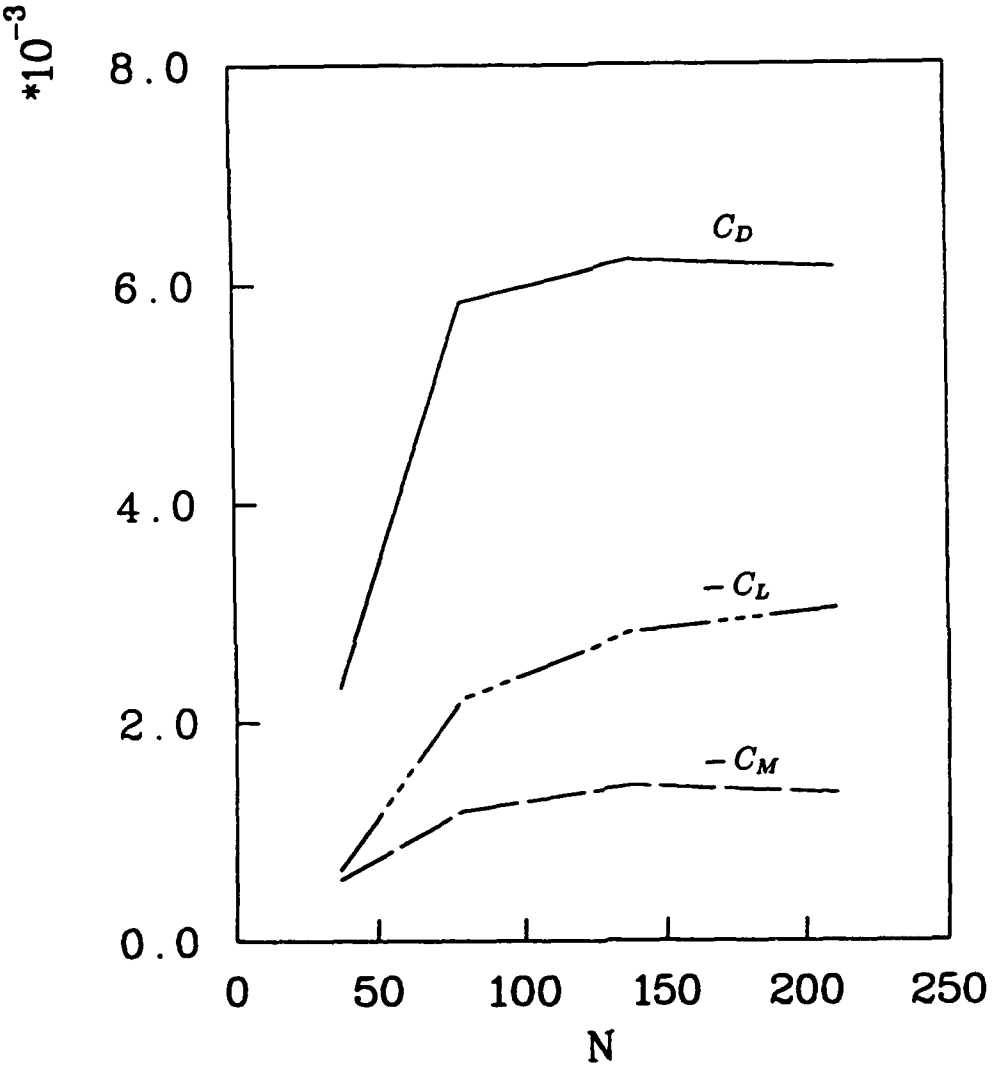


Figure 5.6: Sensitivity of the spheroid surface mesh size

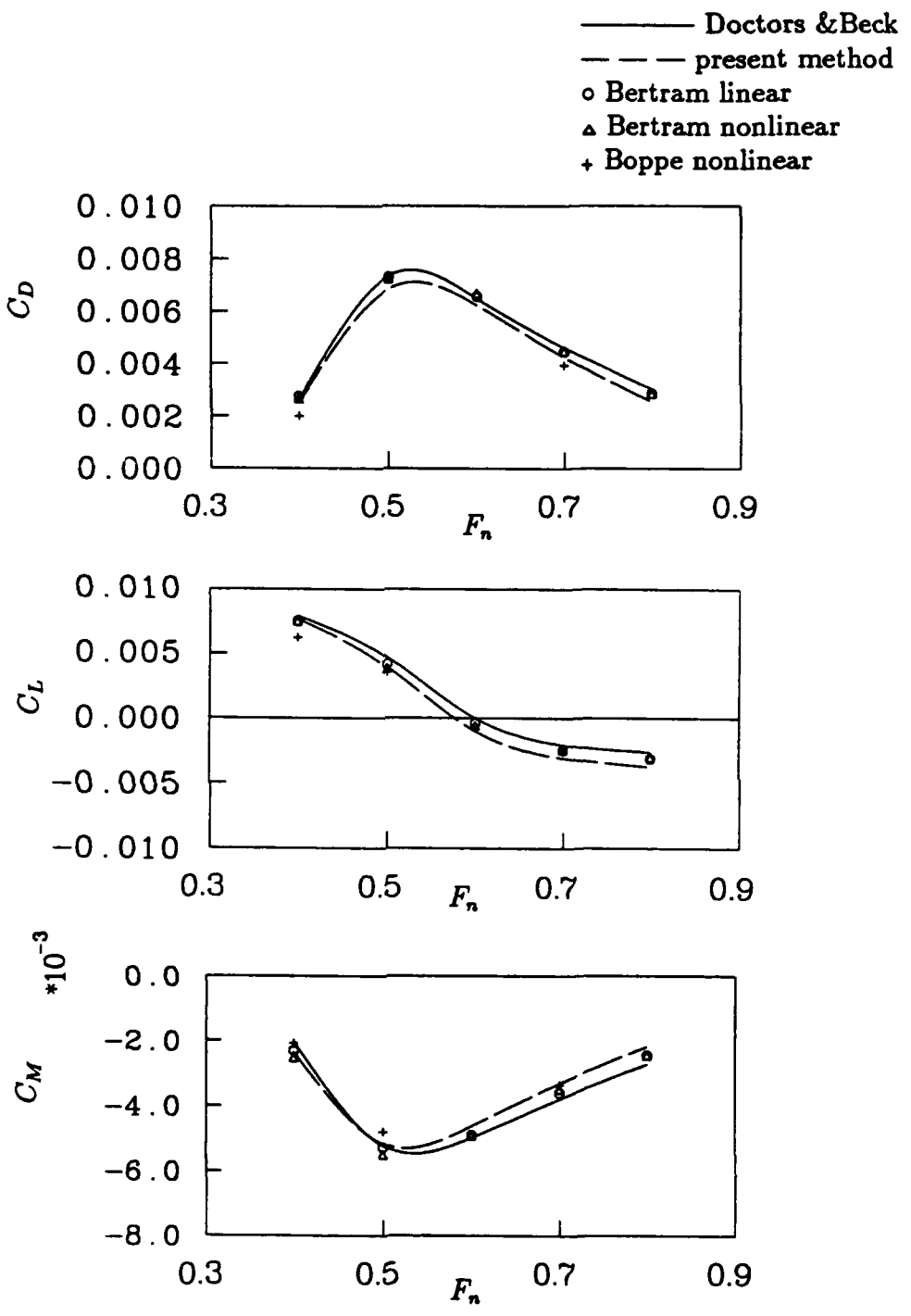


Figure 5.7: Comparison of hydrodynamic coefficients (modified from Doctors & Beck with the present results added)

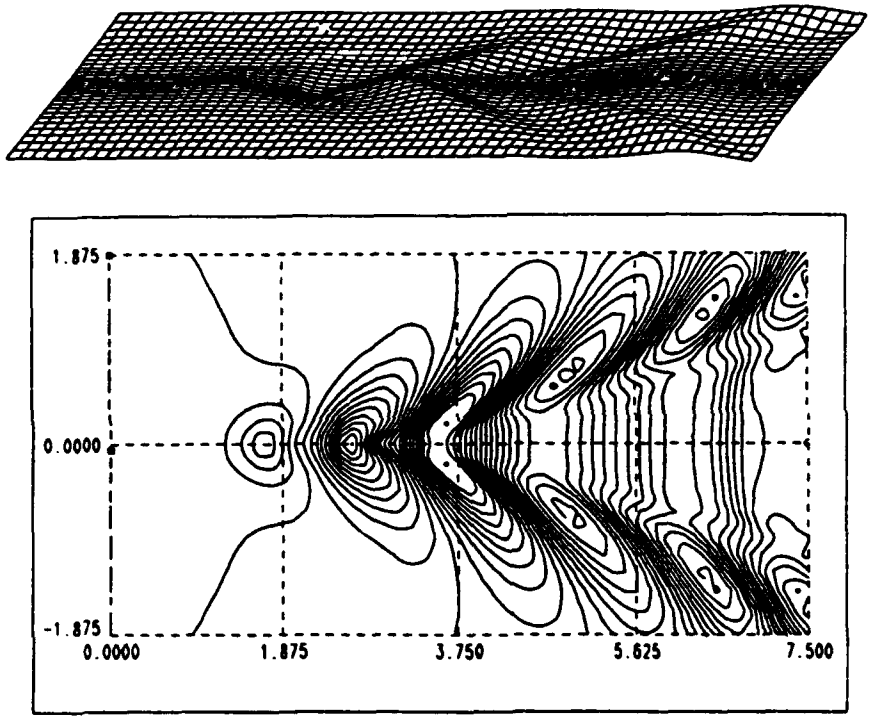


Figure 5.8: Waves generated by the relevant source-sink pair, above: isometric view, below: wave elevation contours (0.02 apart)

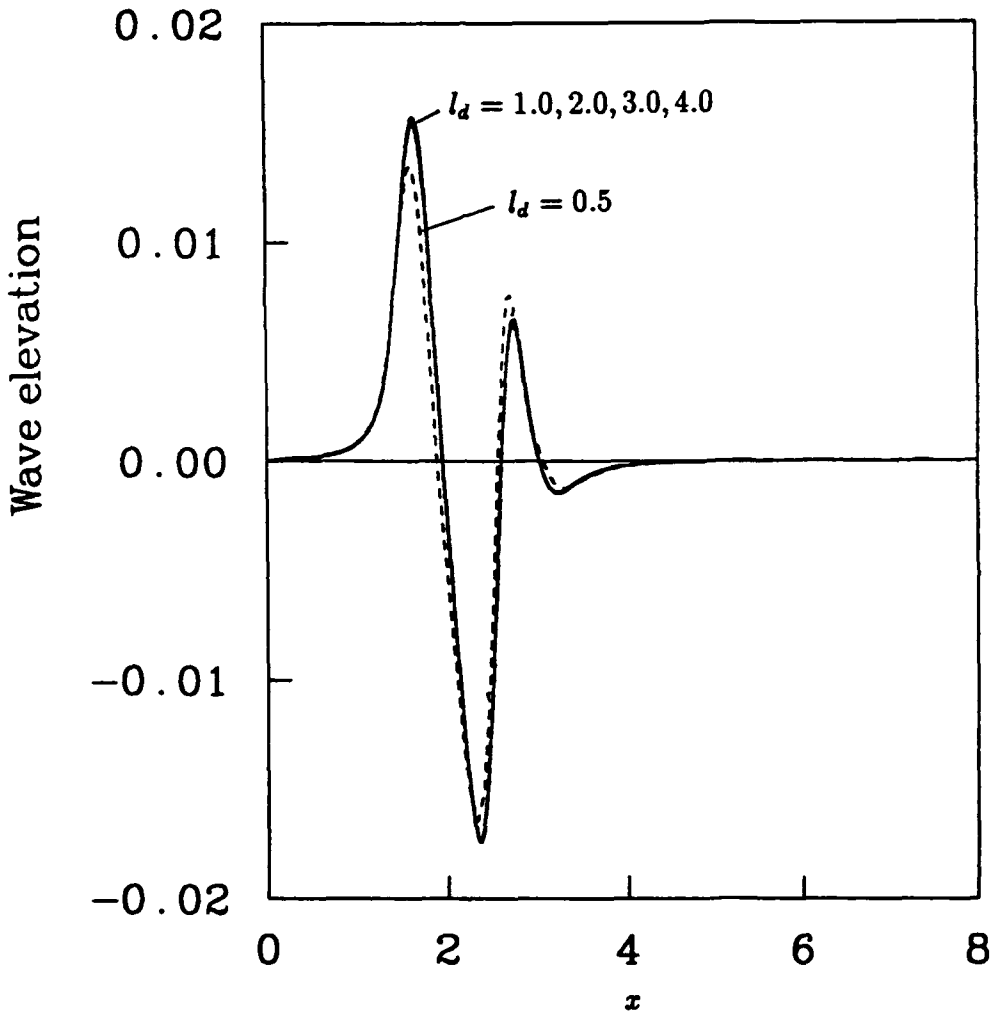


Figure 5.9: Effect of desingularization factor l_d

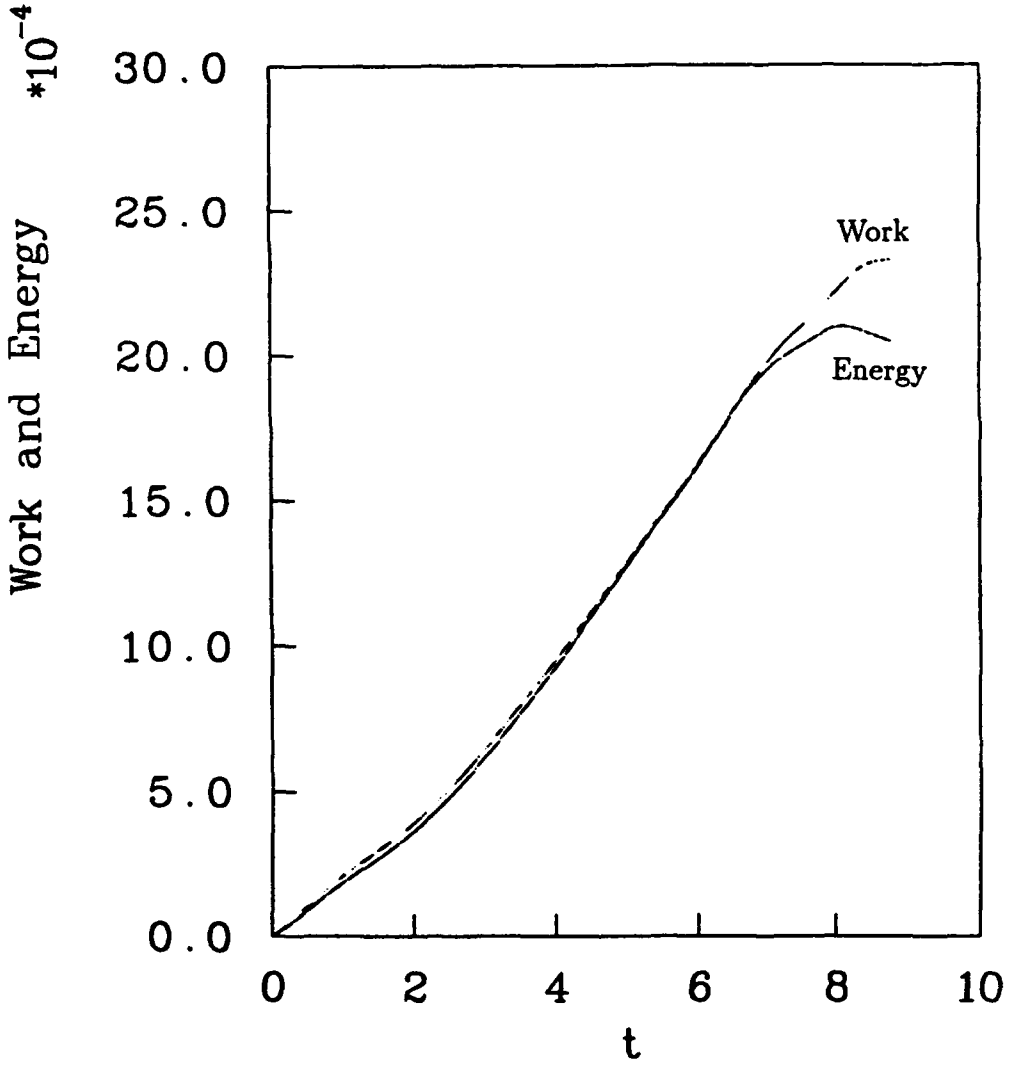


Figure 5.10: Wave energy and work done by the spheroid

CHAPTER VI

UNSTEADY WAKE AND INNER-ANGLE WAVEPACKETS

Recent observations (SAR images from the space shuttle and aerial photographs) of the ship wakes sometimes reveal a narrow V wave pattern in addition to the the classical Kelvin wake (Fu & Holt 1982, Munk *et al.* 1987, Brown *et al.* 1989, Reed *et al.* 1991 and the articles in JOWIP and SARSEX Special Issue, *Journal of Geophysical Research* 1988). According to available observations, a ship wake can consist of the following three types of structures, although this classification is not very precise: 1) the usual Kelvin wake component consisting of transverse waves and diverging waves, both within the classical 19.5 degree cusp line; 2) the narrow V-wake typically appearing in the SAR image as a narrow bright V of half-angle 2 to 3 degrees with a centerline dark area within the V; and 3) the relatively isolated wavepacket of about 10 to 11 degrees, *e.g.* as recently observed in the wake of the U.S. Coast Guard cutter Point Brower, (Brown *et al.* 1989). The packet persists for several kilometers behind the ship. Here we will call this isolated wavepacket inner-angle wavepacket to distinguish it from the very narrow V-wake of half-angle 2 to 3 degrees. More detailed descriptions about the ship wake can be found in the papers mentioned above.

Although there are many theoretical uncertainties as well as voids in experimental data, it is believed that the very narrow V-wakes are associated with turbulence, internal waves, wave breaking, nonlinear effects as well as surfactant effects (Reed *et al.* 1991). The generation mechanism responsible for inner-angle waves and their relation to the ship characteristics are also not clear. The typical wavelength of the inner-angle waves is much larger than those in the very narrow V-wakes and has the same order as that of the Kelvin components. This can be easily seen in the aerial photograph of the wake of the Coast Guard cutter Point Brower (figure 2 in Brown *et al.* 1989). The inner-angle waves will be studied in this chapter. The most probable hypotheses of the causes for the inner-angle waves are: 1) interference due to the linear superposition of the wave fields generated by the bow and the stern; 2) nonlinear effects; and 3) unsteadiness of the waves. We will investigate all three cases in this chapter.

Linear interference has been studied by Hall & Buchsbaum (1990) using a submerged source-sink pair as well as a line source distribution to model the ship. The linear free surface boundary condition was satisfied. They were able to generate an inner-angle wavepacket using this model. However, the wavepacket spreads faster than the observed data. Brown *et al.* (1989) found that the decay rate of the inner-angle wave amplitude predicted by linear steady Kelvin wake theory was faster than the observed decay rate. According to Hall & Buchsbaum (1990), Brown *et al.* (1989), as well as Akylas *et al.* (1989), nonlinear effects play an important role in the generation of the inner-angle waves.

Most studies to date on this inner-angle phenomenon focus on nonlinear effects. No comprehensive nonlinear models have been developed to calculate the entire wave

field of a ship, although considerable study has been conducted on certain aspects. Most studies use a perturbation method to account for nonlinear effects (Akylas *et al.* 1988, Brown *et al.* 1989, and Hall & Buchsbaum 1990). A two-dimensional nonlinear Schrödinger equation for the wave envelope is derived assuming a narrow band of frequencies for the carrier waves along the ray of the inner-angle wavepacket. The wave envelope from the nonlinear Schrödinger equation can support solitary wave solutions (hence the terminology inner-angle soliton). However, the use of the envelope equation implies that the wavelength of the carrier waves is much smaller that the envelope width, which often seems not to be the case in visual observations. Moreover, as pointed out by Wu (in discussion of Akylas *et al.* 1988), the carrier waves are not perpendicular to the envelope track and hence it is an open question whether the asymptotic radiation of the envelope wave packets can be satisfactorily explained by local group velocity considerations.

The observed wake of the Coast Guard cutter was distorted by ambient waves, thereby limiting the comparison to averaged properties (Brown *et al.* 1989). There was still variability in the reduced data even when the components due to the ambient waves were filtered. This could be due to, in addition to the ambient waves, variation in ship speed or heading; time-dependent ship motion; interaction with the transverse Kelvin wave and the time-dependency or instability of the solitary wave envelope. Other sources of unsteadiness are the propeller-induced flow field, vortex shedding (von Kármen vortex street type) and the turbulent flow in the near field. Unsteady features of the wake may play a very important role in the generation of the inner-angle wavepackets. It is therefore desirable to investigate the unsteady phenomena of the inner-angle wavepackets.

Unsteady waves have long been studied in seakeeping. However, the main objective in seakeeping is to determine the hydrodynamic forces acting on the ship and the ship motion while little attention is given to the far-field wave patterns. Eggers (1957) studied the wave pattern due to a pulsating translating source and showed that there were three systems of constant phase curves. Recent work by Noblesse & Hendrix (1990) showed similar results. These studies have shown that the wave boundaries change with the frequency of the oscillating source. Newman (1961) studied the wave pattern due to a non-oscillating source translating in an incident wave and showed two systems of "distorted Kelvin waves". All these studies used the method of stationary phase. Jankowski (1990) studied linear time-harmonic wave patterns caused by translating and pulsating sources using fundamental solutions satisfying a linear free surface boundary condition. Nakos and Sclavounos (1990) calculated the time-harmonic wave patterns by a modified Wigley hull model translating and oscillating in heave using a Rankine panel method. However, none of the described work on unsteady wave patterns specifically tried to explain the inner-angle wavepacket phenomenon. Only recently, Mei (1991) used a unsteady, nonlinear Schrödinger equation to study the inner-angle wave phenomenon.

Since we are primarily interested in far-field waves, we simply model the ship by a source-sink pair moving below the free surface or a moving pressure distribution on the free surface. Unsteady wakes can be classified into two types: "diffraction" waves generated by a non-oscillating disturbance moving in incident waves; and "radiation" waves generated by an oscillating disturbance moving in an initially undisturbed water. Both types exist for an advancing ship in a seaway, since the seaway is not only diffracted by the presence of the ship but also causes the ship motion, which in turn generates radiation waves. We only study the "radiation" wake here, leaving

the "diffraction" type and the interaction between the two types of wakes for future study.

The following three methods are used in our study:

1. Nonlinear wave calculations: It is rather straightforward to apply the method described and used in the previous chapters. However, a large computational domain on the free surface is required because of our interests in the far field, resulting in a large number of unknowns in numerical computations (typically the number of nodes $N > 3000$). Some special techniques, such as a fast iterative solver, preconditioning and the multigrid method, are examined and employed to speed up the computations.

2. Linear wave calculations: The time domain Green function satisfying the linear free surface conditions and radiation conditions (Liapis & Beck 1986, King 1987, Beck & Magee 1990) is used to calculate the wave elevation.

3. Method of stationary phase: Although it is not easy to evaluate wave elevation by the method of stationary phase, the wave patterns determined by constant phase can be obtained without a great deal of computational effort. The constant phase lines are obtained in a similar manner as Yih & Zhu (1989a,b) with some modification. In Yih & Zhu (1989a,b), patterns of steady ship waves are analyzed with the added effects of finite depth, surface tension, and wake velocity profiles.

6.1 Nonlinear Wave Calculations

In the nonlinear calculations with a large number of nodes ($N > 3000$), an iterative solver is used to solve the system of linear equations representing the discretized

boundary integral equation:

$$\mathbf{A}\mathbf{x} = \mathbf{b}. \tag{6.1}$$

It is desirable to use a technique to accelerate the convergence. Two techniques, the multigrid method and matrix preconditioning, are tested with two iterative solvers, GMRES and a successive over-relaxation algorithm (SOR).

6.1.1 Multigrid and matrix preconditioning

Multigrid methods have been widely used and proved effective in various finite difference schemes (the working equation being of differential type). Multigrid methods have been infrequently applied to boundary integral methods (integral type). A brief description of the multigrid method used with the GMRES and SOR methods for the algebraic system resulting from the desingularized algorithm, and the discussions of the test results are given in Appendix A. Unfortunately, the test results show that the multigrid method does not help in our nonlinear wave calculations. The GMRES algorithm without a multigrid correction is superior.

The basic idea of preconditioning is to find an approximate matrix $\hat{\mathbf{A}}$ to $\mathbf{A}$ so that $\hat{\mathbf{A}}^{-1}\mathbf{A}$ closely approximates the identity matrix, yielding a strongly diagonally-dominate matrix. The preconditioned equation:

$$\hat{\mathbf{A}}^{-1}\mathbf{A}\mathbf{x} = \hat{\mathbf{A}}^{-1}\mathbf{b} \tag{6.2}$$

is then better conditioned than the original system (6.1) and can be solved with much fewer iterations. In general, it is not easy to find a good approximate $\hat{\mathbf{A}}$ matrix for a dense, nonsymmetric $\mathbf{A}$ matrix. However, we choose $\hat{\mathbf{A}}$ as $\mathbf{A}_o$, *i.e.* $\mathbf{A}$ at $t = 0$. Although the free surface shape changes with time and so does $\mathbf{A}$, $\mathbf{A}_o$ is still a very

good approximation to **A**, especially when the boundary integral is desingularized. More detail on the test results for the nonlinear wave calculations with preconditioning are given in Appendix B. We found that this preconditioning matrix is very effective in accelerating the convergence. For example, preconditioning saves over 80% of the total CPU time to solve the system of 3367 linear equations in the wave computation for 1000 time steps shown in Fig. 6.1. The preconditioning technique, not the multigrid method, is therefore used in the nonlinear wave computations.

6.1.2 Computational results

We first calculate the waves generated by a submerged source-sink pair. The separation, the depth of the submergence, and the strength of the source and the sink are chosen to approximately model the Coast Guard cutter. The cutter has a 25.3m waterline length, 5.2m beam, 1.8m draught, and the ship speed U was 7.7m/s (Brown *et al.* 1989). The source-sink pair starts to move horizontally from the rest. We use the same separation (87.7% of the waterline length), submerged depth (50% of the draught) and strength (UA_w, where $A_w = 3.3m^2$ is the submerged cross-sectional area near midship) of the source-sink pair as used by Hall & Buchsbaum (1990). The problem is made dimensionless based on the ship's waterline length. The strength of the pair are multiplied by $(1 - e^{-\mu t})$ where μ=2.0. The time simulation is sufficiently long so that the waves behind the pair achieve a steady state. Fig. 6.1 shows contour and isometric plots of the waves when the pair has traveled about 16 ship lengths. The wake is essentially a Kelvin wake although there is interference between the wave systems by the source and the sink. This interference does not form a wavepacket like the one observed in the experiment of the cutter Point Brower at an inner-angle of less than 19.5 degrees.

Fig. 6.2 shows the waves generated by two moving dipoles. The dipole strength is made as large as possible so that the waves are nonlinear but not breaking. The submergence depth of the dipole is set to 1, the separation of the dipoles is 10, and the strength is 2.5. The depth Froude number is 1.0. Fig. 6.3 and Fig. 6.4 show the waves due to two moving free surface pressure patches. Each patch has a length 1 and beam 0.2. The pressure distribution for each patch is

$$p_a(\hat{x},\hat{y}) = p_o P^x(\hat{x}) P^y(\hat{y}),$$

where

$$P^x(\hat{x}) = \begin{cases} 1 & |\hat{x}| \le 0.8 \\ \frac{1}{2}\{\cos[5\pi(\hat{x} \mp 0.8)] + 1\} & 0.8 < \pm\hat{x} \le 1 \\ 0 & |\hat{x}| > 1.0 \end{cases} \tag{6.3}$$

$$P^y(\hat{y}) = \begin{cases} 1 & |\hat{y}| \le 0.1 \\ \frac{1}{2}\{\cos[10\pi(\hat{y} \mp 0.1)] + 1\} & 0.1 < \pm\hat{y} \le 0.2 \\ 0 & |\hat{y}| > 0.2 \end{cases}$$

and $(\hat{x},\hat{y})$ are the local coordinates attached to the centroid of a patch. The centroids of the two pressure patches are separated by 1.8. In Fig. 6.3, the pressure is small ($p_o = 0.001$) so the waves are essentially linear. In Fig. 6.4, the pressure is 20 times larger so the waves are nonlinear (the maximum wave slope is about 0.30). Fig. 6.5 compares the longitudinal wave cuts of the linear and nonlinear steady waves at different y when the linear waves of Fig. 6.3 are multiplied by 20. As seen in Fig. 6.5, the nonlinear effect is not very significant and again no small angle wavepackets form. Instead, the two wave systems by the forward and aft disturbances seem parallel to each other. The computations (not shown here) using other separation distances of

the disturbances reveal the same feature, except when the separation distance is so small that the two wave systems merge into one Kelvin-type wave system.

We then calculate the unsteady wakes generated by one pressure patch of form (6.3) translating at a speed F_n and pulsating with a frequency ω such that $p_o = \hat{p_o} \sin \omega$. Figures 6.6 to 6.11 show the waves caused at different values of the reduced frequency $\tau = F_n \omega$, with $F_n = 0.4$. For small τ, two wave systems can be seen, one with a bounding angle larger than the Kelvin angle and the other smaller than the Kelvin angle. As the frequency increases, only one wave system is visible with a smaller bounding angle. Although it is not easy to measure bounding angles precisely from these contour plots, it is clear that the angles decrease with increasing disturbance frequency.

Since the pressure patch is not a point pressure, a Froude number effect is expected. Fig. 6.12 shows wave contour plots for $F_n = 0.2$ and $\omega = 5$ keeping $\tau = 1.0$. The wave orientation in relation to the wavepacket is quite different compared to that in Fig. 6.8 (with the same value of τ but $F_n = 0.4$) although the bounding packet angle is not affected.

6.2 Linear Wave Calculations

The steady nonlinear wave computations have shown that nonlinear effects are not essential to the generation of the inner-angle wavepackets while the unsteadiness of the flow can cause the inner-angle waves. Further study on the features of the unsteady wake using linear computations is suggested. We will now study the unsteady wakes by linear computations using a time-domain Green function.

6.2.1 Time-domain Green function

The time-domain Green function $G(P,P',t,t')$ we use is the potential due to an impulsive source at time t' and location P':

$$G(P,P',t,t') = \left(\frac{1}{r} - \frac{1}{\hat{r}}\right)\delta(t-t') + \tilde{G}(P,P',t,t')\,H(t-t'). \tag{6.4}$$

Here,

$$\tilde{G}(P,P',t,t') = \int_0^\infty dk\sqrt{kg}\sin\left(\sqrt{kg}\,(t-t')\right)e^{k(z+z')}J_0(kR) \tag{6.5}$$

is the wavy part, $P=(x,y,z)$ is the field point, and $P'=(x'(t'),y'(t'),z'(t'))$ is the source point. $r=[(x-x')^2+(y-y')^2+(z-z')^2]^{\frac{1}{2}}$ is the distance between the field and source points, $\hat{r}=[(x-x')^2+(y-y')^2+(z+z')^2]^{\frac{1}{2}}$ is the distance between the field point and the image of the source point, and $R=[(x-x')^2+(y-y')^2]^{\frac{1}{2}}$. J_o is the zero-order Bessel function, $\delta(t)$ is the delta function, and $H(t)$ is the unit step function.

The Green function $G(P,P',t,t')$ satisfies the following governing equation,

$$\nabla^2 G \;=\; -4\pi\delta(P-P')\,\delta(t-t'),$$

with the linear free surface condition on $z=0$,

$$\frac{\partial^2 G}{\partial^2 t} + g\frac{\partial G}{\partial z} \;=\; 0 \qquad (\text{on } z=0),$$

and the initial and far-field conditions,

$$\begin{aligned} G,\ \frac{\partial G}{\partial t} \;&=\; 0 \qquad && t-t'<0 \\ \nabla G \;&\to\; 0 \qquad && \text{as } r\to\infty \end{aligned}$$

The potential due to a source of strength $\sigma(t)$ moving in the path, $(x'=x'(t), y'=y'(t), z'=z'(t))$ is then

$$\phi(P,t) = \int_0^t \sigma(t')G(P,P',t,t')dt'. \tag{6.6}$$

The free surface elevation in the fixed coordinate system is,

$$\eta(x,y,t) = -\frac{1}{g}\frac{\partial \phi}{\partial t} \qquad (\text{on } z=0). \tag{6.7}$$

When x is replaced by $x - Vt$ and $\frac{\partial}{\partial t}$ by $\frac{\partial}{\partial t} + V\frac{\partial}{\partial x}$, one obtains the wave elevation in the coordinate system moving with velocity V in the $-x$ direction,

$$\eta(x,y,t) = -\frac{1}{g}(\frac{\partial \phi}{\partial t} + V\frac{\partial \phi}{\partial x}) \qquad (\text{on } z=0). \tag{6.8}$$

We use the subroutine initially developed by Liapis (1986) and later improved by King (1987) and Magee (1990) to calculate $G(P,P',t,t')$. The time convolution integral in (6.6) is performed using a simple trapezoidal rule.

6.2.2 Computational results

Since discretization of the free surface is not necessary in the linear calculations, less computation time is required compared to the nonlinear wave calculations. Therefore, we are able to consider a larger free surface area with a finer grid. The disturbance used is a source-sink pair. The submergence depth is 1. The separation of the source and sink is also 1. The problem is made dimensionless based on the depth. Figures 6.13 to 6.17 show the wave patterns by a translating and pulsating source-sink pair with zero-mean strength for different values of τ. Similar to the nonlinear computations, two wave systems can be identified at low frequency. Again, as the frequency increases, the angles of the two wave systems merge and only one system is seen. The angles measured from these figures are shown in Fig. 6.18 as a function of τ. The inner wave angle approaches the Kelvin angle as τ approaches zero. The outer wave angle has a maximum around 90 degrees at $\tau = 1/4$ and decreases to the Kelvin angle as τ approaches zero. From Fig. 6.18, the inner-angle of the Point Brower observations corresponds to $1.0 < \tau < 1.5$.

Fig. 6.19 shows contour and isometric plots of the far-field waves generated by a translating and pulsating source-sink pair with nonzero mean strength which may correspond to the surge motion of a ship. The puslation amplitude is the same as the mean value. The reduced frequency is $\tau = 1.0$. An inner-angle wavepacket at about 14 degrees is observed.

Figures 6.20 ($\tau = 1.0$) and 6.21 ($\tau = 2.0$) show the wave patterns corresponding to those in Figs. 6.16 and 6.17, respectively, with the Froude number F_n doubled and the frequency ω halved to keep τ unchanged. The computational domain on the free surface is enlarged by ${F_n}^2$, as explained by (6.25) in the following section. The wave systems with larger bounding angles in Fig. 6.16 and Fig. 6.17 are not visible in Fig. 6.20 and Fig. 6.21 (the wave elevation may be too small to be caught in the contour plots). Again, similar to the nonlinear calculations (Fig. 6.8 and Fig. 6.12), the wave orientations along the wavepackets in Fig. 6.20 and Fig. 6.21 are slightly different from those in Fig. 6.16 and Fig. 6.17 while the packet angles are almost unaffected.

6.3 Wave Patterns by Method of Stationary Phase

The method of stationary phase provides an easy way to determine far-field wave patterns in terms of curves of constant phase. The disturbance can be a ship, a free surface pressure distribution, underwater body or singularity (source-sink pair). In this analysis, the particularity of the disturbance does not affect the establishment of the formulas for determining the phase lines (Yih & Zhu 1989a,b). If the region under consideration is sufficiently far from the disturbance, the wave pattern obtained may be independent of the local disturbance details.

6.3.1 Constant phase lines

The velocity potential $\Phi(\vec{x},t)$ can be expressed as

$$\Phi(\vec{x},t) = Re\{\phi(\vec{x})e^{i\omega t}\}, \tag{6.9}$$

assuming the system is linear and has reached a harmonic limit cycle. Clearly, the spatial function ϕ also satisfies Laplace equation. The linearized free surface boundary condition for Φ in the coordinate system moving with the disturbance is

$$\frac{\partial \Phi}{\partial z} + \left(F_n \frac{\partial}{\partial x} + \frac{\partial}{\partial t}\right)^2 \Phi = 0 \qquad (\text{on } z = 0). \tag{6.10}$$

Substituting (6.9) into (6.10) gives the free surface condition for ϕ,

$$\frac{\partial \phi}{\partial z} + {F_n}^2 \frac{\partial^2 \phi}{\partial x^2} + 2iF_n\omega \frac{\partial \phi}{\partial x} - \omega^2 \phi = 0 \qquad (\text{on } z = 0). \tag{6.11}$$

Separation of variables gives

$$\phi \propto e^{kz} exp\left[i\left(k_x x + k_y y\right)\right] \tag{6.12}$$

where the wavenumber vector is given by

$$(k_x, k_y) = k(\cos\theta, \sin\theta). \tag{6.13}$$

Substitution of (6.13) and (6.12) into (6.11) gives the relation between k and θ,

$$k = (kF_n \cos\theta + \omega)^2. \tag{6.14}$$

Solving (6.14) for k gives

$$k = \frac{1 + 2\tau\cos\theta \pm \sqrt{1 + 4\tau\cos\theta}}{2{F_n}^2 \cos^2\theta}, \tag{6.15}$$

with its first derivative

$$\frac{dk}{d\theta} = k\tan\theta \frac{(\sqrt{1 + 4\tau\cos\theta} \pm 1)}{\sqrt{1 + 4\tau\cos\theta}}, \tag{6.16}$$

where $\tau = F_n\omega$ is the reduced frequency. Since k is real, $1 + 4\tau\cos\theta \geq 0$, the region for θ must be restricted to $0 \leq \theta \leq \theta_o$, where

$$\theta_o = \begin{cases} \pi & \text{if } \tau \leq 0.25 \\ \pi - \cos^{-1}\left(\frac{1}{4\tau}\right) & \text{if } \tau > 0.25 \end{cases}$$

The spatial potential ϕ can then be expressed as

$$\phi(\vec{x}) = \int_0^{\theta_o} d\theta A(\theta) e^{kz} exp\left[i\left(k_x x + k_y y\right)\right], \tag{6.17}$$

where $A(\theta)$ is a function depending on the particular disturbance. The wave elevation $\bar{\eta}(\vec{x}, t)$ has a form similar to Φ,

$$\bar{\eta}(\vec{x}, t) = Re\{\eta(\vec{x}) e^{i\omega t}\}, \tag{6.18}$$

where $\eta(\vec{x})$ has a form similar ϕ (6.17),

$$\eta(\vec{x}) = \int_0^{\theta_o} d\theta B(\theta) e^{i\left(xk_x + yk_y\right)} = \int_0^{\theta_o} d\theta B(\theta) e^{i\, R\psi(\beta,\theta)}, \tag{6.19}$$

and $B(\theta)$ is a function depending on the the particular disturbance, R and β are the polar coordinates of the field point,

$$(x, y) = R(\cos\beta, \sin\beta)$$

and

$$\psi = k(\cos\beta\cos\theta + \sin\beta\sin\theta).$$

Evaluation of (6.17) by the stationary phase method (Copson 1965) gives

$$\eta(R, \beta) \approx \sum_i^M B(\bar{\theta}_i)\left[\frac{\pi}{2R\psi''(\beta, \bar{\theta}_i)}\right]^{1/2} e^{iR\psi(\beta,\bar{\theta}_i) \pm \frac{1}{4}\pi i} + O(\frac{1}{R}), \tag{6.20}$$

where the summation is made over all the stationary points $\bar{\theta}_i$ which are given by

$$\frac{d}{d\theta}\left(R\psi(\beta, \theta)\right) = 0$$

or

$$x\ dk_x + y\ dk_y = 0. \tag{6.21}$$

The "$\pm$" sign in (6.20) is the same as the sign of the second derivative $\psi''(\beta, \bar{\theta}_i)$. For simplicity, the subscript i and the bar over θ are omitted hereafter.

The curve of constant phase can be obtained without the knowledge of $A(\theta)$ and $B(\theta)$. The curve of constant phase C is given by

$$R\psi(\beta, \theta) \pm \frac{\pi}{4} = C$$

or

$$k_x x + k_y y = c \tag{6.22}$$

where $c = C \mp \frac{\pi}{4}$. Solving (6.21) and (6.22) simultaneously for x and y gives

$$(x, y) = \frac{c\ (dk_y, -dk_x)}{k_x\ dk_y - k_y\ dk_x} \tag{6.23}$$

With the use of (6.13), (6.23) becomes

$$(x, y) = \frac{c}{k^2}\left(k\cos\theta + \frac{dk}{d\theta}\sin\theta\ , k\sin\theta - \frac{dk}{d\theta}\cos\theta\right). \tag{6.24}$$

Substituting (6.15) and (6.16) into (6.24) gives the parametric equations for the curves of constant c,

$$\frac{(x, y)}{{F_n}^2} = \frac{2c\left[(\pm\sin^2\theta + \sqrt{1 + 4\tau\cos\theta})\cos\theta,\ \mp\sin\theta\cos^2\theta\right]}{(1 + 2\tau\cos\theta \pm \sqrt{1 + 4\tau\cos\theta})\sqrt{1 + 4\tau\cos\theta}}\ . \tag{6.25}$$

Choosing values of c separated by 2π gives a set of phase lines separated by one wavelength. Equation (6.25) shows that the stet of the constant phase lines are Froude number independent as expected since there is no physical length scale involved in this analysis. Therefore, we set F_r to be unity.

The sign of c must be properly chosen to satisfy the radiation conditions (lines of constant phase do not extend to $x \to -\infty$). At the first glance, there seems to be two sets of constant phase lines since (6.14) has two roots for k. By carefully examining (6.25), we find that (6.25) using positive c and the "+" sign satisfies the radiation condition for $0° \leq \theta \leq 90°$ but not for $90° < \theta < \theta_o$. The phase c must change sign for $90° < \theta < \theta_o$. So (6.25) using the "+" set gives two systems of phase lines. For the "−" sign in (6.25), c must be positive so that the radiation condition is satisfied. Equation (6.25) using "−" gives only one system of constant phase lines.

Figures 6.22 to 6.29 show lines of constant phase C for several values of τ. Each figure, for a given $\tau > 0$, contains three distinct systems of waves similar to those in Noblesse & Hendrix (1990) using a different approach. For $\tau = 0$ (steady waves), the "−" set of the constant phase lines disappear (the wavelength becomes infinitely large), while the first and second systems of the phase lines become identical to the normal Kelvin wave pattern. The first system is very similar to the Kelvin wave pattern which consists of transverse waves and diverging waves and has a cusp line whose angle is less than the Kelvin angle 19.5°. The second system also consists of transverse waves and diverging waves for $\tau < 0.25$ with a cusp line of a larger angle than 19.5°. For $\tau > 0.25$ the transverse waves disappear. The third system has ring-type waves for $\tau < 0.25$. For $\tau > 0.25$, part of the ring-type waves become diverging waves.

A line of constant phase C is disconnected at the cusp line of a wave system since the constant c has a jump of $\pi/2$ across the point. This is because the second derivative of ψ, ψ'', changes its sign across the point, which will be explained in more detail in the following sections. Because of this jump, the crests (or trough) of the

transverse waves and the crests (or trough) of the diverging waves do not meet on the cusp line. The phase lines shown in Noblesse & Hendrix (1990) correspond to the lines of constant c in our case where the lines should be continuous.

6.3.2 Bounding angles for constant phase lines

From (6.25), we have, for the first and second systems,

$$\frac{|y|}{x} = f_{1,2}\frac{|c|}{c}\frac{\sin\theta\cos\theta}{\sin^2\theta + \sqrt{1+4\tau\cos\theta}}, \tag{6.26}$$

where

$$f_{1,2} = \frac{1+2\tau\cos\theta+\sqrt{1+4\tau\cos\theta}}{\left|1+2\tau\cos\theta+\sqrt{1+4\tau\cos\theta}\right|}$$

and for the third system,

$$\frac{|y|}{x} = -f_3\frac{|c|}{c}\frac{\sin\theta\cos\theta}{\sin^2\theta - \sqrt{1+4\tau\cos\theta}}, \tag{6.27}$$

where

$$f_3 = \frac{1+2\tau\cos\theta-\sqrt{1+4\tau\cos\theta}}{\left|1+2\tau\cos\theta-\sqrt{1+4\tau\cos\theta}\right|}$$

Equation (6.26) is plotted in Fig. 6.30 for various values of τ. The curves for $0° < \theta < 90°$ correspond to the first system of phase lines and $\theta > 90°$ corresponds to the second system of phase lines as explained above. The third system (6.27) is plotted in Fig. 6.31 for various values of τ.

The bounding angle for each system can be determined from Fig. 6.30 and Fig. 6.31 or from (6.26) and (6.27) or (6.25) directly. The maximum of $|y|/x$ of each system gives the bounding angle $\alpha = \tan^{-1}(|y|/x)$. For the first system, $0° < \theta < 90°$ in Fig. 6.30, $|y|/x$ has one maximum which is also a local maximum (*i.e.* the derivative of $|y|/x$ is zero). For the second system, $90° < \theta < \theta_o$ in Fig. 6.30, $|y|/x$ also

has one maximum which, however, is not a local maximum when $\tau > 1/4$. For the third system, Fig. 6.31, $|y|/x$ can have a maximum of $\pm\infty$ for τ less than a certain value. $|y|/x$ has a jump from ∞ to $-\infty$ (or $-\infty$ to ∞) across an angle θ_c which is the root of $\sin^2\theta - \sqrt{1+4\tau\cos\theta} = 0$. The infinity of $|y|/x$ does not correspond to the angle of the bounding line. The angle of the bounding line in this system only comes from the local maximum of $|y|/x$ where the derivative of $|y|/x$ is zero. Fig. 6.32 shows $\tan^{-1}(|y|/x)$ as a function of θ for the third system. From Fig. 6.32, it is easier to determine the angle of the bounding line by finding the global maximum of $\tan^{-1}(|y|/x)$.

Fig. 6.33 shows the bounding angles of the three systems (denoted by α_1, α_2 and α_3 respectively) as a function of τ. α_1 is a continuous function of τ. α_2 has a jump from 54.74° to 90° and α_3 has a jump from 180° to 126.26° when τ changes from 0.25− to 0.25+. Fig. 6.33 is convenient to determine the angles of the inner-angle wavepackets. Fig. 6.30 and Fig. 6.31 help estimate the decay rates of the waves.

6.3.3 Decay rates of waves

The wave decay rate for large R can be estimated by applying the method of stationary phase to (6.19) without knowing $B(\theta)$ (Copson 1965). The decay rate is closely related to the second derivative of ψ (corresponding to the first derivative of $|y|/x$, Newman 1977). Fig. 6.30 and Fig. 6.31 are helpful since they provide the information about the derivative of $|y|/x$.

- Along β, in which $\beta \neq \alpha_i$ and $\beta < max(\alpha_i)$, $i = 1,2,3$, the wave elevation is given by (6.20) since the second derivative of ψ (corresponding to the first

derivative of $|y|/x$, Newman 1977) does not vanish at the stationary points. The waves decay at a rate of $R^{-1/2}$. For simplicity, we express this decay as

$$\eta(R,\beta) \propto \frac{1}{R^{1/2}} + O(\frac{1}{R}). \tag{6.28}$$

- If β is greater than $\max(\alpha_i)$, there are no stationary points and the waves decay faster,

$$\eta(R,\beta) \propto \frac{1}{R} + O(\frac{1}{R^2}). \tag{6.29}$$

- The decay rates along the bounding angles of the wave systems are as follows:

  - Along $\beta = \alpha_1$, for all τ, ψ'' is zero for the first wave system at the stationary point while ψ'' is not zero for the other two wave systems. The contribution from the first system dominates and decays as $R^{-1/3}$, while the contributions from the other two systems decay as $R^{-1/2}$. Therefore, the decay rate along $\beta = \alpha_1$ is

$$\eta(R,\beta) \propto \frac{1}{R^{1/3}} + O(\frac{1}{R^{1/2}}). \tag{6.30}$$

  - Along $\beta = \alpha_2$, ψ'' is zero for the second system at the stationary point only when $\tau < 0.25$. When $\tau \geq 0.25$, ψ'' is not zero. Also, ψ'' is also not zero for the other two systems for all τ. Therefore, the decay rate along α_2 is

$$\eta(R,\beta) \propto \begin{cases} \frac{1}{R^{1/3}} + O(\frac{1}{R^{1/2}}) & \text{if } \tau < 0.25 \\ \\ \frac{1}{R^{1/2}} + O(\frac{1}{R}) & \text{if } \tau \geq 0.25. \end{cases}$$

  - Along $\beta = \alpha_3$, ψ'' is zero for the third system for $\tau > 0.25$. ψ'' is not zero for the other two wave systems for all τ. Therefore, the waves decay as

$$\eta(R,\beta) \propto \begin{cases} \frac{1}{R^{1/3}} + O(\frac{1}{R}) & \text{if } \tau > 0.25 \\ \\ \frac{1}{R^{1/2}} + O(\frac{1}{R}) & \text{if } \tau \leq 0.25. \end{cases}$$

6.4 Comparisons and Discussions

We now compare the results of the nonlinear and linear calculations as well as the stationary phase analysis, and steady waves to unsteady waves.

Fig. 6.34 shows the contour plot of the waves generated by the same source-sink pair used in Fig. 6.1 to simulate the cutter Point Brower using the linear calculation. Both the nonlinear (Fig. 6.1) and linear (Fig. 6.34) calculations show same interference between the wave system caused by the source and that caused by the sink. The interference is not clearly separated from the Kelvin diverging waves. Fig. 6.35 and Fig. 6.36 show results of the linear and nonlinear wave calculations for the same source-sink pair used in Fig. 6.1 and Fig. 6.34. Here the pair not only translates but also heaves about the mean submergence depth used for Fig. 6.1. We use a heave amplitude of 25% of the mean depth and a reduced frequency $\tau = 0.5$ although the information on the motion of the cutter is not known. An inner-angle wavepacket is seen separated from the Kelvin diverging waves at an angle between 13.5° and 14.5° in both linear and nonlinear calculations. The wavepacket by the nonlinear calculation seems more isolated.

Three wave systems are identified in the stationary phase analysis. However, the phase lines do not give the quantitative information about the wave elevation. To

calculate the wave elevation, it is necessary to know $A(\theta)$, or $B(\theta)$, which depends on the particular disturbance. It is possible that one may not be able to identify all the three wave systems in the isometric and contour plots of the wave elevation. At low frequency, we see the first and second systems in the plots of the linear and nonlinear waves. The third system is not seen most likely because it has a large wavelength, a small amplitude, or is outside the computational window. At an intermediate frequency, the third system can be identified while it is difficult to distinguish the second system from the first system because the bounding lines of the two systems are close and the waves interact. At high frequency, the second system has very short wavelengths, finer than our computational grids can resolve. We can see the third system or the combination of the first and third systems but it is difficult to distinguish them from the plots of wave elevation. Fig. 6.37 shows a contour plot of wave elevation due to a translating pulsating source-sink pair with a zero-mean strength and $\tau = 1.0$ using the linear calculation. The corresponding constant phase lines are overlayed on the contour lines. The agreements in the wavelength, wave orientations, and the phase in the inner region and outer region are fairly good.

Figures 6.38 to 6.42 show the wave elevation (shown by darkness of color) due to the same source-sink pair used in Fig. 6.37 but with $\tau = 0.5$ at five different times within an oscillation cycle, beginning at time $t = 12.0$ when the pair has traveled 18 ship lengths. The period of the cycle is $100\Delta t$ where $\Delta t = 0.02$ is the time step used in the calculation. As can be seen, the initial transient effects have died out and the waves have almost achieved the limit cycle since Fig. 6.38 and Fig. 6.42 are nearly identical. To examine how these unsteady waves move, the wave elevation within one cycle along the symmetry plane and the ray of the inner-angle wavepacket of 14 degrees is shown in Fig. 43 and Fig. 44 respectively (the wave motions can be

seen more clearly from the animation of the waves). In Fig. 43 and Fig. 44, R is the distance from the center of the source-sink pair. As expected, the transverse waves (Fig. 6.43) radiate from the disturbance. The waves along the line of 14° (Fig. 6.44) also radiate from the disturbance but with a fluctuation at lower frequency. The animation clearly shows that the inner-angle wavepacket originates from the disturbance and moves away from it. The wavepacket fluctuates along the 14° line, which agrees with the observed sinuous fluctuation along the "solitary" feature in the wake of the cutter Point Brower (Brown *et al.* 1989). The animation also shows that there are long crest waves moving away from the wavepacket periodically. As a wave (*e.g.*, a wave crest) in the wavepacket moves along the 14° line, half of it merges into a long crest wave and the other half keeps moving along the wavepacket.

From Fig. 6.43 and Fig. 6.44, it can be seen that the wave amplitude along the wavepacket is larger and decays at a slower rate than that along the symmetry plane. Moreover, Fig. 6.45 shows the peak wave amplitude within the diverging wave system of the steady wake by the nonlinear calculation shown in Fig. 6.1. The peak wave amplitude at a distance x is obtained by searching the maximum wave amplitude in the y direction within the diverging wave region ($15° < \beta < 19.5°$). Fig. 6.46 shows the peak wave amplitude within the region ($10° < \beta < 15°$) of the interference between the bow and stern wave systems in Fig. 6.1. Fig. 6.47 and Fig. 6.48 show the peak wave amplitudes within the diverging wave region ($15° < \beta < 19.5°$) and interference region ($10° < \beta < 15°$) for the steady wake by the linear calculation shown in Fig. 6.34. Fig. 6.49 shows the peak amplitudes at three different times within the the inner-angle wavepacket region ($10° < \beta < 15°$) in the unsteady wake by the nonlinear calculation shown in Fig. 6.36. Fig. 6.50 shows the the peak amplitudes at the five different times in one oscillation cycle within the the inner-

angle wavepacket region in the unsteady wake by the linear calculation shown in figures 6.38 to 6.42.

The upper envelope of the amplitude in each figures (figures 6.45 to 6.50) gives the decay rate of the wavepacket amplitude. A straight line showing the algebraic decay rate by the stationary phase analysis is drawn at the upper bound of the peak amplitude in each figures. As seen from these figures, for the steady wake, the waves by both nonlinear and linear calculations decay at a rate close to $O(R^{-1/3})$ within the diverging wave region while at $O(R^{-1/2})$ within the interference region in the steady wake. This is consistent with the results of the normal steady Kelvin wake theory (Ursell 1960). For the unsteady wake, the waves by both nonlinear and linear calculations decay at a rate close to $O(R^{-1/3})$ within the inner-angle wavepacket, which is consistent with the result of the stationary phase analysis in this thesis. The experimental data of Brown *et al.* (1989) are also redrawn in Fig. 6.51 to show the algebraic decay of the peak amplitude. The observed decay rate (Fig. 6.51) is closer to $O(R^{-1/3})$ of the unsteady inner-angle wavepacket. Brown *et al.* (1989) compare the experimental data to the $O(R^{-1/2})$ decay of a steady linear Kelvin wake theory to draw the conclusion that nonlinear effects play an important role in the generation of the inner-angle wavepacket.

6.5 Conclusions

Our study shows that nonlinear effects are not necessary for the generation of inner-angle wavepackets; unsteady effects can cause the inner-angle waves. The observed inner-angle of 10.8 degrees in the full scale measurement on the cutter Point Brower may correspond to a ship motion at a reduced frequency within $1.0 < \tau < 1.5$. In the unsteady wake, the wave amplitude decays as $O(x^{-1/3})$ along the ray of the

inner packet, the same rate at which the normal steady Kelvin wave decays along its cusp line (Ursell 1960). Hence, it appears that the persistence of the inner-angle wavepacket behind the ship can be explained by unsteady linear wave theory alone. Our study also shows that waves can be confined in a very narrow region if the frequency is very high. Therefore, the high frequency propeller-induced unsteady flow may also contribute to the very narrow V structure in the wake.

The Froude number, based on the pressure patch length in our nonlinear calculations or the submergence depth of the source-sink pair in our linear wave calculations, affects the wave orientation in relation to the wavepacket without affecting the wavepacket angles if the reduced frequency remains unchanged.

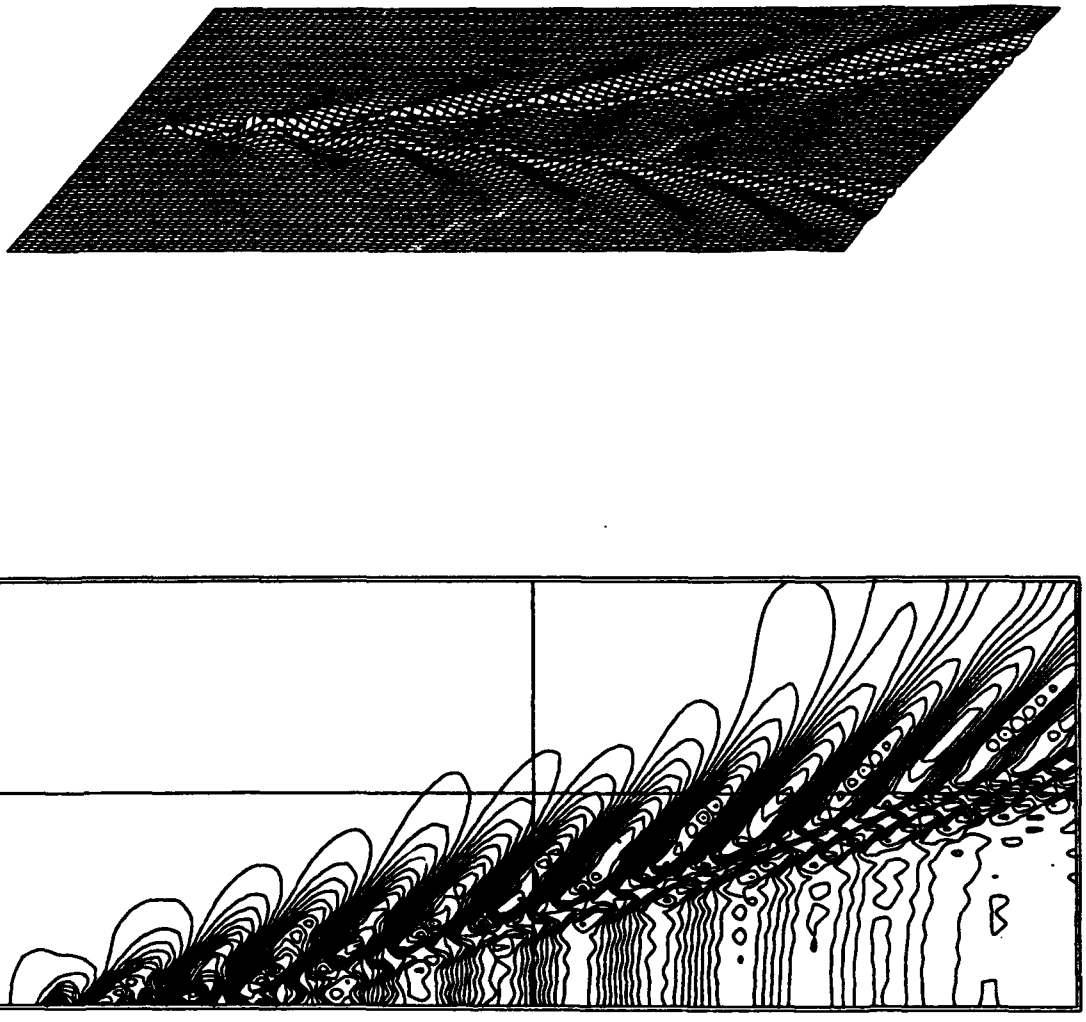


Figure 6.1: Nonlinear waves by a translating, non-oscillating source-sink pair, F_n=0.49, free surface domain: $(0 \leq x \leq 11,\ 0 \leq y \leq 4.5)$ Contour lines are apart by 0.005

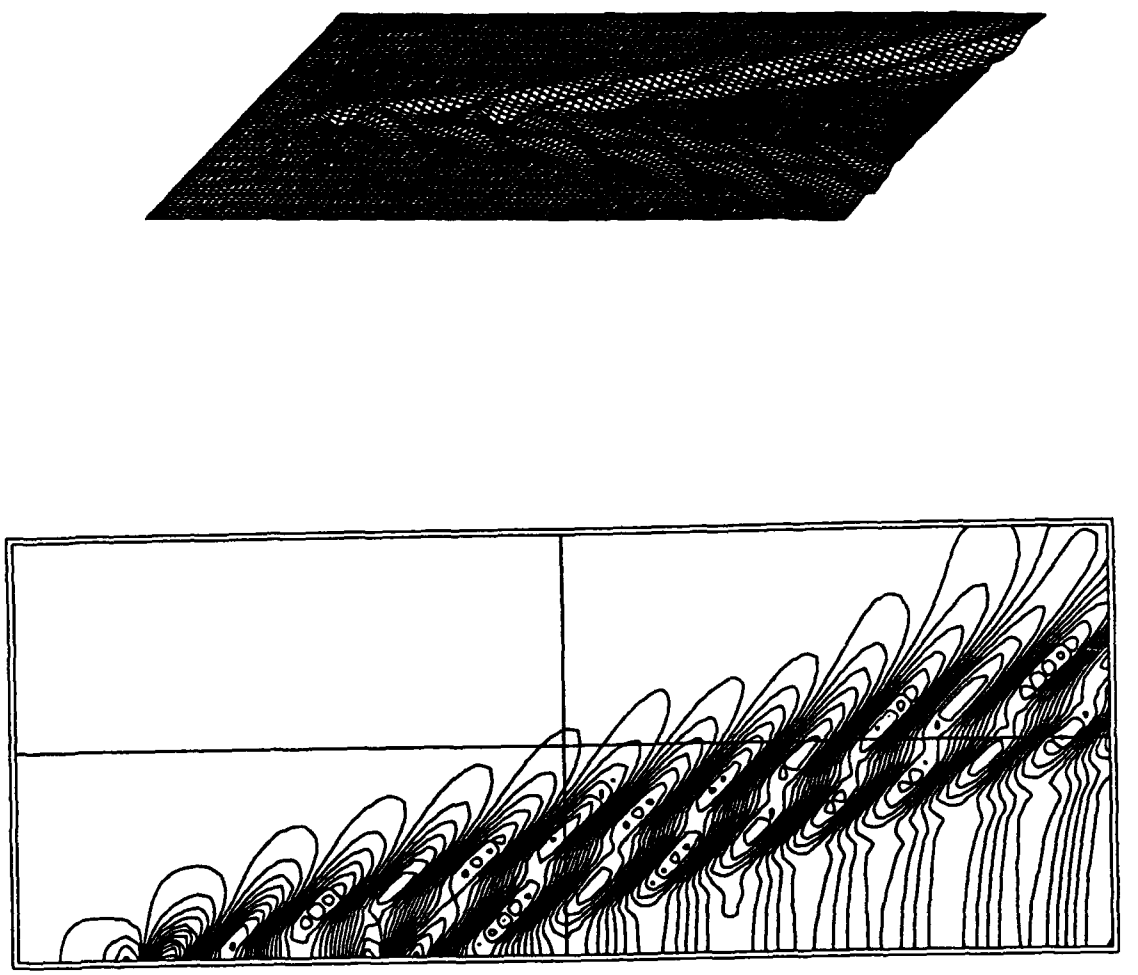


Figure 6.2: Nonlinear waves by two translating, non-oscillating dipoles, F_n=1.0, free surface domain:($0 \leq x \leq 4.5 \quad 0 \leq y \leq 1.8$), Contour lines are apart by 0.001

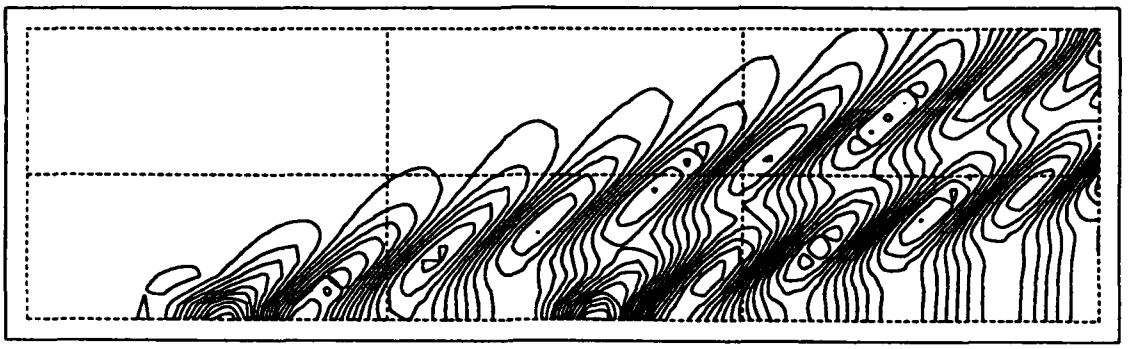


Figure 6.3: Nonlinear waves by two translating, non-oscillating surface pressure patches (weak disturbance), Contour lines are apart by 0.0002
$(0 \leq x \leq 5.2, 0 \leq y \leq 1.6)$

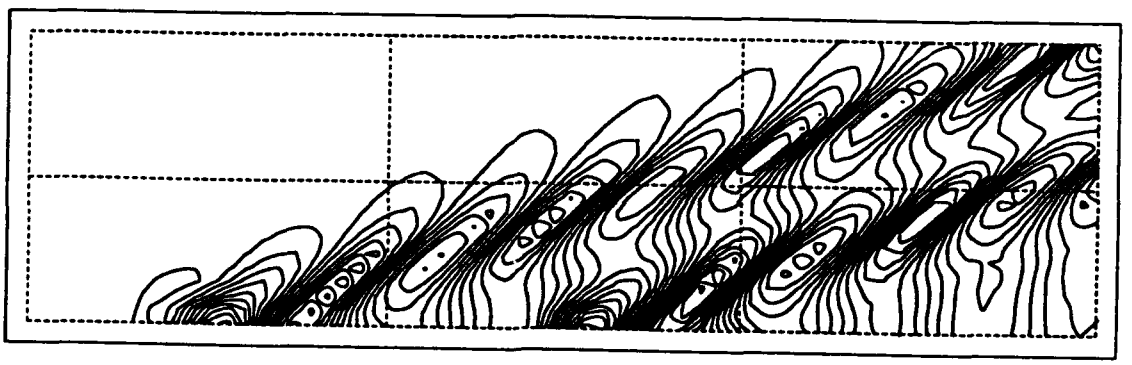


Figure 6.4: Nonlinear waves by two translating, non-oscillating surface pressure patches (strong disturbance), Contour lines are apart by 0.004)
$(0 \leq x \leq 5.2, 0 \leq y \leq 1.6)$

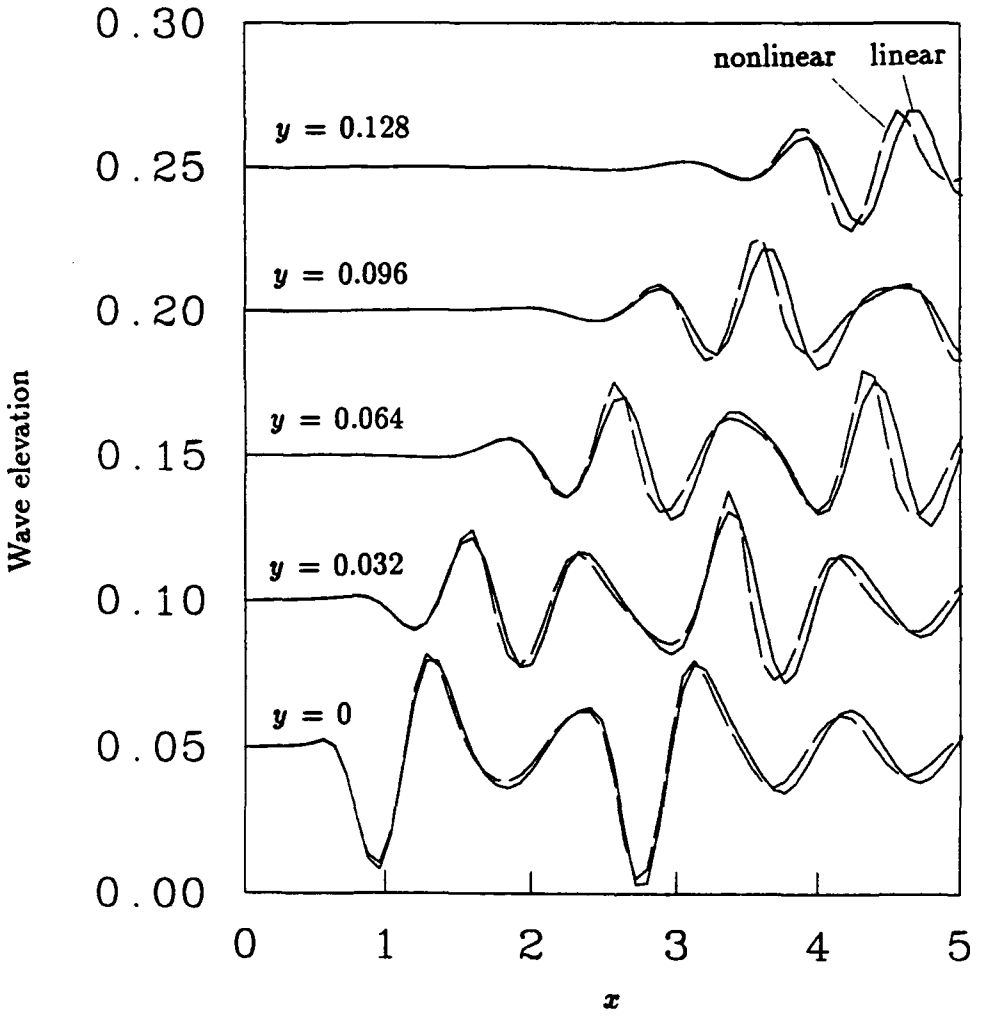


Figure 6.5: Comparison of Nonlinear waves to "linear" waves by two translating, non-oscillating surface pressure patches (strong disturbance)

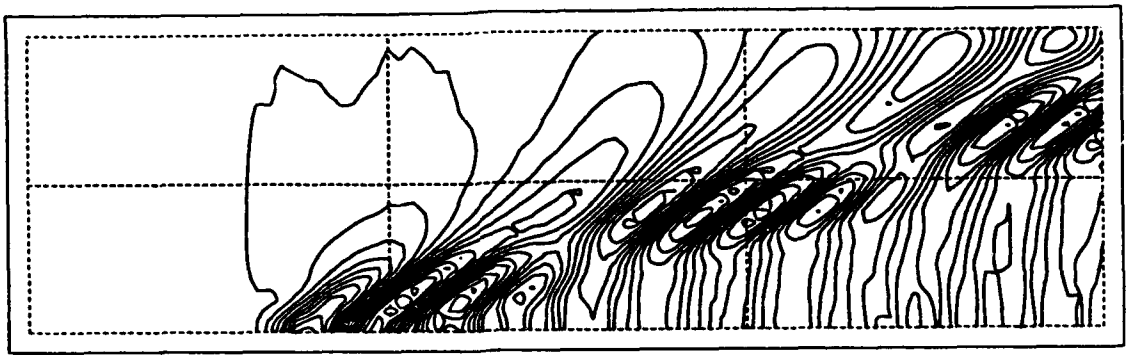


Figure 6.6: Nonlinear waves by a translating and oscillating surface pressure patch with zero mean. ($\tau = 0.25$, $F_n = 0.4$), Contour lines are apart by 0.0001 ($0 \leq x \leq 5.2, 0 \leq y \leq 1.6$)



Figure 6.7: Nonlinear waves by a translating and oscillating surface pressure patch with zero mean. ($\tau = 0.5$, $F_n = 0.4$), Contour lines are apart by 0.0001 ($0 \leq x \leq 5.2, 0 \leq y \leq 1.6$)

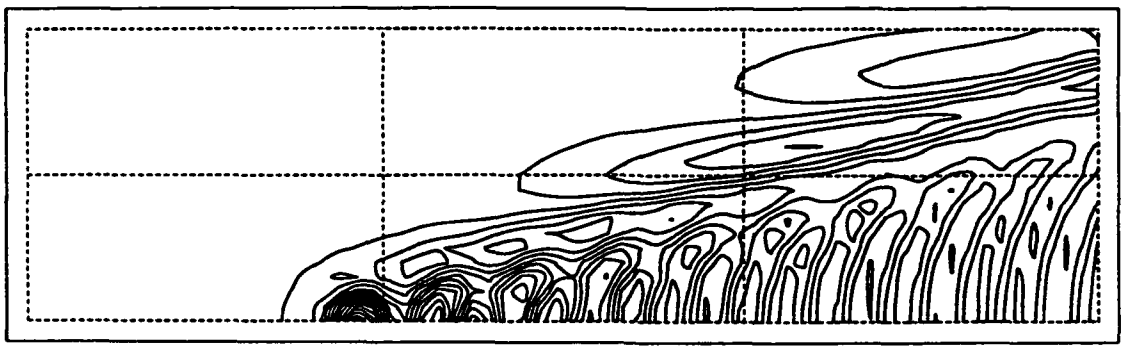


Figure 6.8: Nonlinear waves by a translating and oscillating surface pressure patch with zero mean. ($\tau = 1.0$, $F_n = 0.4$), Contour lines are apart by 0.0001 ($0 \leq x \leq 5.2, 0 \leq y \leq 1.6$)

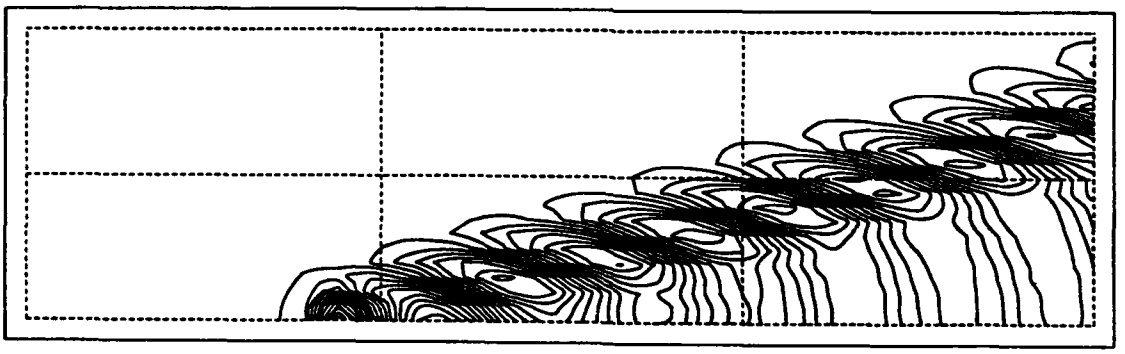


Figure 6.9: Nonlinear waves by a translating and oscillating surface pressure patch with zero mean. ($\tau = 2.0$, $F_n = 0.4$), Contour lines are apart by 0.00005 ($0 \leq x \leq 5.2, 0 \leq y \leq 1.6$)

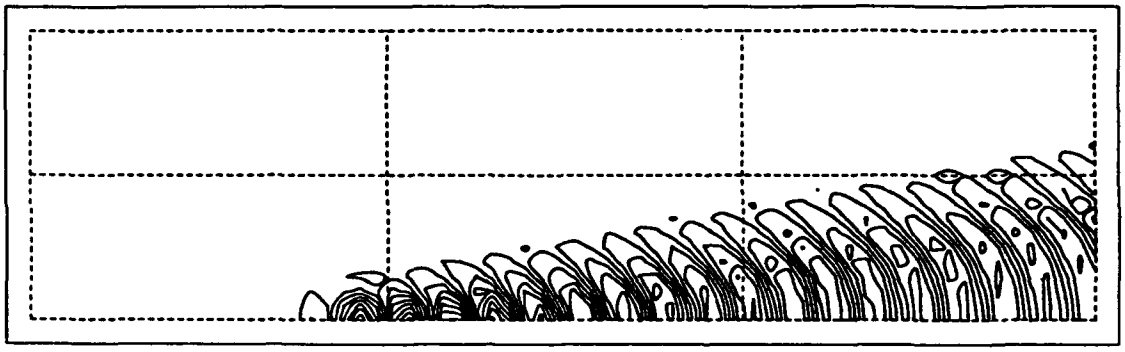


Figure 6.10: Nonlinear waves by a translating and oscillating surface pressure patch with zero mean. ($\tau = 4.0$, $F_n = 0.4$), Contour lines are apart by 0.00005 ($0 \leq x \leq 5.2, 0 \leq y \leq 1.6$)

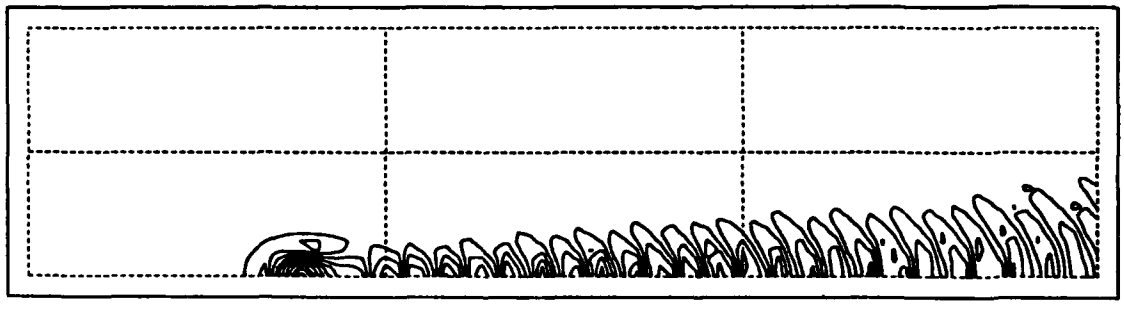


Figure 6.11: Nonlinear waves by a translating and oscillating surface pressure patch with zero mean. ($\tau = 6.0$, $F_n = 0.4$), Contour lines are apart by 0.00001 ($0 \leq x \leq 5.2, 0 \leq y \leq 1.6$)

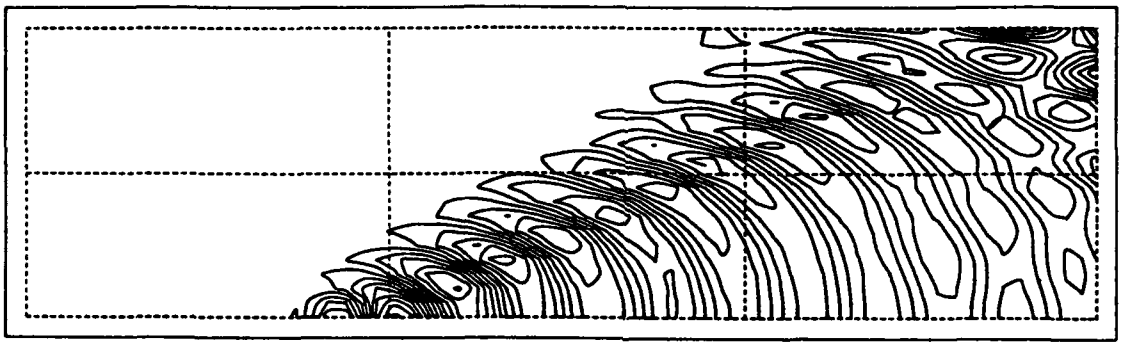


Figure 6.12: Nonlinear waves by a translating and oscillating surface pressure patch with zero mean. ($\tau = 1.0$, $F_n = 0.2$), Contour lines are apart by 0.0001 ($0 \leq x \leq 5.2, 0 \leq y \leq 1.6$)

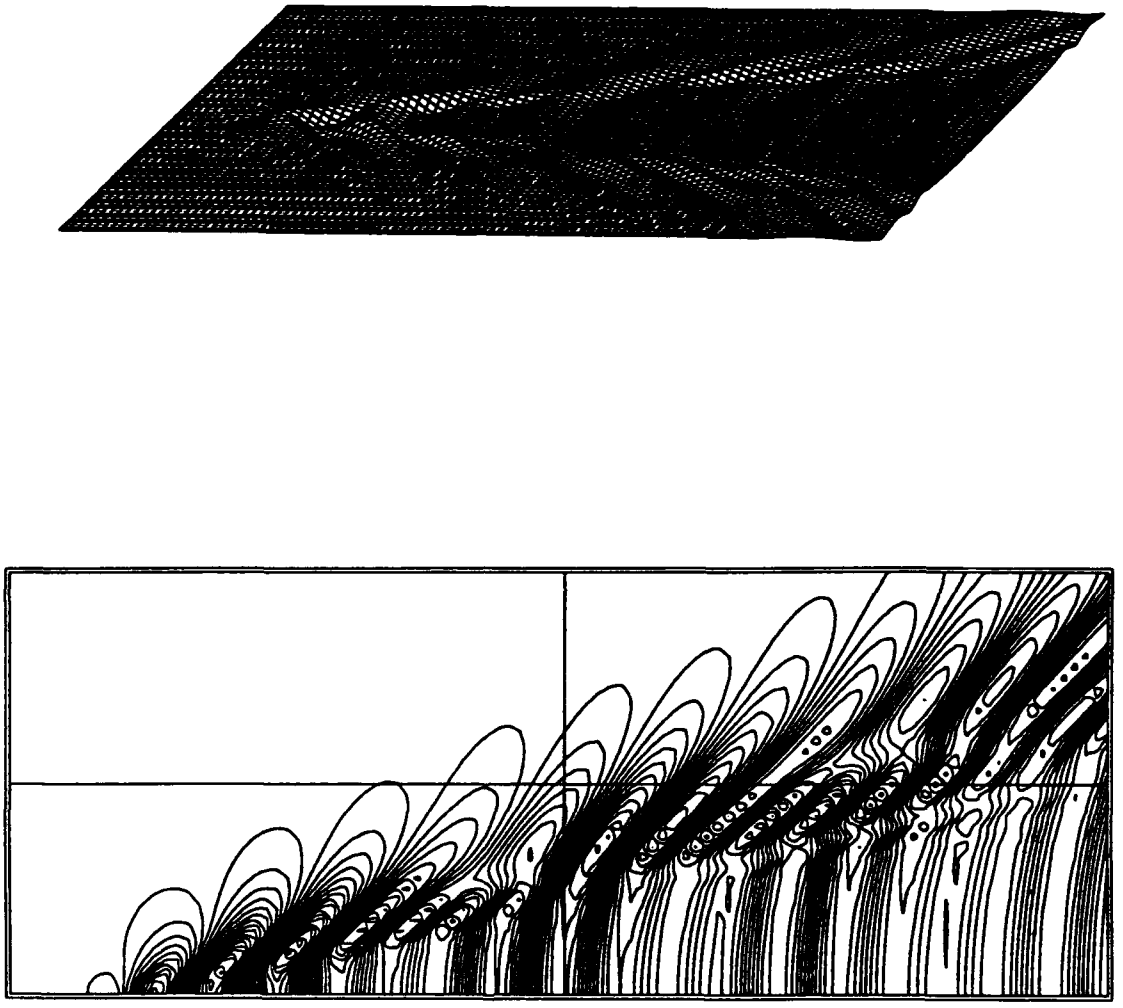


Figure 6.13: Linear waves by a translating and oscillating source-sink pair with zero-mean strength. ($\tau = 0.125$) $(0 \leq x \leq 11, 0 \leq y \leq 4.5)$

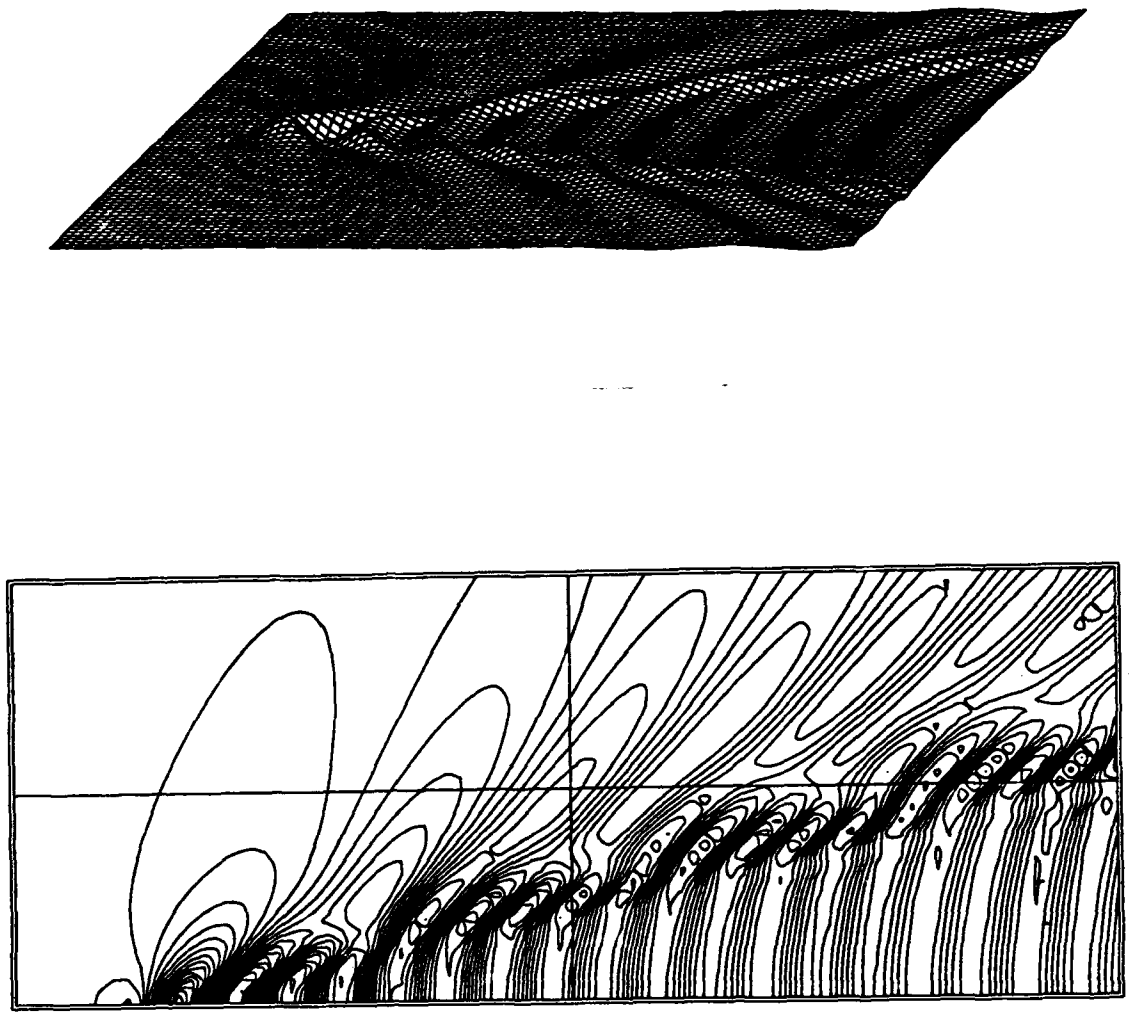


Figure 6.14: Linear waves by a translating and oscillating source-sink pair with zero-mean strength. ($\tau = 0.25$) ($0 \leq x \leq 11, 0 \leq y \leq 4.5$)

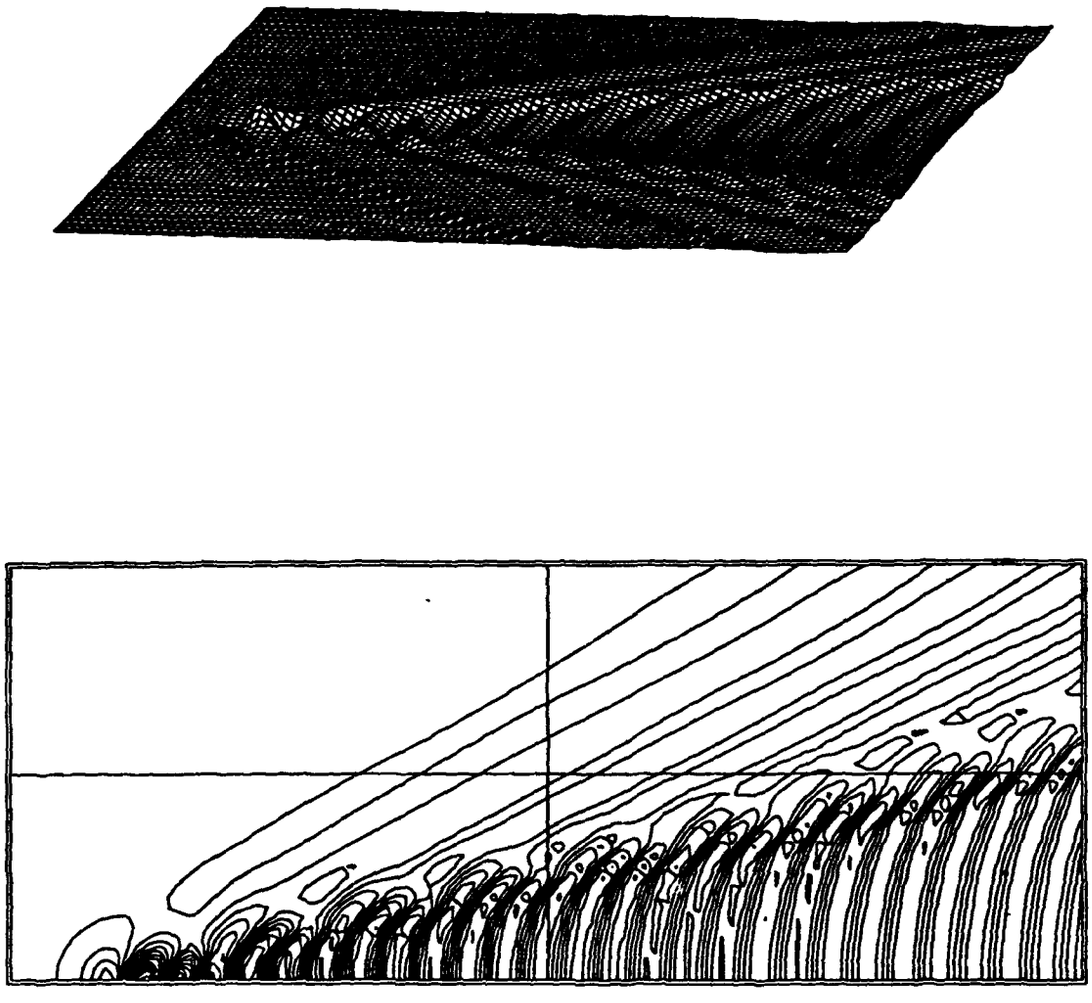


Figure 6.15: Linear waves by a translating and oscillating source-sink pair with zero-mean strength. ($\tau = 0.5$) ($0 \leq x \leq 11, 0 \leq y \leq 4.5$)

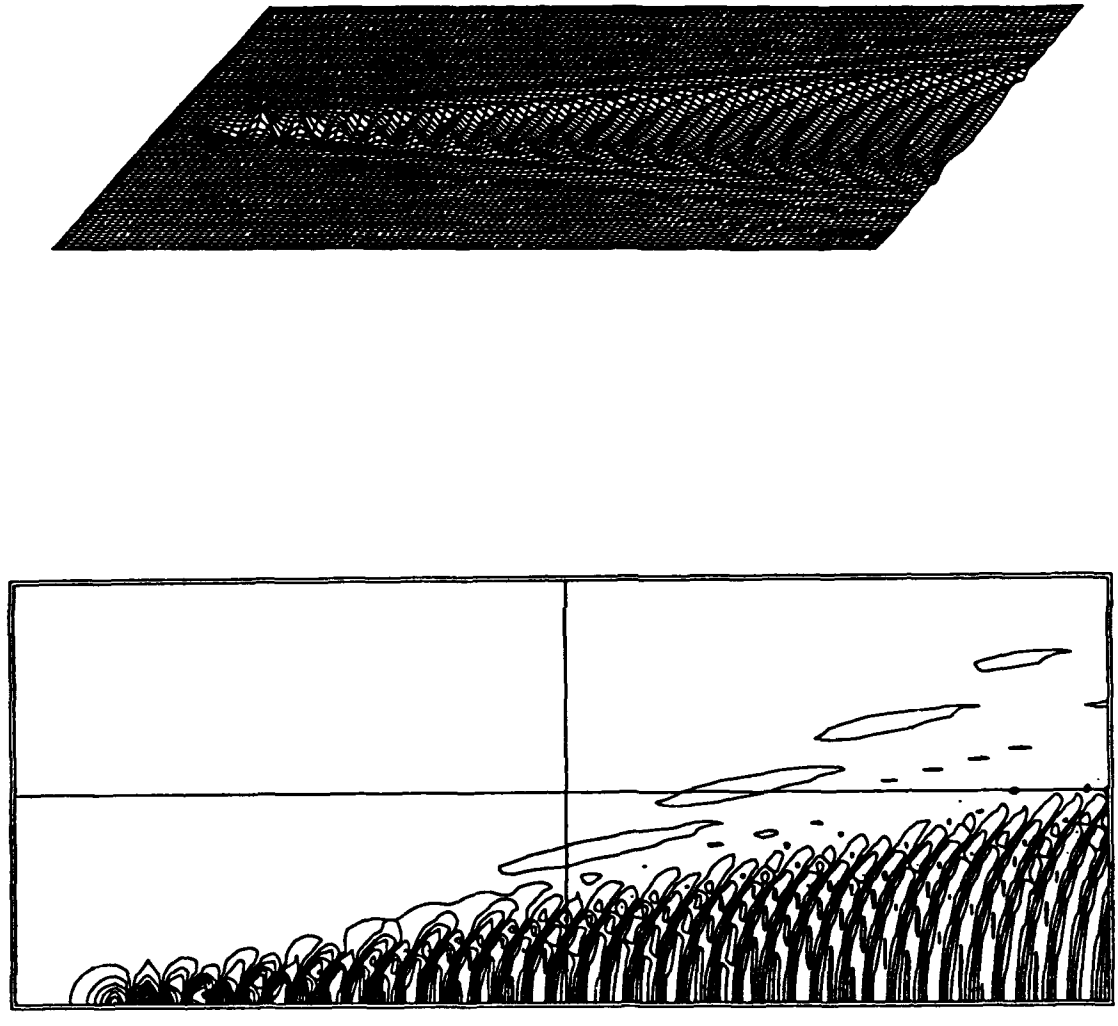


Figure 6.16: Linear waves by a translating and oscillating source-sink pair with zero-mean strength. ($\tau = 1.0$) $(0 \leq x \leq 11, 0 \leq y \leq 4.5)$

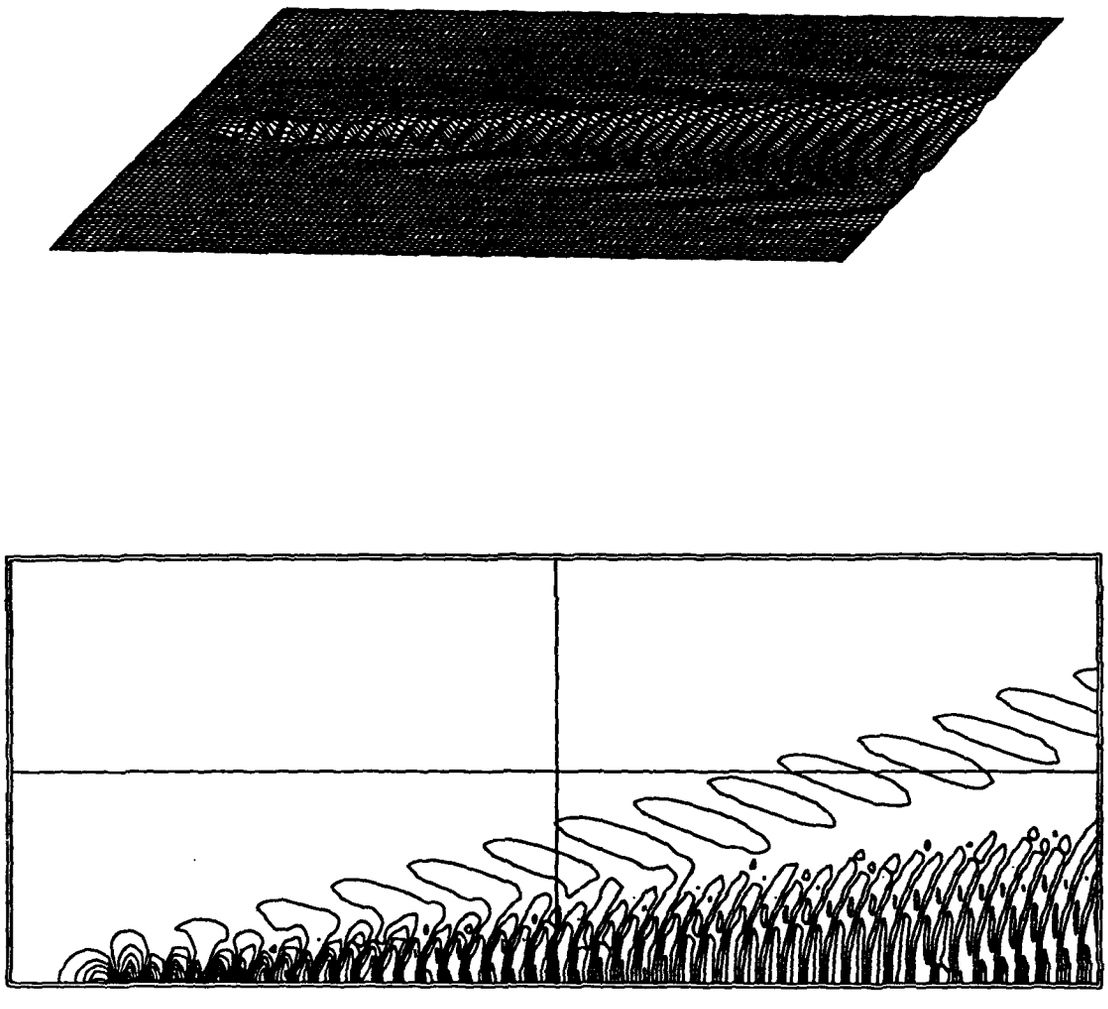


Figure 6.17: Linear waves by a translating and oscillating source-sink pair with zero-mean strength. ($\tau = 2.0$) ($0 \leq x \leq 11, 0 \leq y \leq 4.5$)

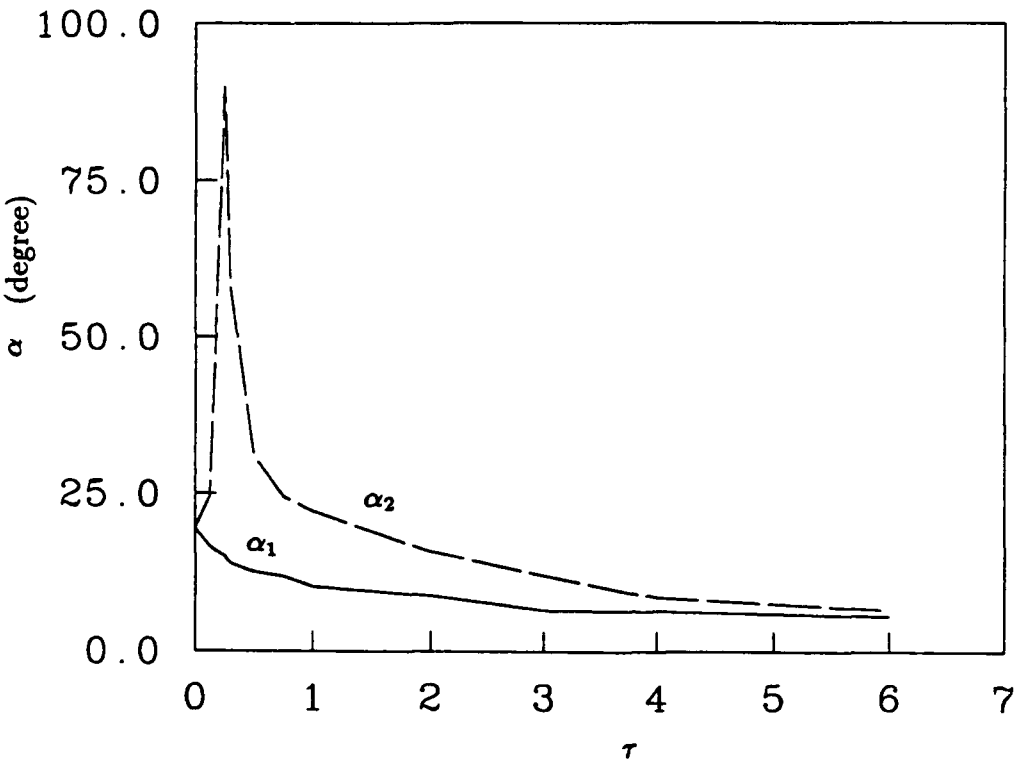


Figure 6.18: Bounding-line angles *vs* τ (by linear wave calculations using time-domain Green function

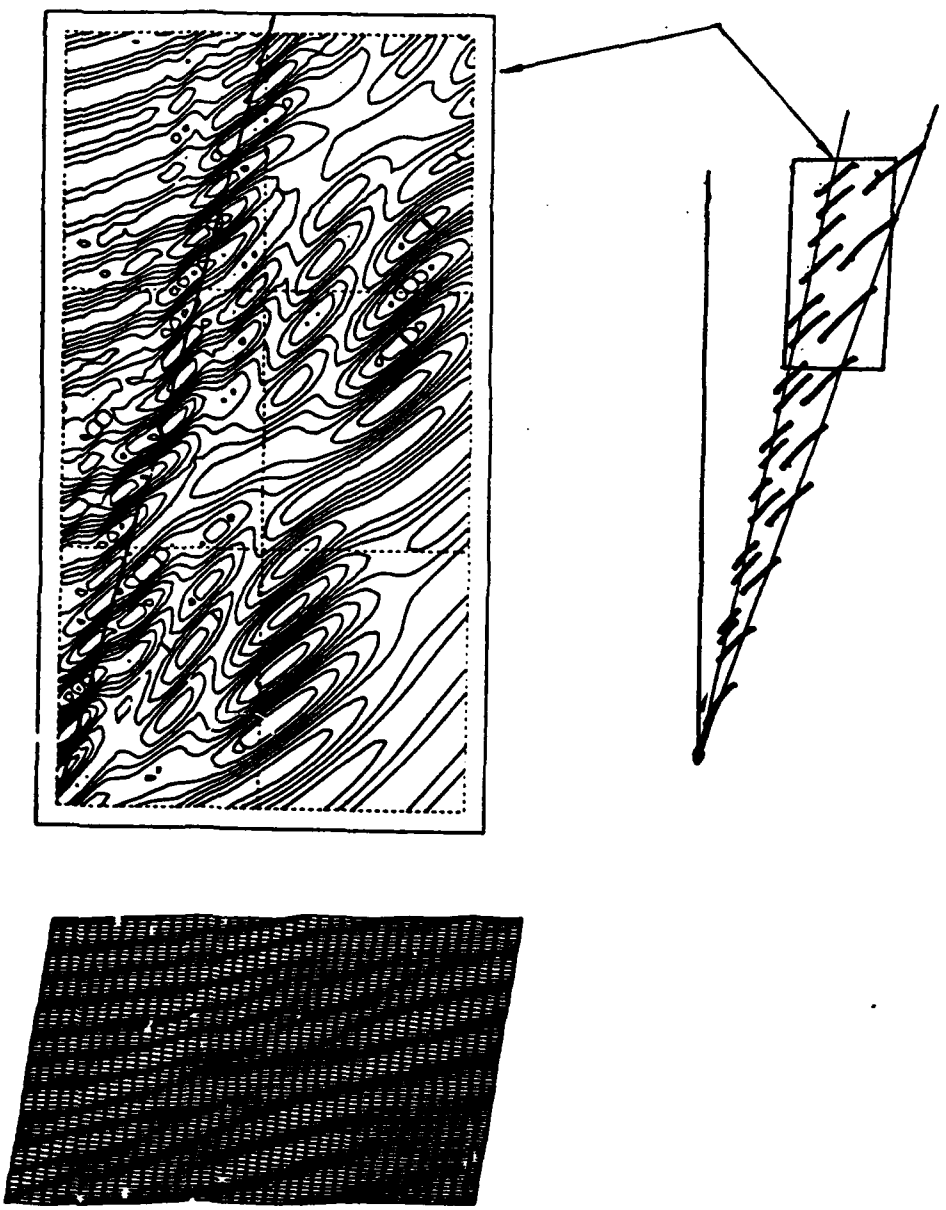


Figure 6.19: Far field linear waves by a translating and oscillating source-sink pair with non-zero-mean strength. ($\tau = 1.0$)

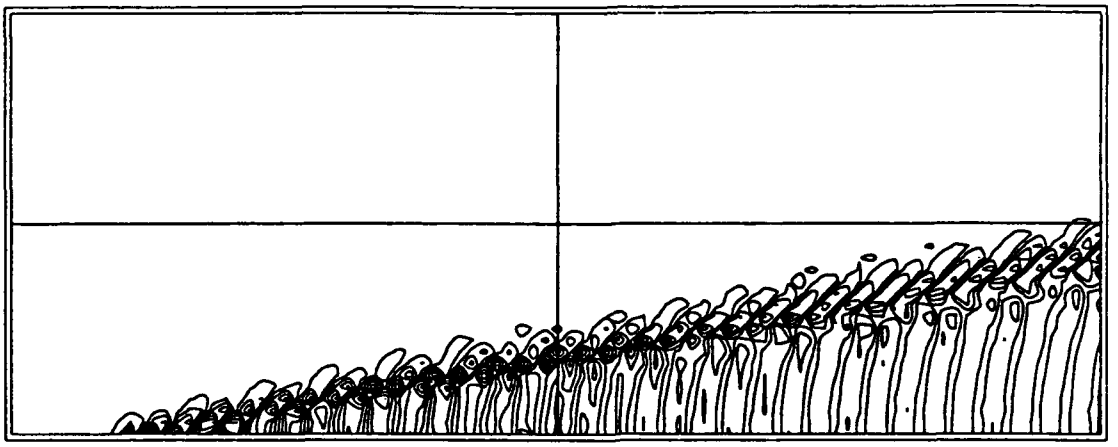


Figure 6.20: Linear waves by a translating and oscillating source-sink pair with zero-mean strength. ($F_n = 2$ and $\tau = 1.0$) $(0 \leq x \leq 11, 0 \leq y \leq 4.5)$

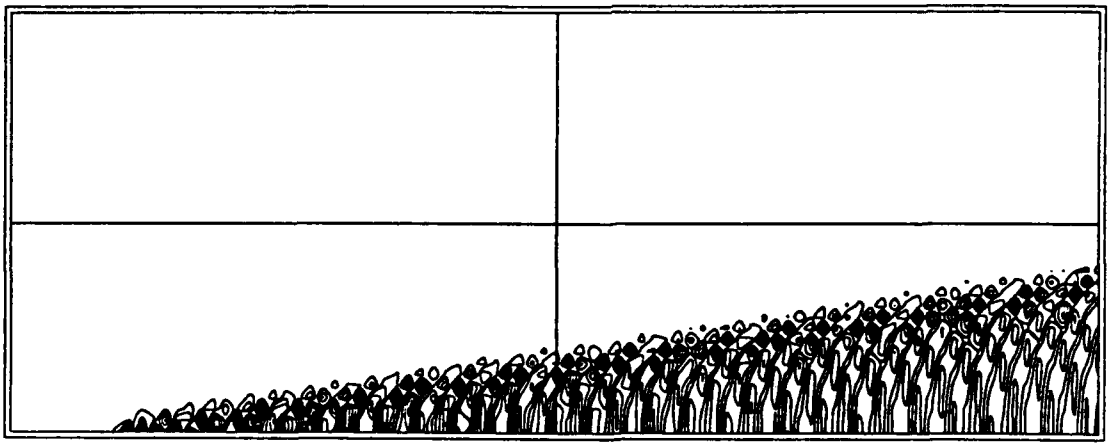


Figure 6.21: Linear waves by a translating and oscillating source-sink pair with zero-mean strength. ($F_n = 2$ and $\tau = 2.0$) $(0 \leq x \leq 11, 0 \leq y \leq 4.5)$

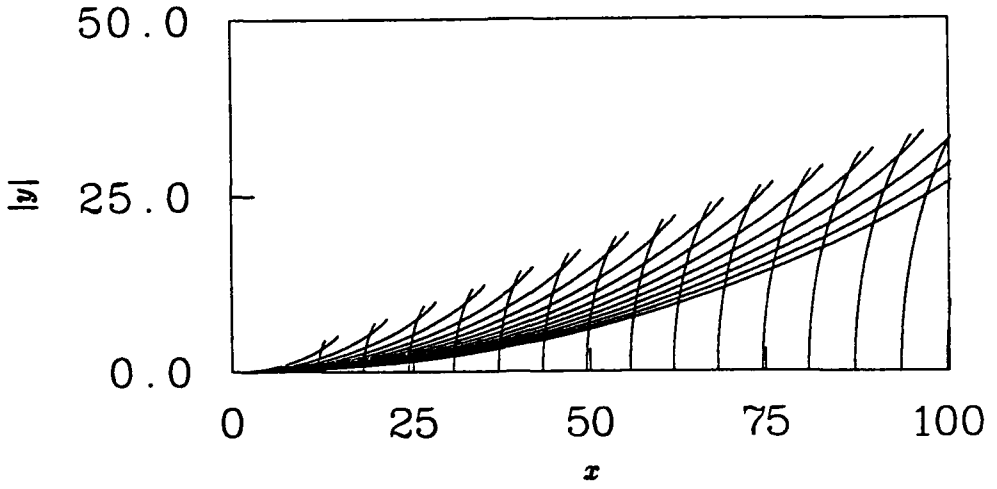


Figure 6.22: Constant phase lines of Kelvin wake,$\tau = 0.0$

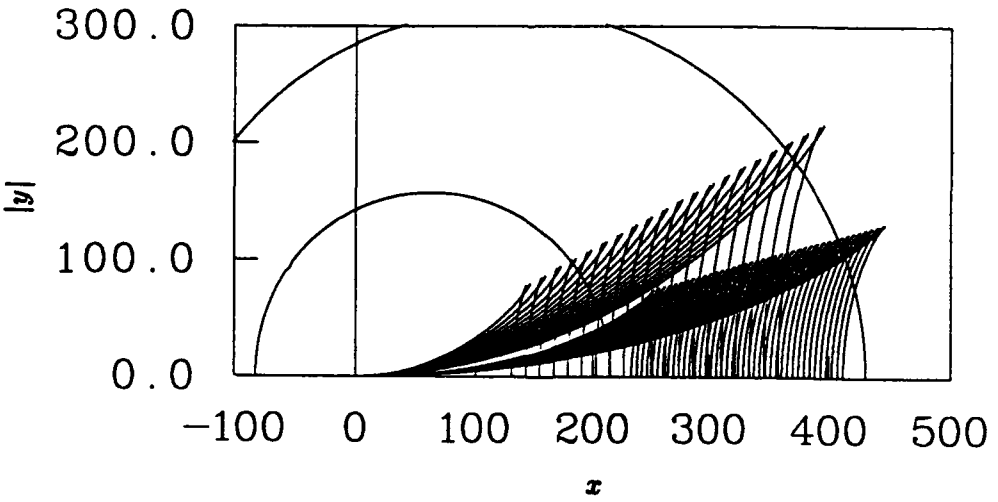


Figure 6.23: Constant phase lines, $\tau = 0.2$

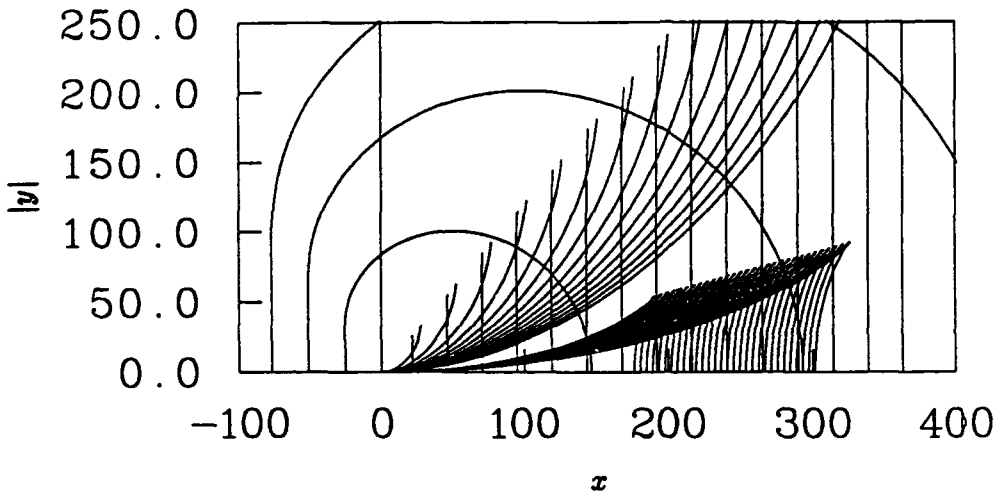


Figure 6.24: Constant phase lines, $\tau = 0.25_-$

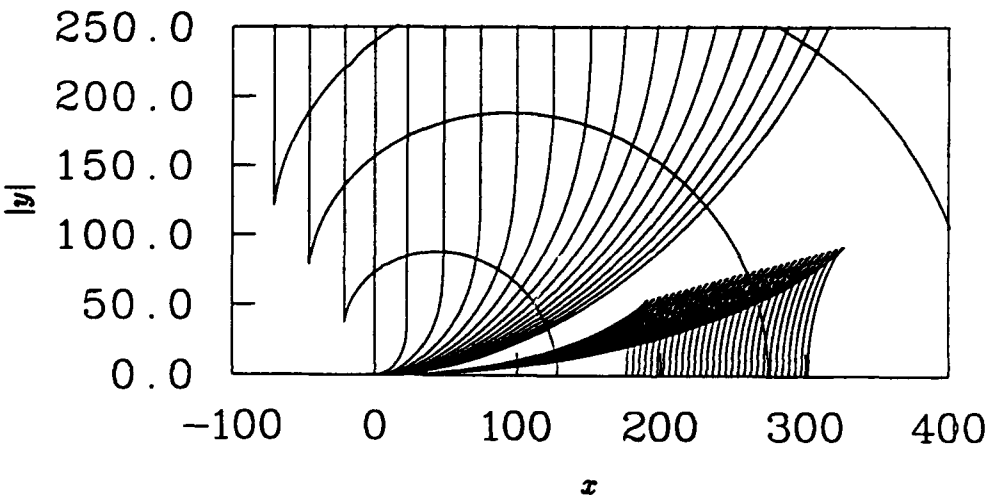


Figure 6.25: Constant phase lines, $\tau = 0.25_+$

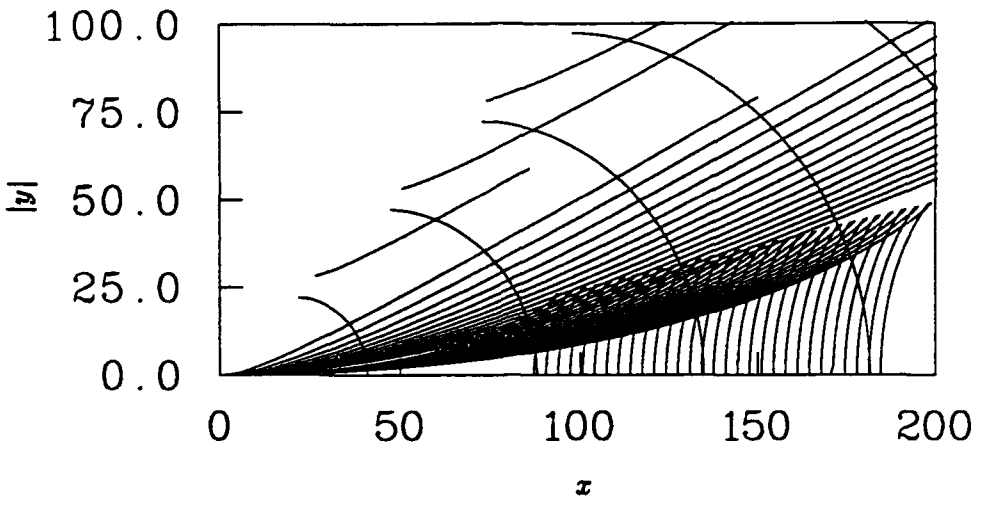


Figure 6.26: Constant phase lines, $\tau = 0.5$

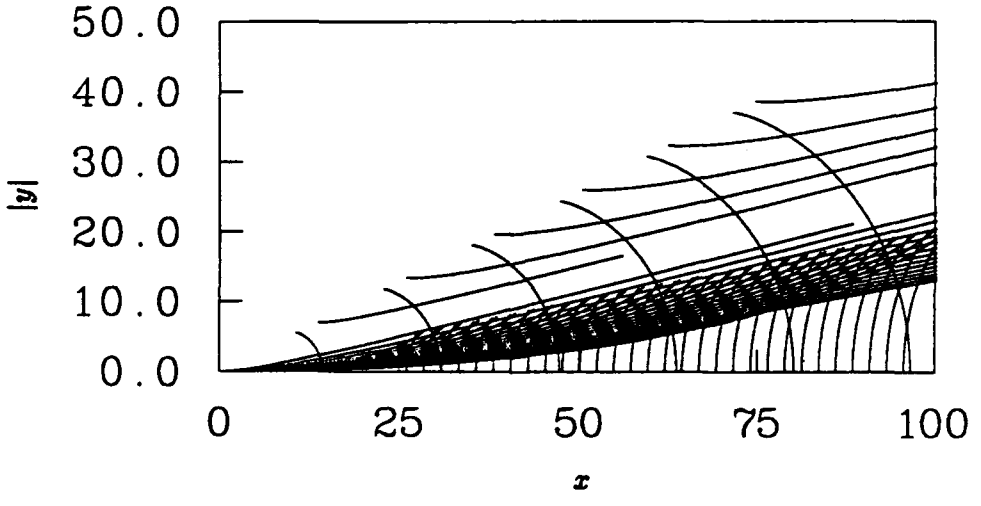


Figure 6.27: Constant phase lines, $\tau = 1.0$

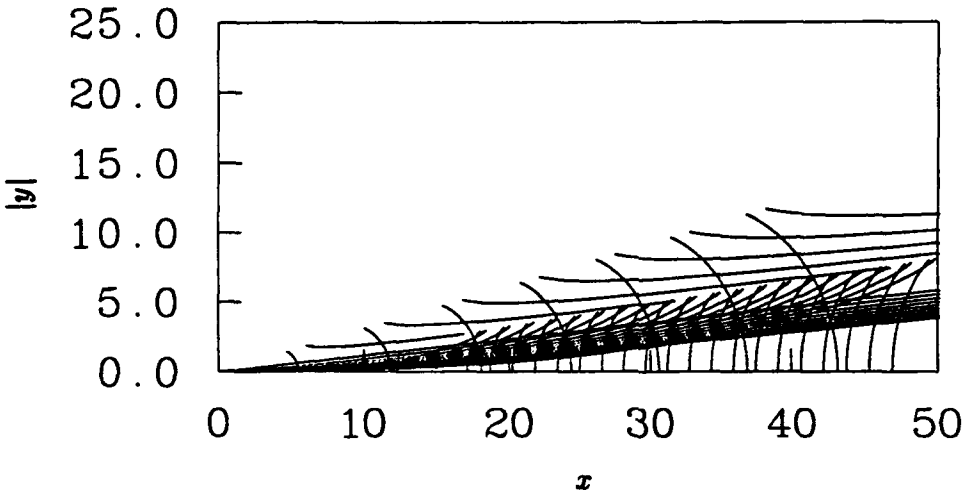


Figure 6.28: Constant phase lines, $\tau = 2.0$

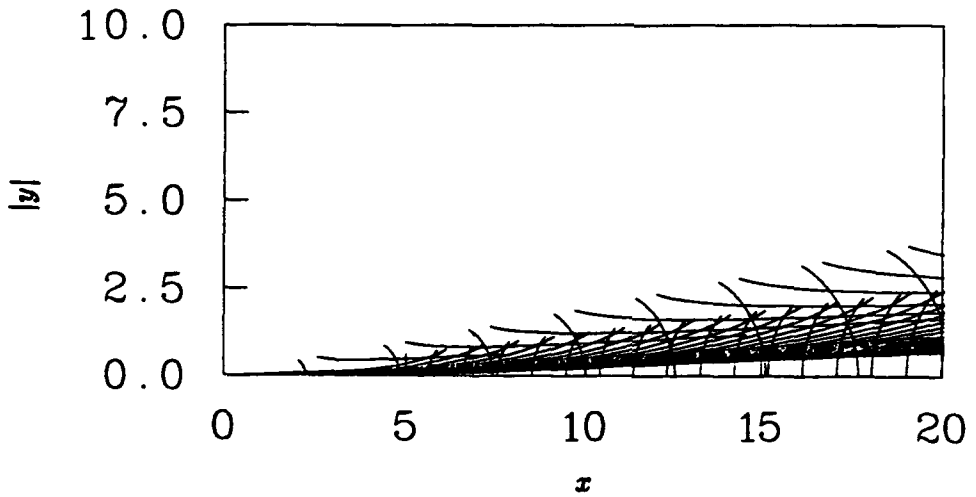


Figure 6.29: Constant phase lines, $\tau = 4.0$

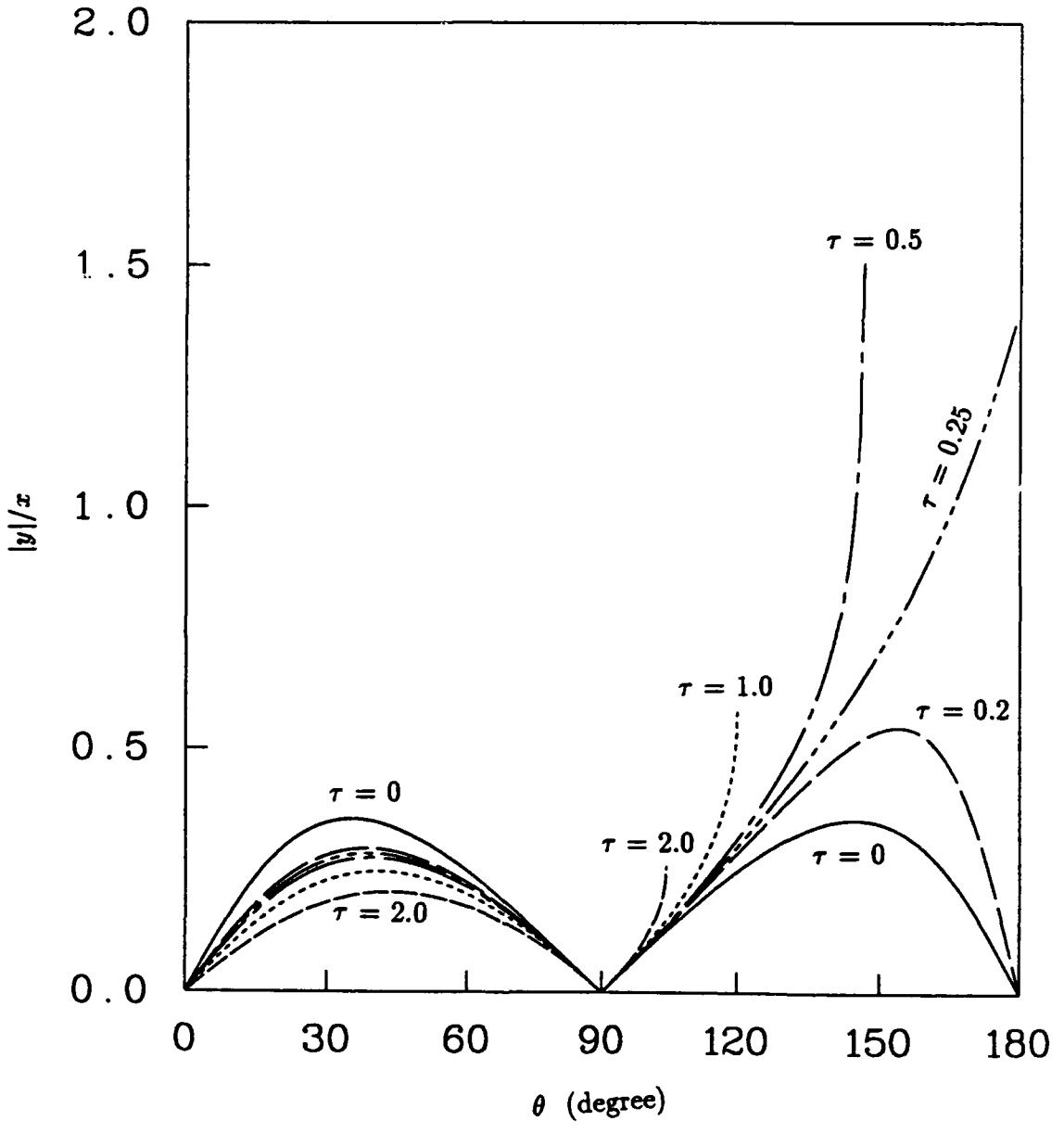


Figure 6.30: $|y|/x$ *vs.* θ for the first and second systems (by stationary phase analysis)

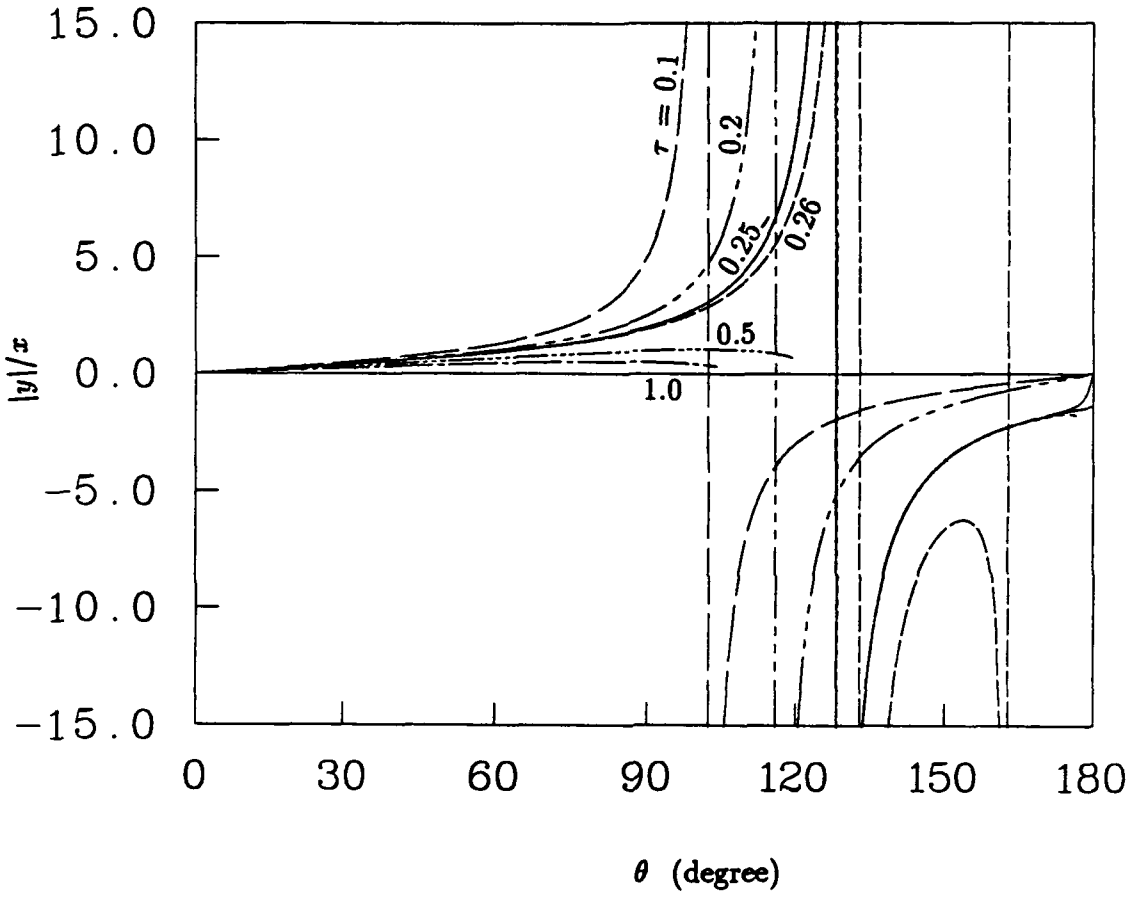


Figure 6.31: $|y|/x$ *vs.* θ for third system (by stationary phase analysis)

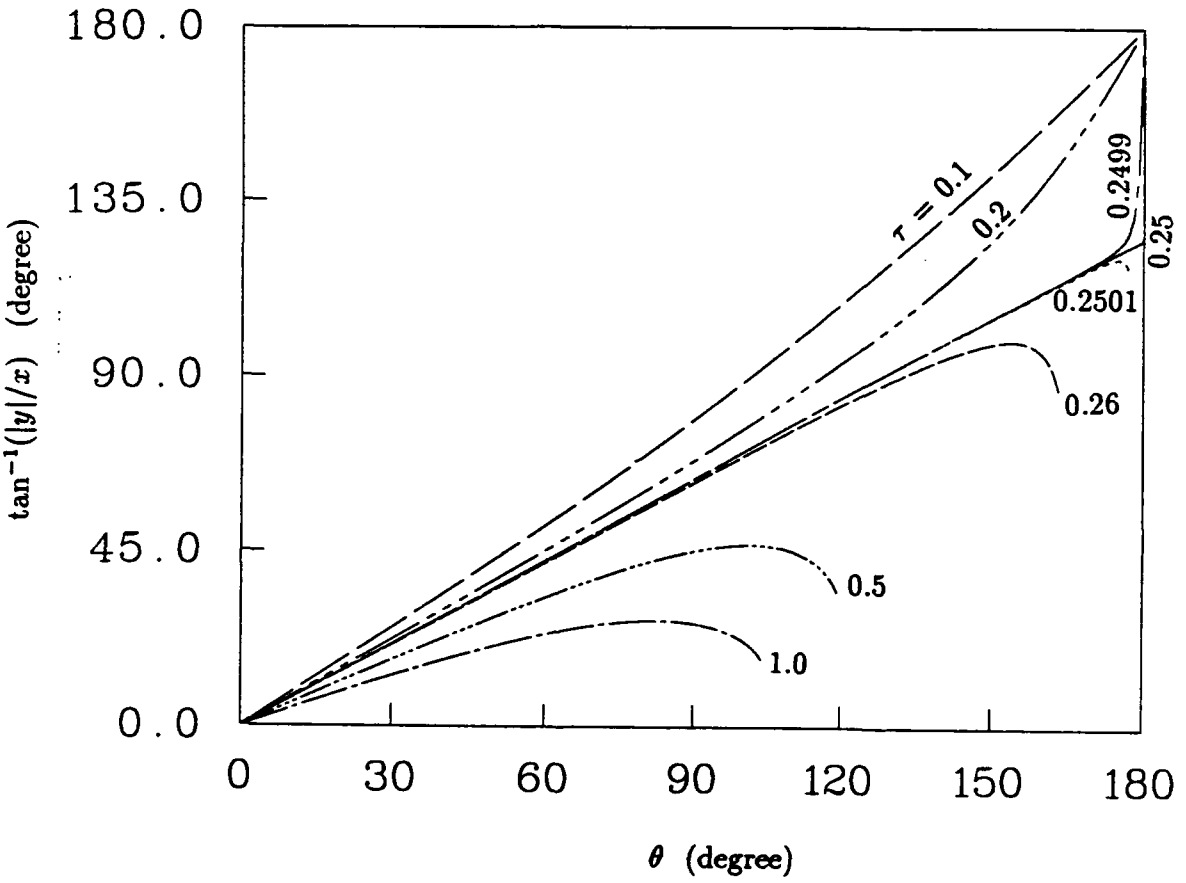


Figure 6.32: $\tan^{-1}(|y|/x)$ *vs.* θ for third system (by stationary phase analysis)

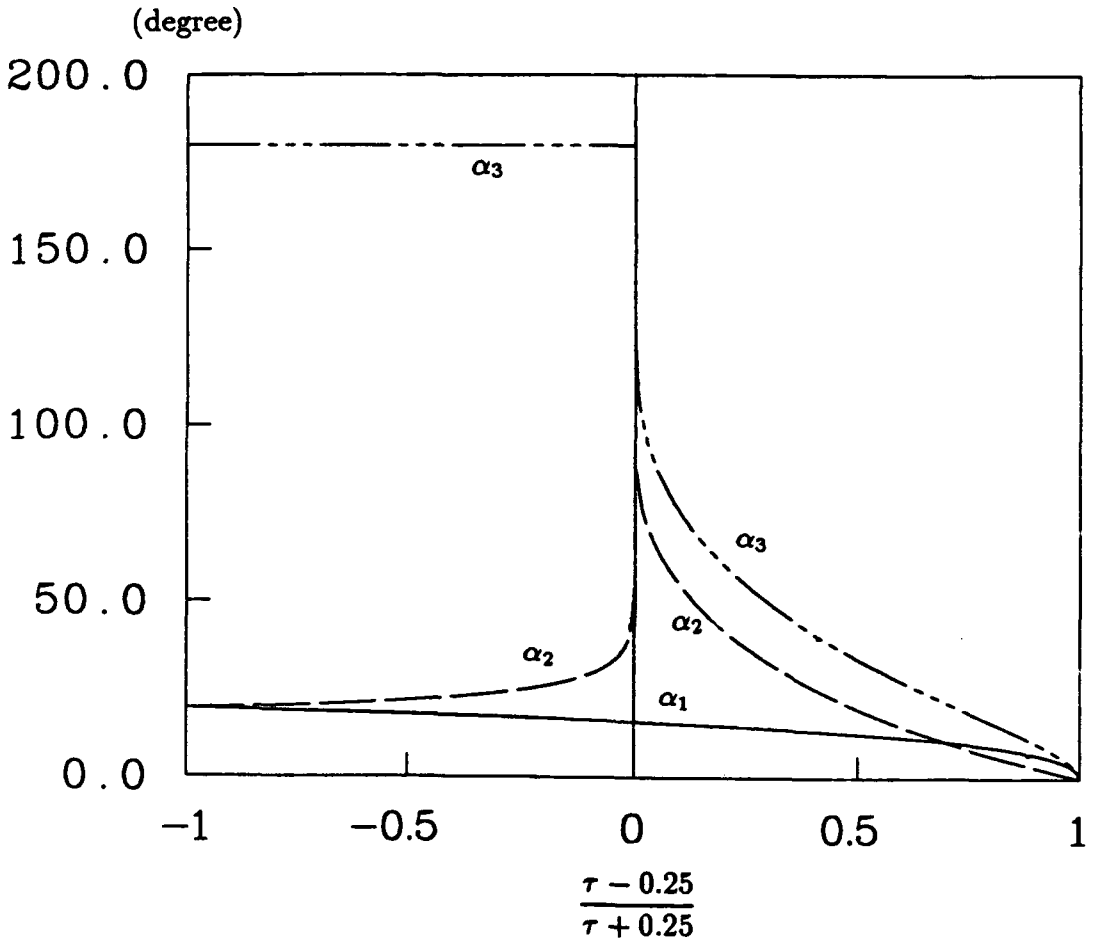


Figure 6.33: Bounding-line angles α_1, α_2 and α_3 *vs* τ (by stationary phase analysis)

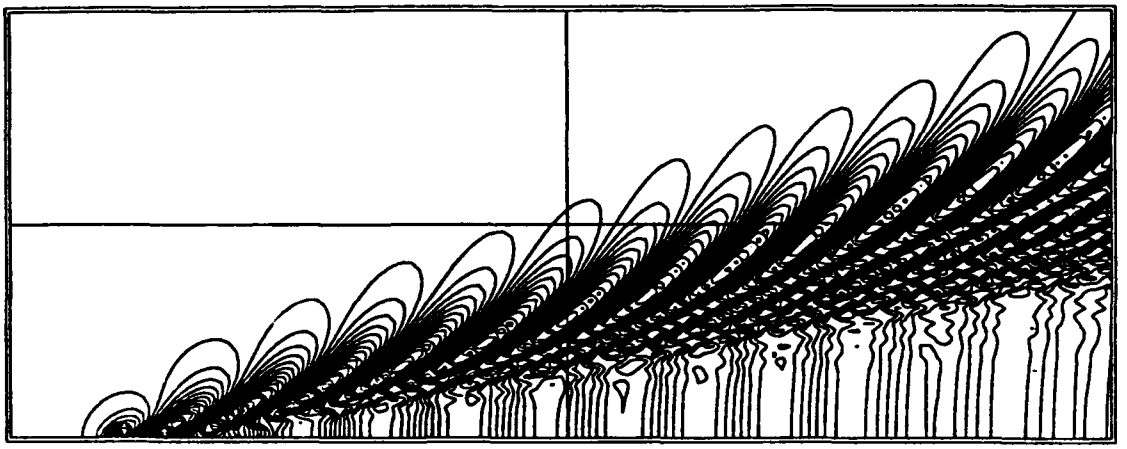


Figure 6.34: Linear steady waves due to a translating source-sink pair, free surface domain ($0 \leq x \leq 11, \ \ 0 \leq y \leq 4.5$)

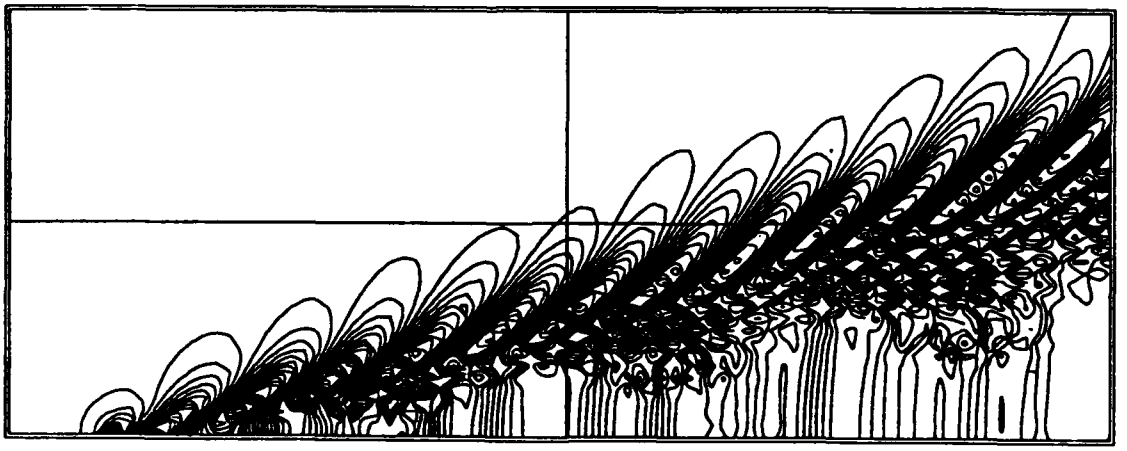


Figure 6.35: Linear waves due to a translating and oscillating source-sink pair, $\tau = 0.5$, free surface domain: ($0 \leq x \leq 11, \ \ 0 \leq y \leq 4.5$)

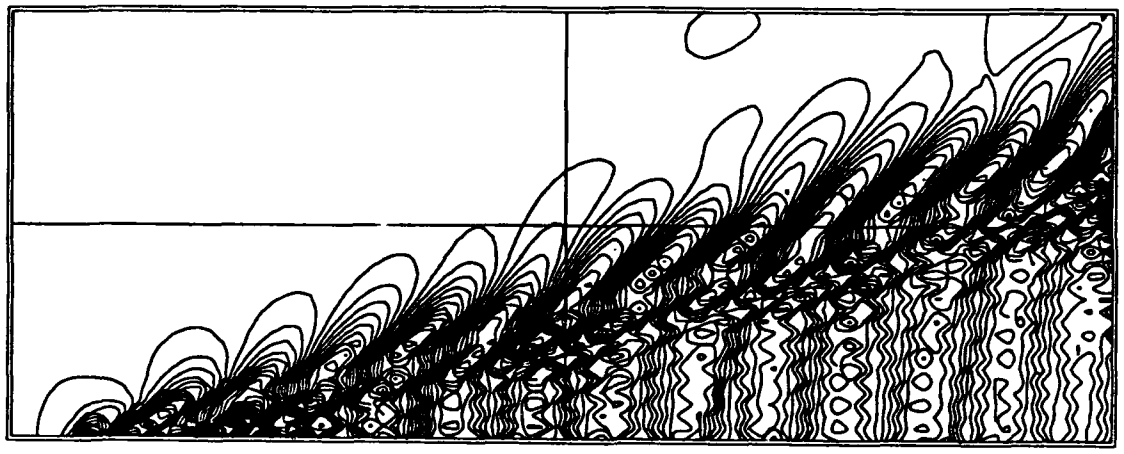


Figure 6.36: Nonlinear waves due to a translating and oscillating source-sink pair, $\tau = 0.5$, free surface domain: $(0 \leq x \leq 11,\ \ 0 \leq y \leq 4.5)$

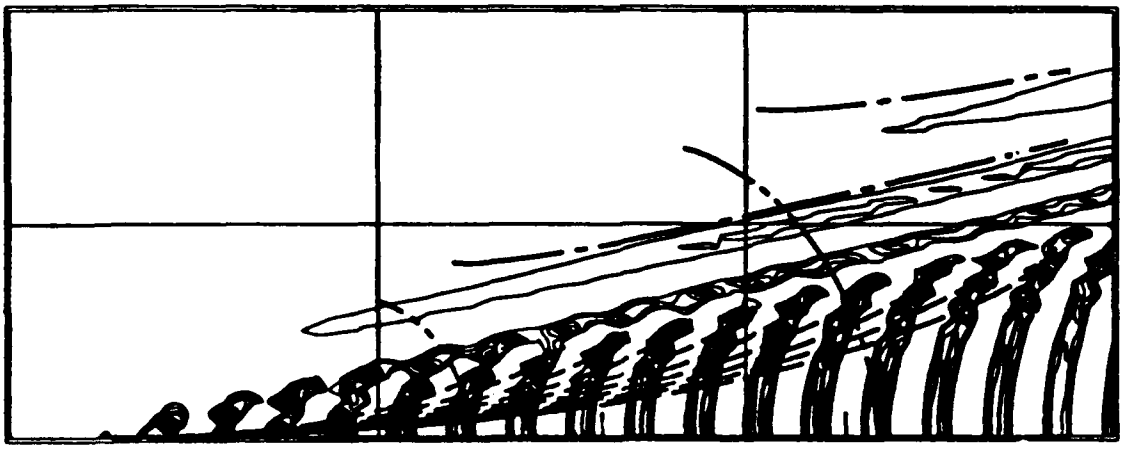


Figure 6.37: Comparison of wave contour lines and constant phase lines for linear waves due to a translating and oscillating source-sink pair, $\tau = 1.0$

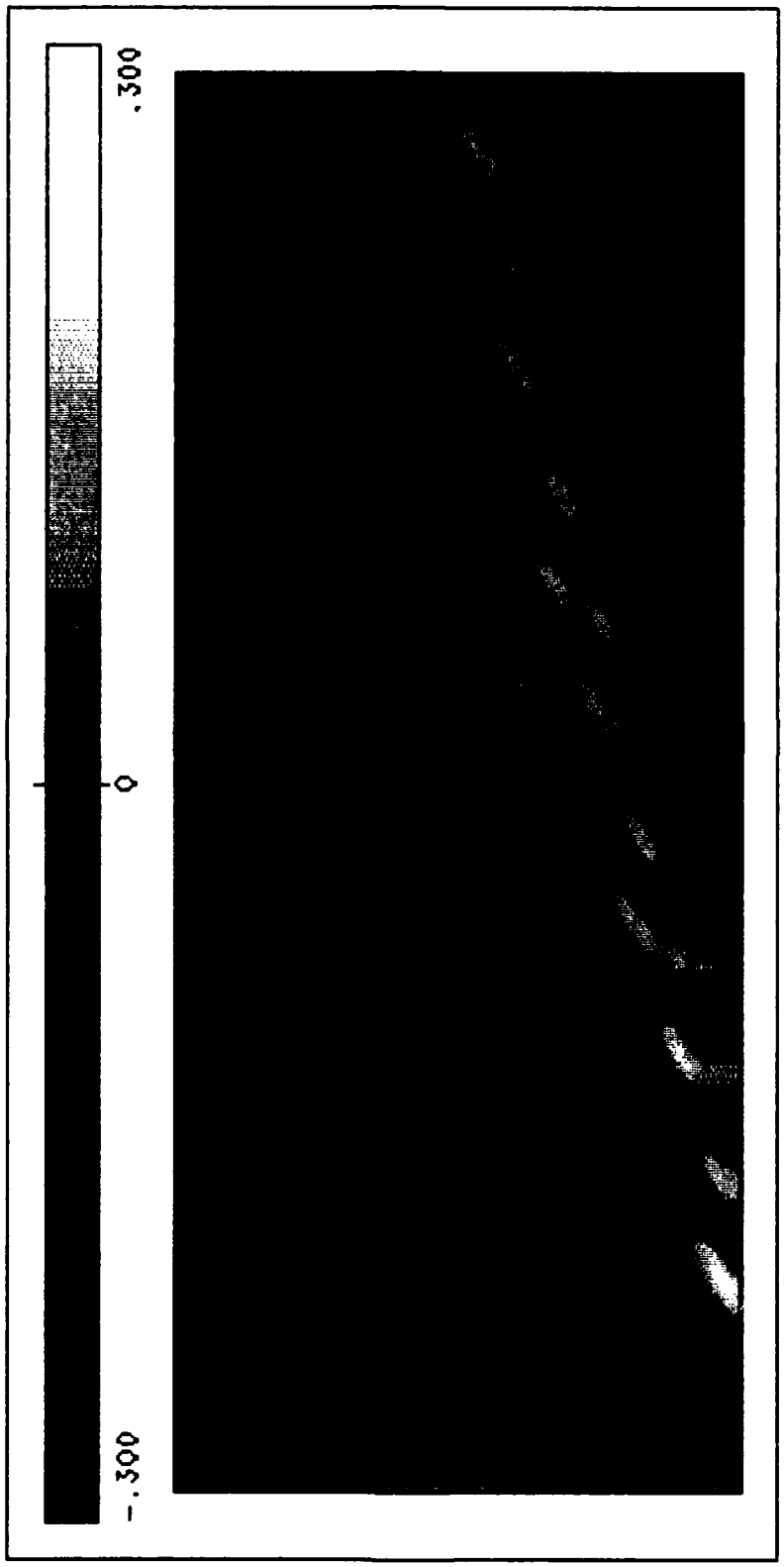


Figure 6.38: Unsteady wake due to a translating and oscillating source-sink pair:
$\tau = 0.5$, zero-mean strength, $t = 12.0$

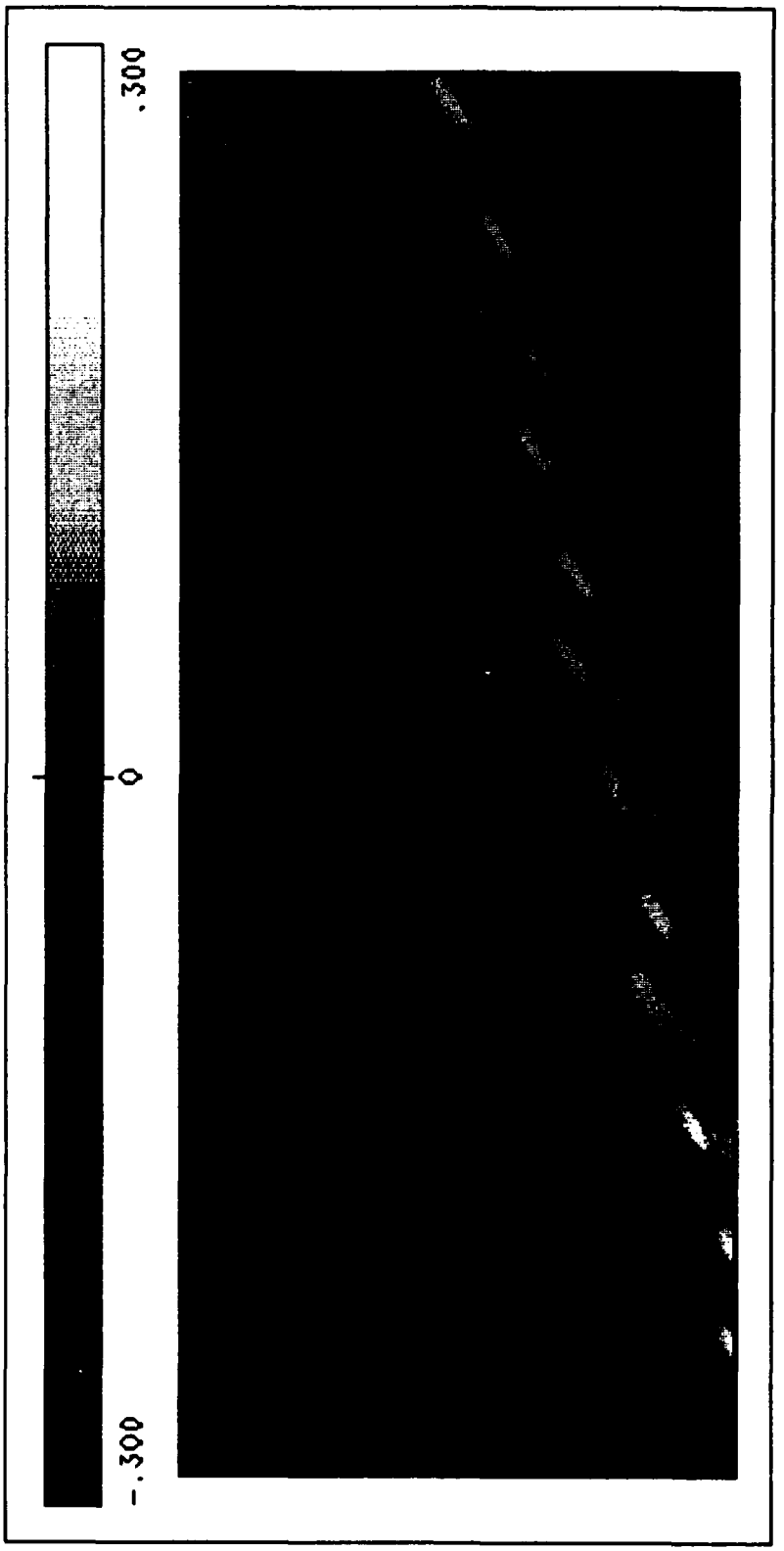


Figure 6.39: Unsteady wake due to a translating and oscillating source-sink pair:
$\tau = 0.5$, zero-mean strength, $t = 12.5$

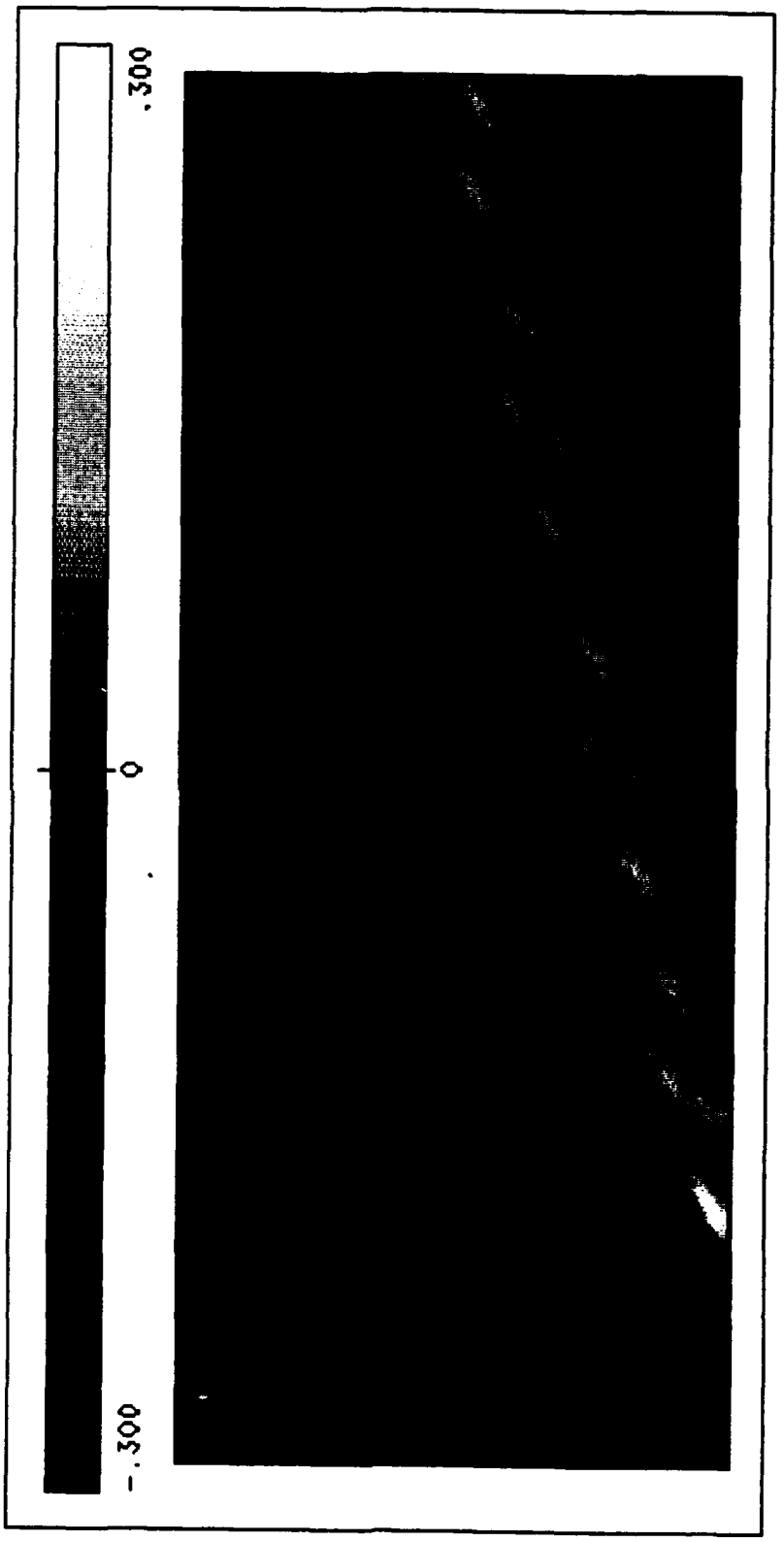


Figure 6.40: Unsteady wake due to a translating and oscillating source-sink pair:
$\tau = 0.5$, zero-mean strength, $t = 13.0$

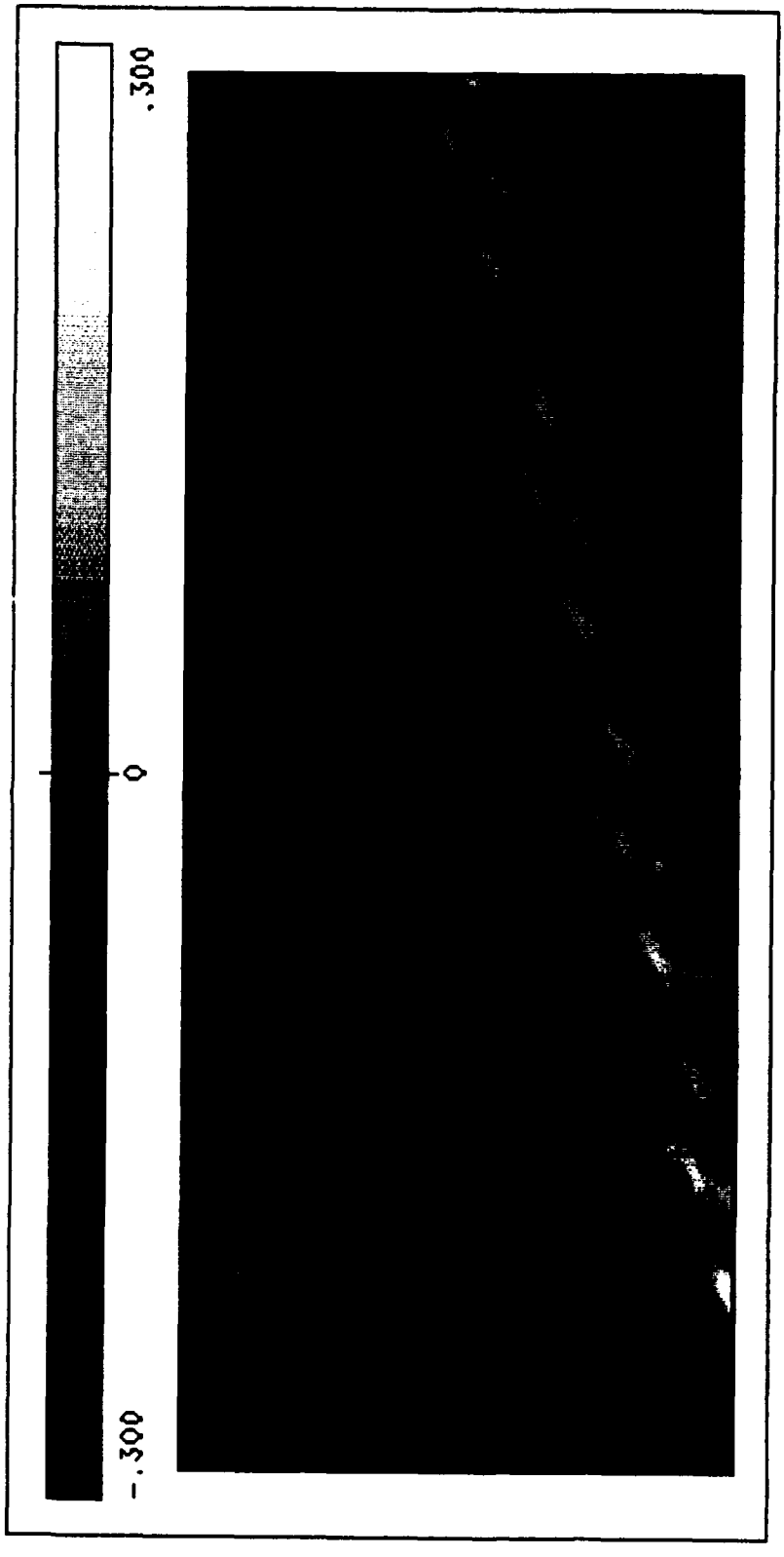


Figure 6.41: Unsteady wake due to a translating and oscillating source-sink pair:
$\tau = 0.5$, zero-mean strength, $t = 13.5$

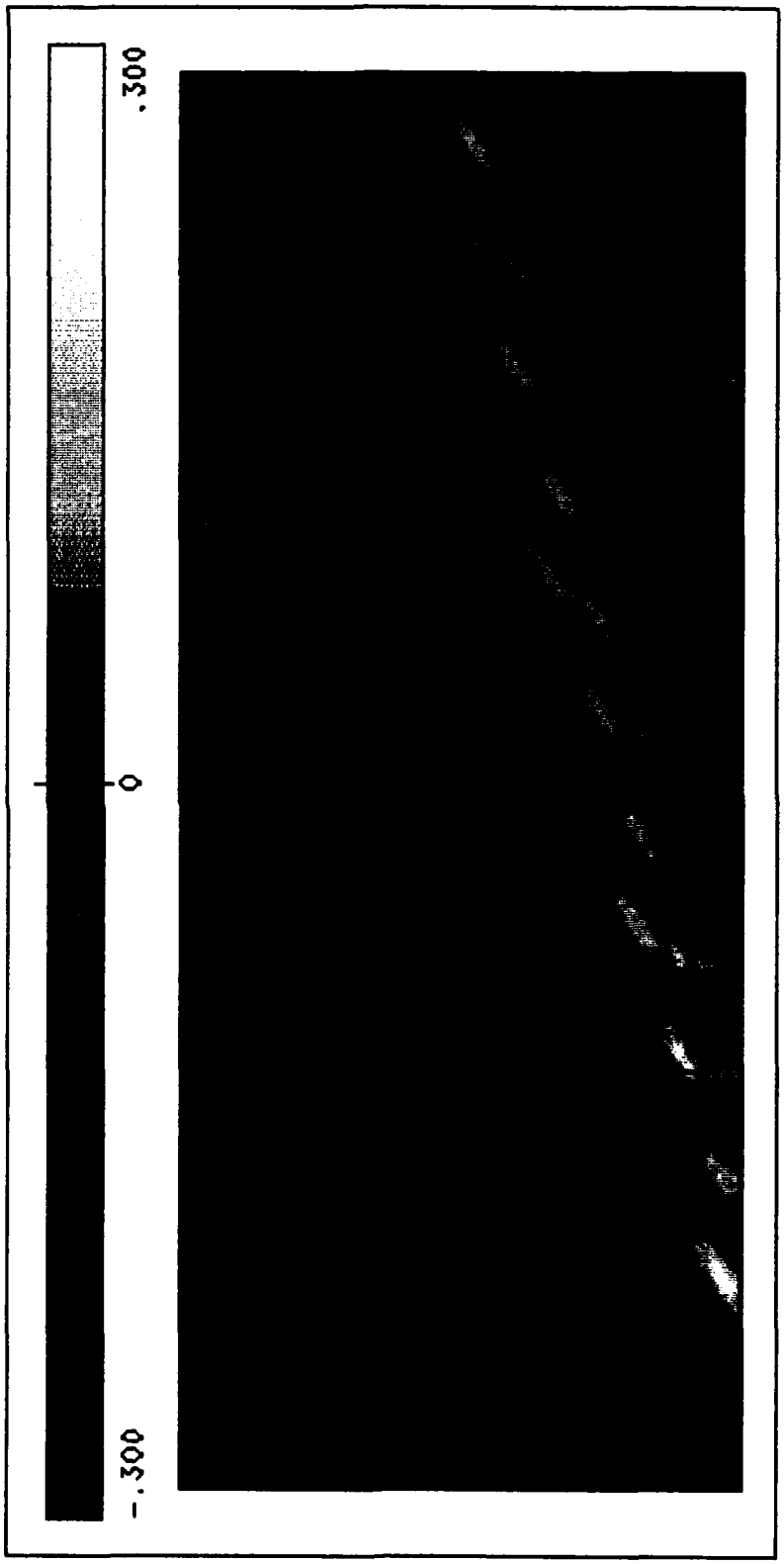


Figure 6.42: Unsteady wake due to a translating and oscillating source-sink pair:
$\tau = 0.5$, zero-mean strength, $t = 14.0$

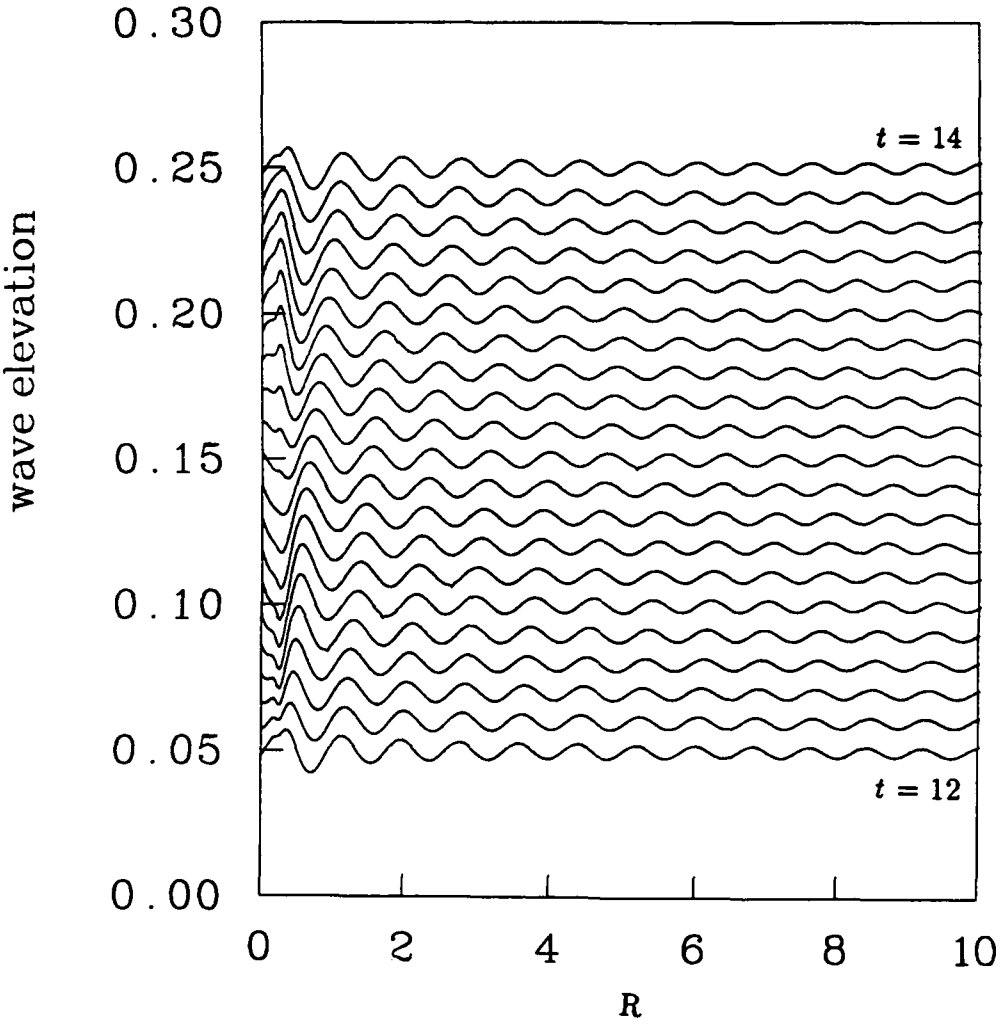


Figure 6.43: Wave elevation along symmetric plane: $\tau = 0.5$, zero-mean strength, $12 < t < 14$)

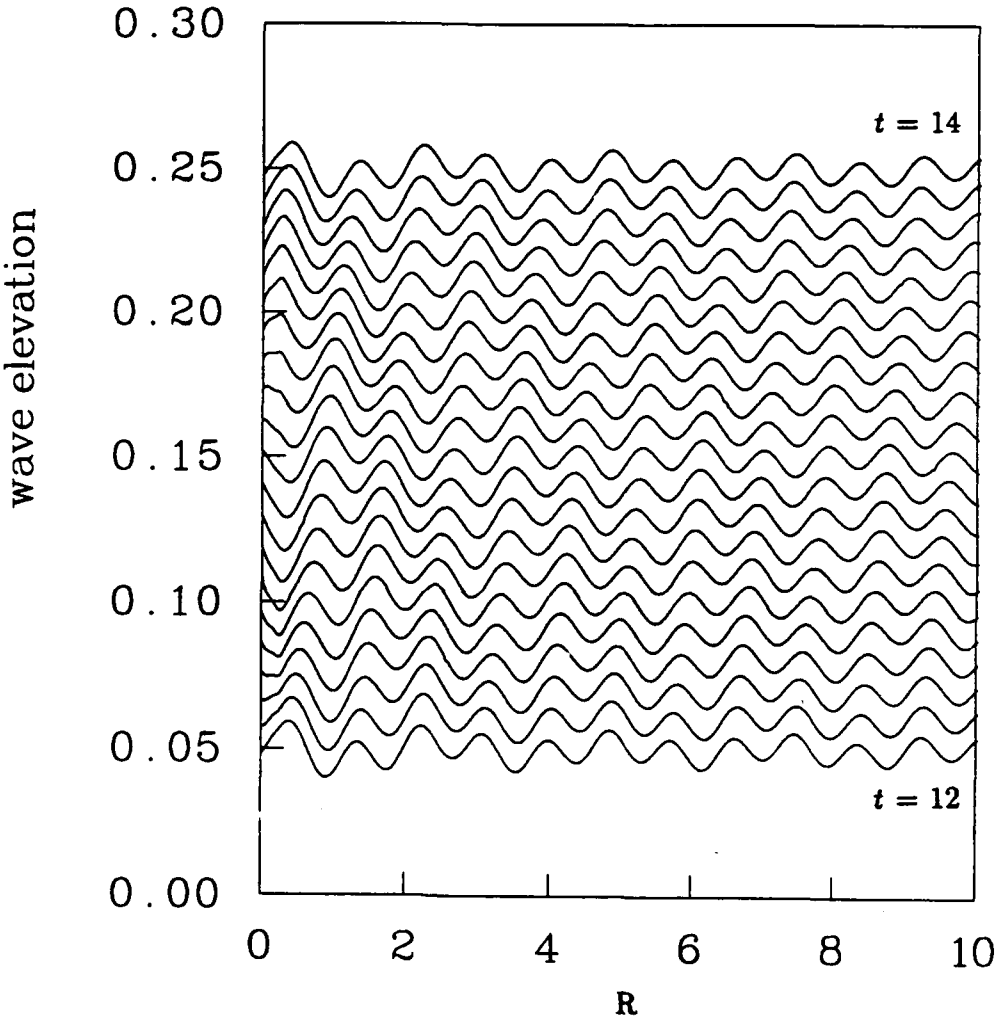


Figure 6.44: Wave elevation along inner-angle wavepacket: $\tau = 0.5$, zero-mean strength, $12 < t < 14$)

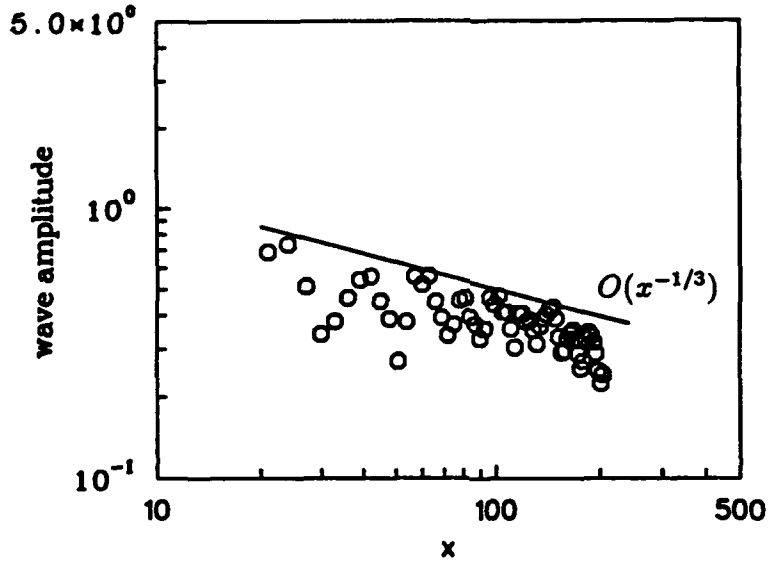


Figure 6.45: Peak wave amplitude within the diverging wave region in nonlinear steady wake

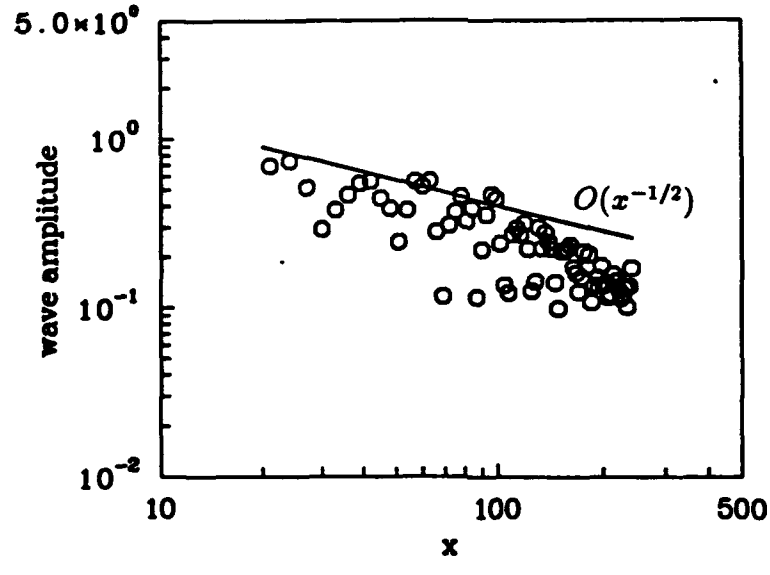


Figure 6.46: Peak wave amplitude within the interference region in nonlinear steady wake

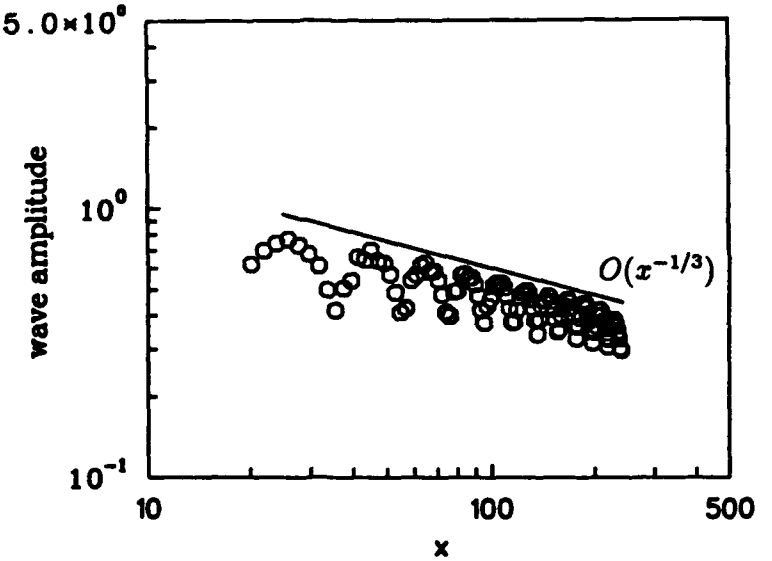


Figure 6.47: Peak wave amplitude within the diverging wave region in linear steady wake

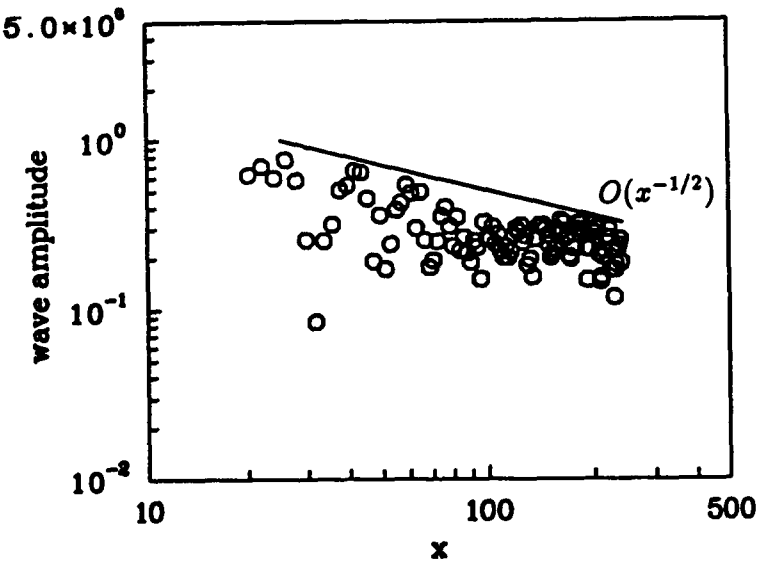


Figure 6.48: Peak wave amplitude within the interference region in linear steady wake

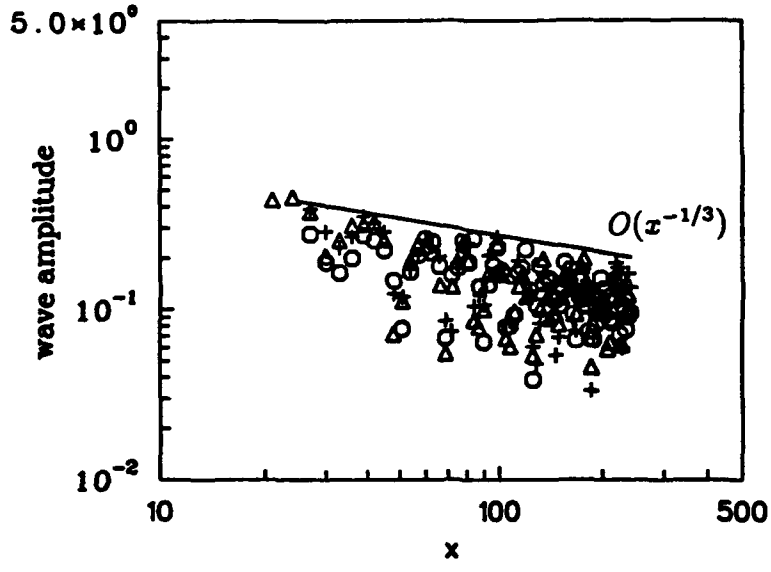


Figure 6.49: Peak wave amplitude within the inner-angle wavepacket in nonlinear unsteady wake

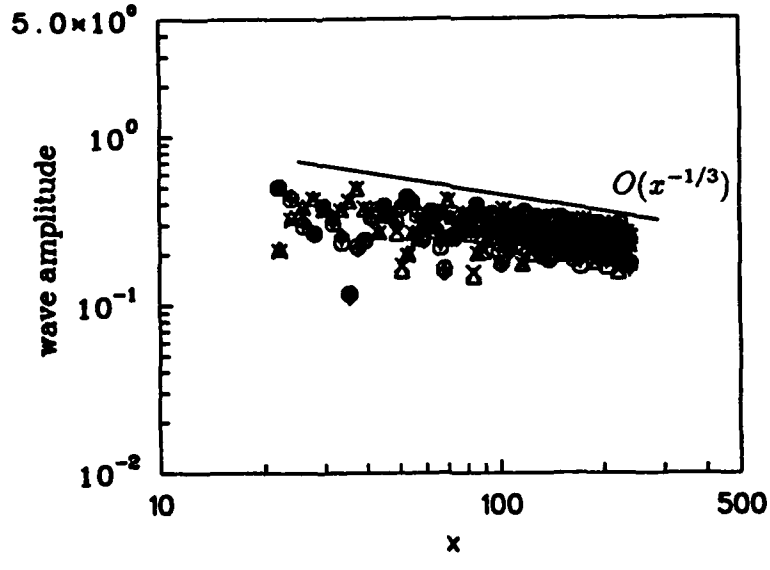


Figure 6.50: Peak wave amplitude within the inner-angle wavepacket in linear unsteady wake

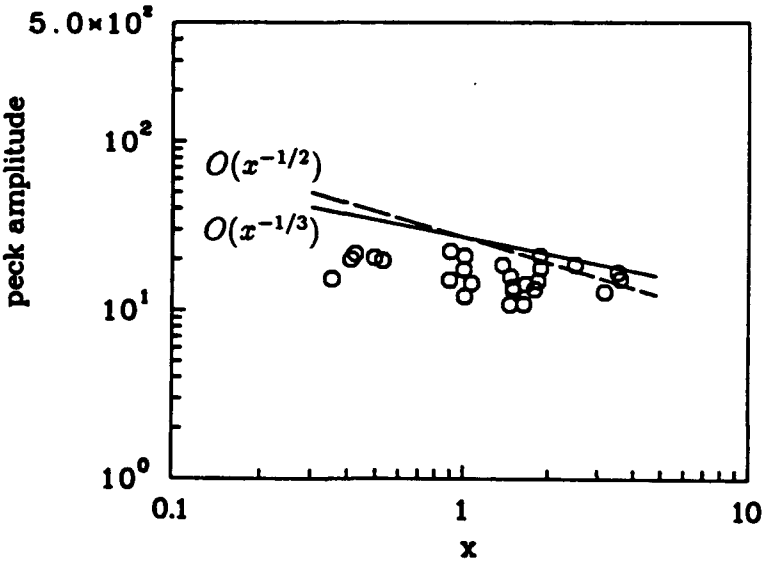


Figure 6.51: Peak wave amplitude within the inner-angle wavepacket in the wake of the cutter Point Brower (experimental data of Brown *et al.* redrawn to show the algebraic decay rate)

CHAPTER VII

CONCLUSIONS AND SUGGESTIONS FOR FURTHER RESEARCH

7.1 Conclusions

The desingularized boundary integral method significantly reduces the time required to compute the influence coefficient matrix of the resulting algebraic system. The indirect method works better than the direct method, especially for the unbounded flows. The matrix is still adequately well conditioned for efficient iterative solutions. Moreover, preconditioning of the matrix greatly reduces the time to solve the algebraic system. For the cases so far investigated, few difficulties of non-physical reflection from the open computation boundaries are encountered. Accurate solutions can be obtained for a large range of desingularization distances on the order of the mesh size. The method is easy to code and vectorize to achieve high performance on supercomputers. The method has been successfully applied to several nonlinear gravity wave problems.

In the two-dimensional upstream runaway soliton problem, the fully nonlinear model predicts the runaway solitons as do the Boussinesq and fKdV models. Our numerical results agree with the fKdV results for small disturbances. However, for

strong disturbances, the fully nonlinear model predicts larger solitons than the fKdV. These soliton are so steep that they will break sometime either upstream or downstream of the disturbance, which have been observed in experiments. For an equivalent distribution, the free surface pressure generates significantly larger waves than the bottom topography.

In the three-dimensional computations for the submerged spheroid, the wave elevation, the pressure distribution on the body and the total forces (drag, lift and moment) are calculated. The convergence with respect to the mesh size, desingularization distance, and energy conservation are checked. The comparison of the drag, lift and moment to other calculations is reasonably good for $H/D = 0.245$. For $H/D = 0.16$, our calculations predict surface piercing of the body. This may be due to the large initial acceleration or high speed of the body (large disturbance). The waves generated by the spheroid and the relevant source-sink disturbance are similar if they are sufficiently submerged. This indicates that a simple disturbance can model the body if the far-field waves are the main interest. This results in significant computational savings.

The nonlinear and linear computations, as well as the stationary phase analysis for the waves due to the source-sink pair or surface pressure patch, have shown that nonlinear effects are not necessary in the generation of the inner-angle wavepackets while the unsteadiness of the flow can cause the inner-angle waves. The wave packet angle decreases with the the increase of the reduced frequency. The inner-angle wave packet decays at the same rate as the Kelvin diverging waves. It appears that the angle and persistence of the inner-angle wavepacket behind the ship can be explained by the unsteady linear wave theory. The 10.8° inner-angle observed in the experiment

of the Coast Guard cutter Point Brower corresponds to $1.0 < \tau < 1.5$.

7.2 Suggestions for Further Research

Desingularization greatly simplifies the boundary integration and also reduces the computation time. However, the desingularizied boundary integral method is still an $O(N^2)$ algorithm. When preconditioning of the influence matrix is employed, the calculation of the influence matrix and the velocity on the free surface dominates the computation time (solving the matrix equation takes only 20% to 30% of the total CPU time) for $N \approx 3000$. The GMRES is also an $O(N^2)$ algorithm. The recently developed Fast Multipole Method for the so-called N-body potential problem (Rokhlin 1985, Greengard & Rokhlin 1988, Greengard 1990, and Korsmeyer 1990) seems promising to be incorporated with the desingularization. The multipole method evaluates the influences among the N bodies (mass particle, electronic charges, sources, dipoles, etc.) using multipole expansions to reduce the operation count from $O(N^2)$ to $O(N \log N)$. When the multipole method is used with an iterative solver for a boundary value problem, it is not necessary to form the influence matrix explicitly. This not only reduces the memory storage requirement but also reduces the operations for the iterative solver from $O(N^2)$ to $O(N \log N)$. It is expected that the computation time could be greatly reduced for very large scale calculations with the combination of desingularization, multipole expansions and preconditioning.

Parallel architecture shows great potential to speed up computations (Duncan 1990, Carriero & Gelernter 1989). There are great potentials for parallel computations using the desingularized method. Parallel computations may become imperative if the multipole method is used, since the sorting of the particles in the multipole

method requires many IF statements which degrade the vectorization of the program but not parallelism.

Introducing a small number of Havelock sources into nonlinear wave calculations can improve the accuracy of the results (Scragg & Talcott 1990). The far-field conditions can be better satisfied and a smaller free surface computational domain may be required. However, numerical instability in the evaluation of Havelock source can sometimes cause difficulties. The use of the Fourier-Kochin representation to avoid these difficulties has been under investigation (Noblesse & Hendrix 1990). For unsteady calculations, large memory storage (proportional to the simulation time because of the time convolution integration) is required to store the influences due to the sources for each of the previous time steps. Before this problem is solved, large time simulations are unlikely.

The present work should be extended to the case of surface-piercing bodies to solve practical seakeeping problems, such as the extreme motions of a ship in a seaway. This is very important in design. The effects of the ship hull on the interaction of bow and stern waves will also allow a better understanding of the inner-angle wave phenomenon. The ship motions and the waves can be solved together. However, in addition to the difficulties associated with the discretization of the wetted ship surface and the free surface which change with time, the singular behaviors of the solution at the intersection line of the ship surface and the free surface is the most important and difficult problem. The rapid change of the boundary conditions of the two surfaces at the intersection line is the cause of the singularity. In time-stepping computations, the specification of the initial conditions (or the boundary conditions for the first time step) has a significant effect on the solution even in the

very simple wavemaker problem (Joo, Schultz & Messiter 1990). Some alternative to the standard time-stepping algorithm used in this study may need to be developed.

Our conclusion about nonlinear effects on the formation and persistence of the inner-angle wavepacket is based on our limited nonlinear wave calculations in which the strength of the disturbance is restricted so that no wave breaking occurs. Therefore, the disturbances used may not be sufficiently strong to produce significantly nonlinear waves in the far field. Wave breaking was observed in the cutter Point Brower experiment. The far-field nonlinearity may play an important role, for instance in making the inner-angle waves more isolated (or sharper). Our method must be modified to continue computation after the wave breaking occurs. The main difficulty is very similar to that in the surface piercing body problem. The free surface is no longer smooth at the point where the wave starts to break. Therefore, the solution to the surface piercing body problem may provide some insight in solving the wave breaking problem.

APPENDICES

APPENDIX A

Tests for Multigrid Method

Multigrid methods have been widely used and proved effective in various finite difference schemes (differentiation type). Although the application of multigrid methods to boundary integral methods (integration type) are relatively limited, it could be a good alternative to speed up the computation. Here, we examine the application of a three-level W type multigrid method to our desingularized boundary integral method. *Briggs (1987) provides a good introduction to mutligrid methods.*

For an approximation $\mathbf{x}^*$ to the equation (6.1)

$$\mathbf{A}\mathbf{x} = \mathbf{b}. \tag{A.1}$$

we have the residual vector $\mathbf{r} = \mathbf{b} - \mathbf{A}\mathbf{x}^*$. Defining the error as the difference between the exact solution to (6.1) and the approximation, $\mathbf{e} = \mathbf{x} - \mathbf{x}^*$, we have the following equation for the error in terms of the residual:

$$\mathbf{A}\mathbf{e} = \mathbf{r}. \tag{A.2}$$

The principle of multigrid is that different frequency components of the error are most efficiently handled on different grids. Low frequency components are best minimized on a coarse grid while high frequency components are best minimized on fine grids.

For ease of presentation we address the case of two grids. Extension to more grids are readily made. In the following, the superscripts f and c denote the fine grid and the coarse grid respectively. Let $\mathbf{x}^f$ be the approximation to (6.1) after several iterations by an iterative solver on the fine grid, then the residual on the fine grid is

$$\mathbf{r}^f = \mathbf{b}^f - \mathbf{A}^f\mathbf{x}^f. \tag{A.3}$$

The residual $\mathbf{r}^f$ on the fine grid is interpolated to the coarse grid via a "restriction" operator $\mathbf{R}$:

$$\mathbf{r}^c = \mathbf{R}\mathbf{r}^f. \tag{A.4}$$

The error equation (A.2) is solved (directly or iteratively) on the coarse grid:

$$\mathbf{A}^c\mathbf{e}^c = \mathbf{r}^c. \tag{A.5}$$

The error $\mathbf{e}^c$ is interpolated to the fine grid via a "prolongation" operator $\mathbf{P}$:

$$\mathbf{e}^f = \mathbf{P}\mathbf{e}^c. \tag{A.6}$$

The latest fine grid iterate is then corrected via:

$$\mathbf{x}^f \Leftarrow \mathbf{x}^f + \mathbf{e}^f. \tag{A.7}$$

The coarse and fine grid matrices $\mathbf{A}^f$ and $\mathbf{A}^c$ are set up in an identical manner; the only difference is the truncation used. Equation (6.1) is again solved on the fine grid by the iterative solver using the multigrid-corrected iterate $\mathbf{x}^f$ as the initial approximation.

In our computations, if the desired accuracy is not achieved within the specified K iterations, the multigrid correction is applied and the iterative solver is called again for another K iterations. The use of multigrid may affect the performance of the

iterative solver used. The performance of SOR (successive over-relaxation), which is most widely used in multigrid methods, is not significantly affected by multigrid. However, GMRES (generalized minimal residual method—an extension of conjugate gradient method), which is much more effective than SOR for nonsymmetric matrices, can be degraded by multigrid. Consider an approximate solution of the form $\mathbf{x}^* + \delta\mathbf{x}$, where $\mathbf{x}^*$ is the initial guess and $\delta\mathbf{x}$ is the correction to $\mathbf{x}^*$. $\delta\mathbf{x}$ is a member of the Krylov space $\Xi = span(\mathbf{r}_o, \mathbf{A}\mathbf{r}_o, \mathbf{A}^2\mathbf{r}_o, ..., \mathbf{A}^{k-1}\mathbf{r}_o)$, in which $\mathbf{r}_o = \mathbf{b} - \mathbf{A}\mathbf{x}^*$ is the residual and k ($\leq K \ll N$) is the dimension of Ξ. The GMRES algorithm determines $\delta\mathbf{x}$ such that the 2-norm of the residual (*i.e.* $\|\mathbf{b} - \mathbf{A}(\mathbf{x}^* + \delta\mathbf{x})\|$) is minimized. k is also the number of iterations conducted, which means that the dimension of Ξ increases as the iteration number increases. K is a specified upper limit of k before restarting of a GMRES cycle. Usually, the performance of the GMRES is poor if K is too small. Fig. A.1 shows the the 2-norm of the residual vs the number of iterations for three cases for a total of 100 iterations without a multigrid correction. The GMRES is restarted every $K = 5$ iterations in the first case, $K = 20$ iterations in the second case and $K = 100$ in the third case. As can be seen, after 100 iterations, the third case has a much smaller residual than the other two cases. Also shown is the result for the SOR. The GMRES is better than the SOR unless it is restarted too frequently and therefore is degraded.

Fig. A.2 shows the effect of multigrid on the GMRES. A coarse multigrid correction is applied every K iterations (no multigrid correction for $K = 100$). For $K = 5$, the multigrid reduces the residual faster in the first few iterations (≤ 20 iterations) but slows down the convergence significantly afterward. For $K = 20$, the multigrid does not help even in the first few iterations although the GMRES with $K = 20$ performs better than with $K = 5$. Fig. A.3 shows the effects of multigrid on the

SOR. The multigrid accelerates the convergence for the SOR. However, it does not help much if a large number of iterations are required to achieve the desired accuracy. In our nonlinear wave calculations, we usually require the 2-norm of the residual to be less than 10^{-6} to 10^{-7}, which means that more than 100 iterations are required if the GMRES is used. Therefore, the GMRES without multigrid correction is still superior.

Another reason why the multigrid correction may not help in our application of the desingularized method is that the integrations over the auxiliary boundary must be evaluated more carefully (a distributed source instead of isolated sources must be used) and the desigularization distance should not change for different grids so that the residual can be restricted to the coarser grids and the errors prolonged up to the finer grids. This not only increases the computation time in setting up the matrix **A** but may also cause convergence problems for the desingularized method since the ratio of the desigularization distance to the local mesh size is no longer the same on the different grids.

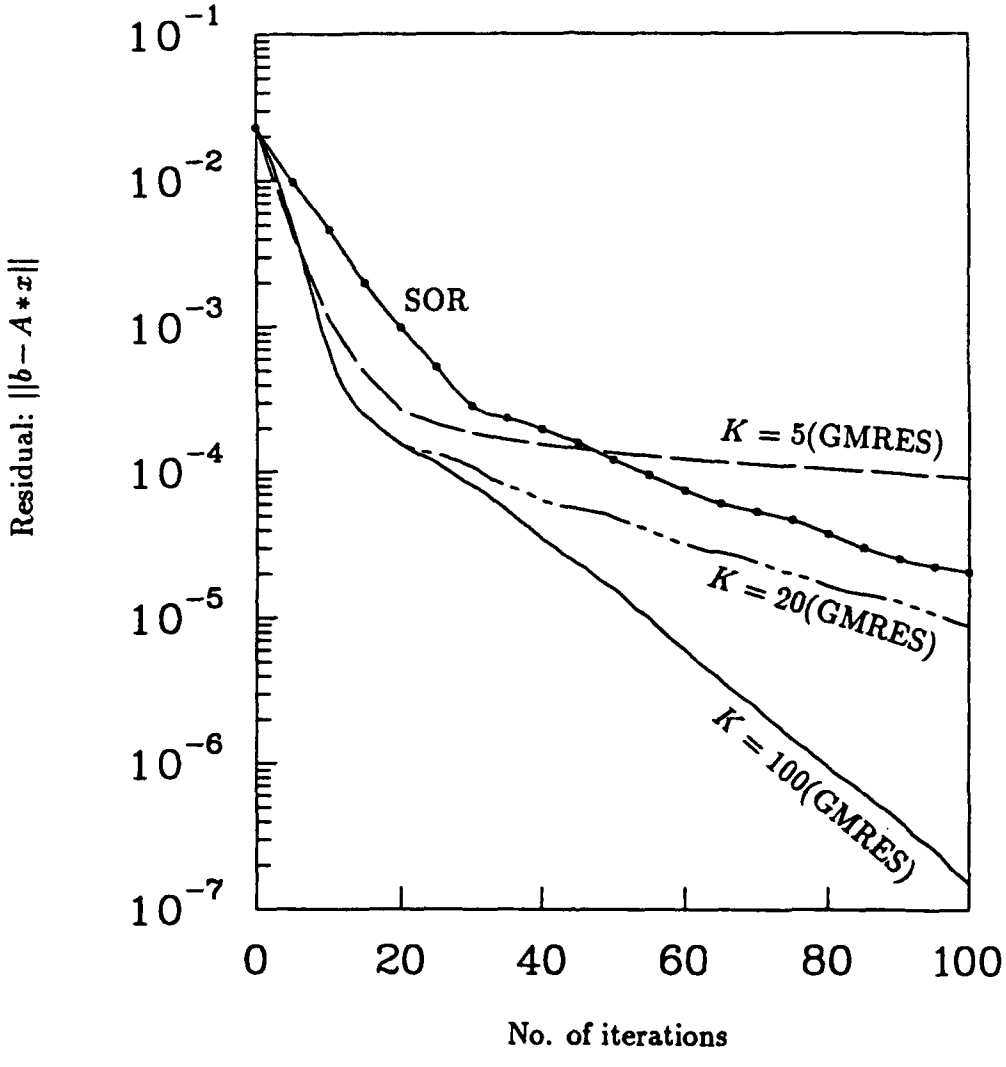


Figure A.1: Effect of restarting of GMRES on residual

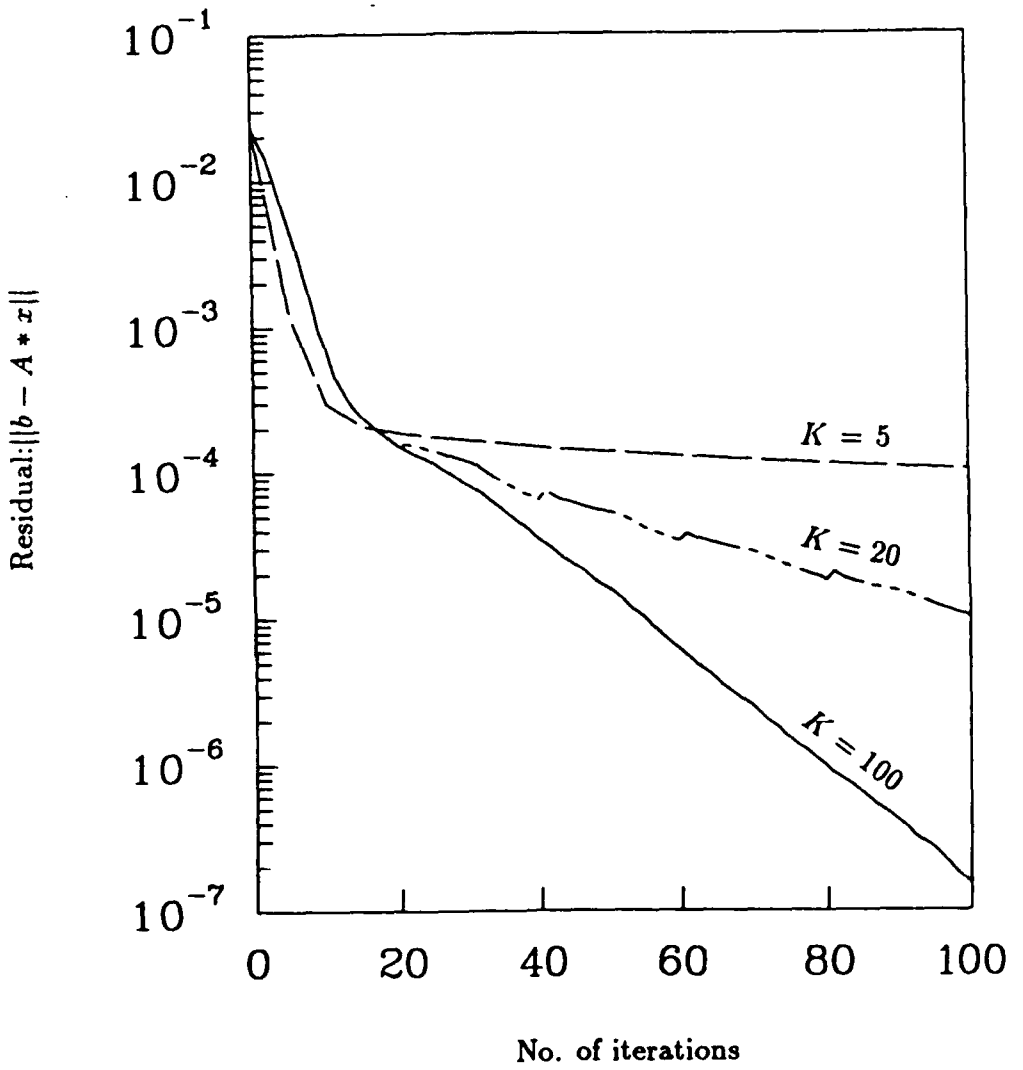


Figure A.2: Effect of multigrid on the convergence with GMRES

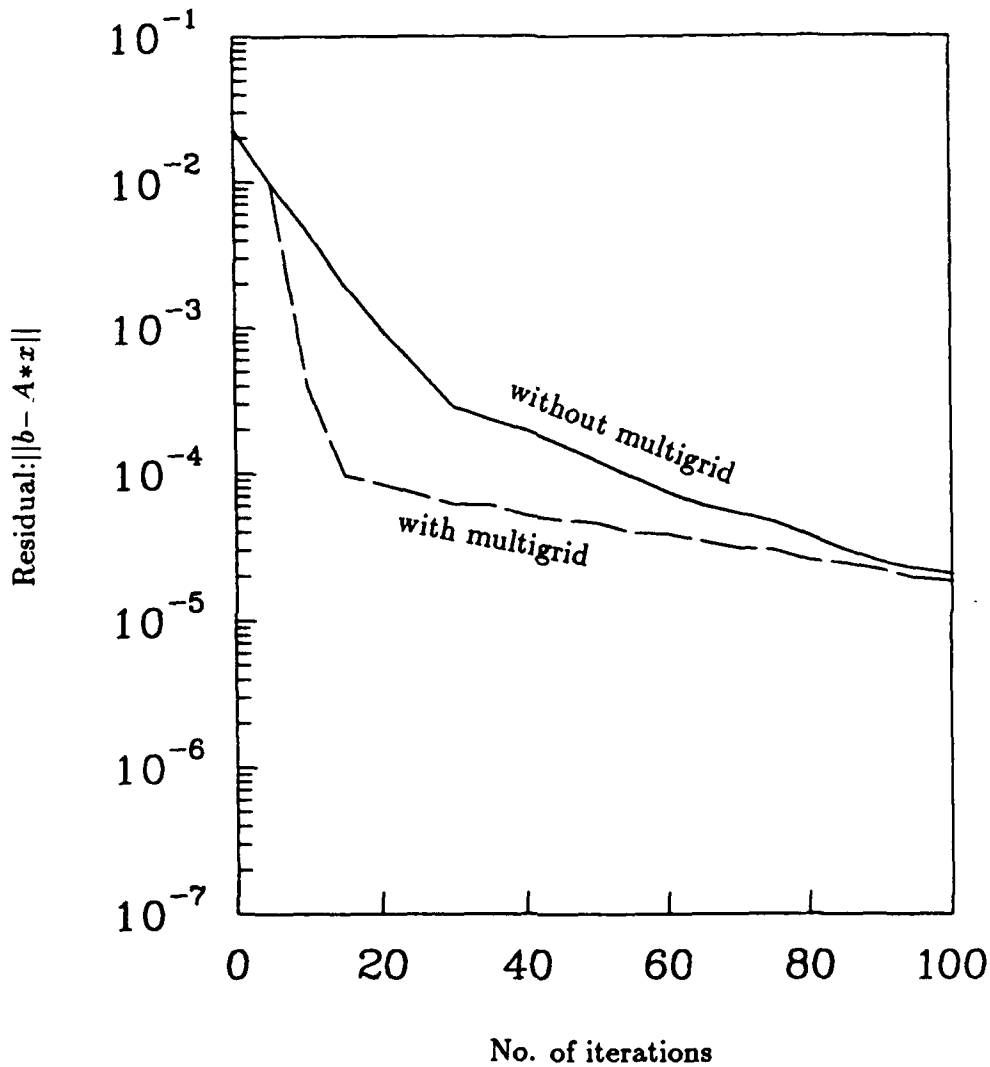


Figure A.3: Effect of multigrid on the convergence with SOR

APPENDIX B

Preconditioning of Equation (6.1)

We seek another alternative to accelerate the convergence: preconditioning of (6.1). The basic idea of preconditioning is to find an approximate matrix $\hat{\mathbf{A}}$ to $\mathbf{A}$ so that $\hat{\mathbf{A}}^{-1}\,\mathbf{A}$ is close to the identity matrix or a strongly diagonally dominated matrix so that the preconditioned equation:

$$\hat{\mathbf{A}}^{-1}\mathbf{A}\mathbf{x} = \hat{\mathbf{A}}^{-1}\mathbf{b} \tag{B.1}$$

is better conditioned than the original system (6.1). Thus, it can be solved by an iterative solver with much fewer iterations. Clearly, one requirement for $\hat{\mathbf{A}}$ is that it be easily invertible or decomposed (*i.e.*, a linear system having $\hat{\mathbf{A}}$ as the coefficient matrix can be solved with much less effort than solving the original system). To reduce the number of iterations, it is also desirable that $\hat{\mathbf{A}}$ be close to $\mathbf{A}$. Therefore, in choosing a preconditioner, one must select between methods which usually perform a large number of "cheap" iterations or a small number of "expensive" iterations.

There exist many preconditioning methods, such as the Richardson method, the incomplete LU decomposition method, the modified LU decomposition method, *etc.* and the subroutines based on these methods are available in the NSPCG (Non-symmetric Preconditioned Conjugate Gradient) package. Oppe, Joubert & Kincaid

(1988) give a brief background on preconditioners. Usually, these methods are very effective for sparse matrices. In general, for a dense, nonsymmetric matrix, it is not easy to find a "close" matrix or a "closer" matrix has to be obtained at a relatively higher expense in the inversion or decomposition of the approximate matrix. In addition, the subroutines in the NSPCG do the preconditioning every time when they are called, which may result in unnecessary overhead. In our nonlinear wave calculations, matrix **A** is function of time and (6.1) must be solved each time step. For large time simulations, a large number of time steps are necessary. If (6.1) was solved using some subroutine in the NSPCG for each time step, the overhead would be quite large.

However, we can easily find a very close approximation $\hat{\mathbf{A}}$ in our problem. We choose $\hat{\mathbf{A}}$ as **A** at $t = 0$, $\mathbf{A}_o$. Although the free surface and the auxiliary surface change with time, $\mathbf{A}_o$ is still a very good approximation to **A**. Therefore, we can invert $\mathbf{A}_o$ once and $\mathbf{A}_o^{-1}$ can be used to precondition (6.1) for every time step. $\mathbf{A}_o$ can be inverted by a direct method. Although the inversion of $\mathbf{A}_o$ is expensive, this is done only once for the whole computation and the computation time for inverting $\mathbf{A}_o$ is very small compared to the computation time saved in solving the preconditioned systems. In GMRES, most of the computation time is used to calculate the multiplication of the matrix **A** and the vector **x** on the left hand side of (6.1) in each iteration. If preconditioning is employed, it needs an additional multiplication of the matrix and the vector for the GMRES to calculate the left hand side of (B.1). This overhead is also small if the total number of iterations can be largely reduced. The preconditioning matrix can also be upgraded after a certain period of time.

The following example shows how effective the preconditioning technique with the

GMRES is in the nonlinear wave computations. We compute the nonlinear waves generated by a submerged source-sink pair (used to model the Coast Guard cutter) starting to move horizontally from the rest. 3367 node points on the free surface and 3367 isolated sources above the free surface are used resulting a 3367×3367 matrix $\mathbf{A}$. The computation is conducted on a Cray Y-MP. The computed wave is shown in Fig. 6.1. In this computation, 1000 time steps are used, that is, we need to solve (6.1) or (B.1) for 1000 times. If no preconditioning is applied, for each time step, GMRES takes an average of 120 iterations (about 18.5 CPU seconds) to converge in solving (6.1). So, the total CPU spent on solving (6.1) is about 18500 seconds. When the preconditioning is applied, GMRES takes only about 5 to 6 iterations (about 1.75 seconds) to converge in solving (B.1). The total CPU for solving the linear system adds up to 1900 seconds including the time for the one-time inversion of $\mathbf{A}_o$ which is about 150 CPU seconds. So, the preconditioning saves CPU time for the solution of the linear system by more than 80 %.

Preconditioning of the matrix also delays the convergence difficulty due to large desingularization distances because the larger the distance, the closer the matrix $\mathbf{A}_o$ is to $\mathbf{A}$. This allows the use of a relatively large desingularization at the same time improving the accuracy of the numerical integrations. The preconditioning technique can also be used in the iterative procedure for steady nonlinear wave computations by the method of Jensen, Mi & Söding (1986).

BIBLIOGRAPHY

BIBLIOGRAPHY

[1] Akylas, T.R. 1984 On the excitation of long nonlinear water waves by a moving pressure disturbance. *J. Fluid Mech.* **141**, 455-466.

[2] Akylas, T.R., Kung, T.J. & Hall, R.E. 1988 Nonlinear groups in ship wakes. *proc. 17th Symp. on Naval Hydrodynamics*, The Hague.

[3] Baker, G.R., Meiron, D.I. and Orszag, S.A. 1982 Generalized vortex methods for free surface flow problems. *J. Fluid Mech.* **123**, 477-501.

[4] Beck, R.F. and Magee, A.R. 1990 Time-domain analysis for predicting ship motions. *Proc. of the IUTAM symp. on Dynamics of Marine Vehicles and Structures in Waves*, Uxbridge, U.K.: Brunel University.

[5] Benjamin, T.B., Bona, J.L. and Mahony, J.J. 1972 Model equations for long waves in nonlinear dispersive systems. *Phil. Trans. R. Soc. Lond.* **A 272**, 47-78.

[6] Bertram, V., Schultz, W.W., Cao, Y. and Beck, R.F. 1991 Nonlinear computations for wave drag, lift and moment of a submerged spheroid. *Ship Technology Research* **38**, 3-5.

[7] Bertram, V. 1990 A Rankine source method for forward-speed diffraction problem. Report No. 508, Institut Für Schiffbau, Der Universit ät Hamburg, Juli.

[8] Boppe, C. 1990 personal communication.

[9] Briggs, W.L. 1987 *A Multigrid Tutorial*, Society for Industrial and Applied Mathematics, Philadelphia.

[10] Brown, E.D., Buchsbaum, S.B., Hall, R.E., Penhune, J.P., Schmitt, K.F., Watson, K.M. and Wyatt, D.C. 1989 Observations of a nonlinear solitary wave packet in the Kelvin wake of a ship. *J. Fluid Mech.* **204**, 263-293.

[11] Cao, Y., Schultz, W.W. and Beck, R.F. 1990 Three-dimensional, unsteady computations of nonlinear waves caused by underwater disturbance. *Proc. 18th Symp. on Naval Hydrodynamics*, Ann Arbor, Michigan, USA.

[12] Cao, Y., Schultz, W.W., and Beck, R. F. 1991a Three-dimensional desingularized boundary integral methods for potential problems. *Int. J. Num. Meth. Fluids* **12**, 785-803.

[13] Cao, Y., Schultz, W.W., and Beck, R. F. 1991b Two-dimensional solitary waves generated by a moving disturbance. *6th International Workshop on Water Waves and Floating Bodies*, Woods hole, Massachusetts, USA.

[14] Carriero, N. and Gelernter, D. 1989 How to write parallel programs: A Guide to the perplexed. *ACM Computing Surveys* **21**, 323-357

[15] Choi, H.S., Bai, K.J., Kim, J.W. and Cho, H. 1990 Nonlinear free surface waves due to a ship moving near the critical speed in a shallow water. *Proc. 18th Symp. on Naval Hydrodynamics*, Ann Arbor, Michigan, USA

[16] Cole, S.L. 1985 Transient waves produced by flow past a bump. *Wave Motion* **7**, 579-587, North-Holland.

[17] Copson, E.T. 1965 *Asymptotic Expansions.* Cambridge University Press.

[18] Doctors, L.J. and Beck, R.F. 1987 Convergence properties of the Neumann-Kelvin problem for a submerged body. *J. Ship Research* **31** 227-234.

[19] Dommermuth, D.G. and Yue, D.K.P. 1987 A High-Order equation for shallow-water waves. *3rd Int. Workshop on Water waves and floating bodies*, Woods hole, Massachusetts, USA.

[20] Dommermuth, D.G., and Yue, D.K.P. 1987 Numerical simulations of nonlinear axisymmetric flows with a free surface. *J. Fluid Mech.* **178**, 195-219.

[21] Dommermuth, D.G., and Yue, D.K.P. 1988 The Nonlinear three-dimensional waves generated by a moving surface disturbance. *Proc. 17th Symp. on Naval Hydrodynamics*, The Hague.

[22] Duncan, R. 1990 A survey of parallel computer architectures. *Computer* **23**, 5-16

[23] Eggers, K. 1957 Uber das wellenbild einer pulsierenden strorung in translatioL. *Schiff and Hafen* **11**, Hamberg.

[24] Ertekin, R.C., Webster, W.C. and Wehausen, J.V. 1986 Waves caused by a moving disturbance in a shallow channel of finite depth. *J. Fluid Mech.* **169**, 275-292.

[25] Farell, C. 1973a On the wave resistance of a submerged spheroid. *J. Ship Research* **17**, 1-11.

[26] Farell, C. 1973b On the experimental determination of the resistance components of a submerged spheroid. *J. Ship Research* **17**, 72-79.

[27] Fu, L. and Holt, B. 1982 SEASAT views oceans and sea ice with synthetic aperture radar. *JPL Publication*, 81-120, Pasadena, California.

[28] Greengard, L. and Rokhlin, V. 1988 On the efficient implementation of the fast multipole algorithm. *Research Report* YALEU/DCS/RR-602, February.

[29] Greengard, L. 1990 The numerical solution of the N-body problem. *Computers in Physics*, Mar/Apr.

[30] Grilli, S. and Svendsen, I.A. 1989 Runup and reflection of a solitary wave on steep slopes in a numerical tank. *4th Int. Workshop on Water Waves and Floating Bodies*, Vystese, Norway.

[31] Hall, R. and Buchsbaum, S. 1990 A model for the generation and evolution of an inner-angle soliton in a Kelvin wake. *Proc. 18th Symp. on Naval Hydrodynamics*, Ann Arbor, Michigan, USA.

[32] Han, P.S., and Olson, M.D. 1987 An adaptive boundary element method. *Inter. J. Num. Meth. in Engin.* **24**, 1187-1202.

[33] Havelock, T.H. 1931 The Wave Resistance of a Spheroid. *Proc. Royal Soc.* Series **A**, **131**, 275-285.

[34] Heise, U. 1978 Numerical properties of integral equations in which the given boundary values and the solutions are defined on different curves. *Comput. Struct.* **8**, 199-205.

[35] Jankowski, J. 1990 Fundamental solutions of linear hydrodynamic boundary-value problems. *Classification*, Polski Rejestr Statków Publicaion 1, GDAŃSK, May.

[36] Jensen, G., Mi, Z.X., and Söding, H. 1986 Rankine source methods for numerical solutions of the steady wave resistance problem. *Proc. 16th Symp. on Naval Hydrodynamics*, Berkeley, California, USA.

[37] Johnston, R.L., and Fairweather, G. 1984 The method of fundamental solutions for problems in potential flow. *Appl. Math. Modeling* **8**, 265-270.

[38] Joo, S.W., Schultz, W.W. and Messiter, A. 1990 An analysis of the initial-value wavemaker problem. *J. Fluid Mech.* **214**, 161-183.

[39] JOWIP and SARSEX Special Issure. *J. Geophysical Research*, 1988.

[40] Kang, C.G. 1988 Bow flare slamming and nonlinear free surface body interaction in the time domain. PhD thesis, Dept. of Naval Architecture and Marine Engineering, The University of Michigan, USA.

[41] Katsis, C. and Akylas, T.R. 1987 On the excitation of long nonlinear water waves by a pressure distribution. Part 2. Three-dimensional effects. *J. Fluid Mech.* **177**, 49-65.

[42] King, B.K. 1987 Time-domain analysis of wave exciting forces on ships and bodies. Ph.D. Diss., Dept. of Naval Architecture and Marine Engineering, The University of Michigan, USA.

[43] King, B., Beck, R.F., and Magee, A. 1988 Seakeeping calculations with forward speed using time-domain analysis. *Proc. 17th Symp. on Naval Hydrodynamics*, The Hague.

[44] Korsmeyer, T. 1990 An order N algorithm for the solution of the boundary integral equations of potential flow. *5th International Workshop on Water Waves and Floating Bodies*, Manchester, England.

[45] Kupradze, V. 1967 On the approximate solution of problems in mathematical physics. *Russ. Math. Surveys* **22**, 59-107.

[46] Lamb, H. 1929 *Hydrodynamics*, U.K., Cambridge University Press.

[47] Lee, S.J., Yates, G.T. and Wu, T.Y. 1989 Experiments and analyses of upstream-advancing solitary waves generated by moving disturbances. *J. Fluid Mech.* **199**, 569-593.

[48] Liapis, S.J. and Beck, R.F. 1985 Seakeeping computations using time domain analysis. *Proc. of 4th International Conference on Numerical Hydrodynamics*, Washington, D.C.,: National Academy of Sciences.

[49] Lin, W.M. 1984 Nonlinear motion of the free surface near a moving body. Ph.D. Diss., Dept. of Ocean Engineering, MIT, USA.

[50] Longuet-Higgins M.S., and Cokelet,C.D. 1976 The deformation of steep surface waves on water: I. A numerical method of computation. *Proc. R. Soc. London* **A350**, 1-26.

[51] Magee, A. 1991 Large-amplitude Ship Motions in the Time Domain . Ph.D. Diss., Dept. of Naval Architecture and Marine Engineering, The University of Michigan, USA.

[52] Martin, P.A. 1981 On the Null-Field Equations for water-wave radiation problems. *J. Fluid Mech.* **113**, 315-332.

[53] Mei, C.C. 1986 Radiation of solitons by slender bodies advancing in a shallow channel. *J. Fluid Mech.* **162**, 53-67.

[54] Mei, C.C. 1991 Ship oscillations and wake solitons. *6th International Workshop on Water Waves and Floating Bodies*, Woods hole, Massachusetts, USA.

[55] Munk, W.H., Scully-Power, P. and Zacharisen, F. 1987 Ships from space. *Proc. R. Soc. Lond.* **A 412**, 231-254.

[56] Nakos, D.E. and Sclavounos, P.D. 1990 Ship motions by a three-dimensional Rankine panel method. *Proc. 18th symp. on Naval Hydrodynamics*, Ann Arbor, Michigan, USA.

[57] Newman, J.N. 1961 A linearized theory for the motion of a thin ship in regular waves. *J. Ship Research*, **5**, 34-55.

[58] Newman, J.N. 1986 Distributions of sources and normal dipoles over a quadrilateral panel. *J. Eng. Math.* **20**, 113-126.

[59] Newman, J.N. 1977 *Marine Hydrodynamics.* The MIT Press.

[60] Noblesse, F. and Hendrix, D. 1990 Fourier-Kochin representation of the flow due to a ship advancing in regular waves. *Proc. of the IUTAM symp. on Dynamics of Marine Vehicles and Structures in Waves*, Uxbridge, U.K., Brunel University.

[61] Olson, L.G. 1989 GMRES iterative solution of matrix systems derived from boundary element techniques. PSH Report, Dept. of Mechanical Engineering and Applied Mechanics, The University of Michigan, Ann Arbor, Michigan, USA.

[62] Oppe, T.C., Joubert, W.D. and Kincaid, D.R. 1988 NSPCG User's Guide version 1.0: A packege for solving large sparse linear systems by various iterative methods. *Center for Numerical Analysis*, The University of Texas at Austin, Austin, Texas, USA.

[63] Pedersen, G. 1988 Three-dimensional wave patterns generated by moving disturbances at transcritical speeds. *J. Fluid Mech.* **196**, 39-63.

[64] Reed, M.D., Beck, R.F., Griffin, O.M. and Peltzer, R.D. 1990 Hydrodynamics of remotely sensed surface ship wakes. *Trans. SNAME* **98**.

[65] Rokhlin, V. 1985 Rapid solution of integral equations of classical potential theory. *J. Computational Physics* **60**, 187-207.

[66] Saad, Y. and Schultz, M.H. 1986 GMRES: A generalized minimal residual algorithm for solving nonsymmetric linear systems. *SIAM J. Sci. Stat. Comp.* **7**, 856-869.

[67] Schultz, W.W., Cao, Y., and Beck, R.F. 1990 Three-dimensional nonlinear wave computation by desingularized boundary integral method. *5th International Workshop on Water Waves and Floating Bodies*, Manchester, England.

[68] Schultz, W.W., and Hong, S.W. 1989 Solution of potential problems using an overdetermined complex boundary integral method. *J. Comp. Phys.* **84**, 414-440.

[69] Scragg, C.A. and Talcott, J.C. 1990 Numerical solution of the "Dawson" free-surface problem using Havelock singularities. *Proc. 18th Symp. on Naval Hydrodynamics*, Ann Arbor, Michigan, USA.

[70] Stoker, J.J. 1957 *Water Waves.* Interscience Publishers.

[71] Ursell, F. 1960 On Kelvin's ship wave pattern. *J Fluid Mech.* **8** 418-431.

[72] Vinje, T., and Brevig, P. 1981 Nonlinear ship motions. *Proc. of 3rd Int. Conf. on Numerical Ship Hydrodynamics*, Paris.

[73] von Kármám, T. 1930 Calculation of pressure distribution on airship hulls. NACA Technical Memorandum **574**.

[74] Webster, W.C. 1975 The flow about arbitrary, three-dimensional smooth bodies. *J. Ship Research* **19**, 206-218.

[75] Wehausen, J.V. and Laitone, E.V. 1960 Surface waves. *Encyclopedia of Physics*, **9** 446-778, Springer-Verlag.

[76] Wehausen, J. V. 1964 Effect of the initial acceleration upon the wave resistance of ship models. *J. Ship Research* **7**, 38-50.

[77] Whitham, G.B. 1974. *Linear and Nonlinear Waves.* Wiley.

[78] Wu, D.M. and Wu, T.Y. 1982 Three-dimensional nonlinear long waves due to surface pressure. *Proc. 14th Symp. on Naval Hydrodynamics*, National Academy Press.

[79] Wu, T.Y. 1987 Generation of upstream-advancing solitons by moving disturbances. *J. Fluid Mech.* **184**, 75-99.

[80] Yeung, R.W. 1982 Numerical methods in free-surface flows. *Ann. Rev. Fluid Mech.* **14** 395-442.

[81] Yih, C.S. and Zhu, S. 1989a Patterns of ship waves. *Q. Appl. Math.* **47**, 17-33.

[82] Yih, C.S. and Zhu, S. 1989b Patterns of Ship waves II: Gravity-capillary waves. *Q. Appl. Math.* **47**, 35-44.